(12) INTERNATIONAL APPLICATION PUBLISHED UNDER THE PATENT COOPERATION TREATY (PCT)

(19) World Intellectual Property Organization
International Bureau

(43) International Publication Date
30 January 2003 (30.01.2003)

PCT

(10) International Publication Number
WO 03/007809 A2

(71) Applicant (for all designated States except US): ART, ADVANCED RESEARCH TECHNOLOGIES INC. [CA/CA]; 2300 Alfred-Nobel Blvd., Saint-Laurent, Québec H4S 2A4 (CA).
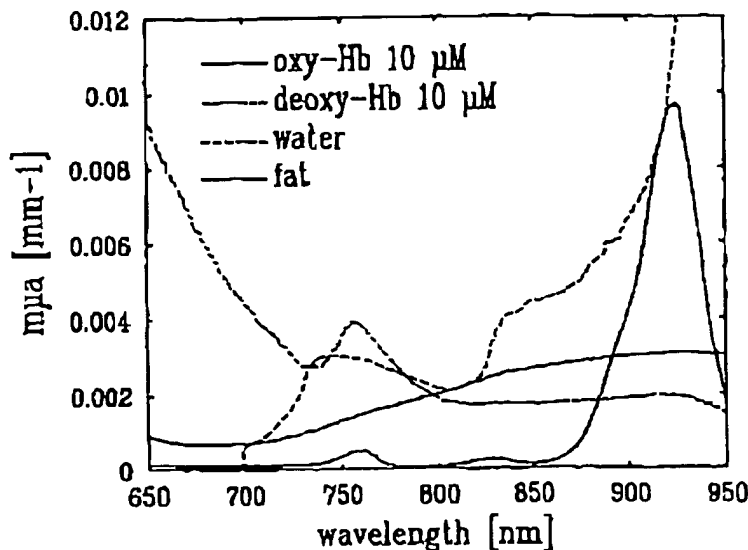
(72) Inventors; and
(75) Inventors/Applicants (for US only): HALL, David, Jonathan [GB/CA]; 3445 rue Drummond, app. 1005, Montreal, Québec H3G 1X9 (CA). KHOL-BAREIS, Mathias [DE/DE]; Drosselveg 21, 53489 Sinzig (DE).

(74) Agents: OGILVY Renault et al.; 1981 McGill College Avenue, Suite 1600, Montreal, Quebec H3A 2Y3 (CA).

(54) Title: CHOICE OF WAVELENGTHS FOR MULTIWAVELENGTH OPTICAL IMAGING

(57) Abstract: The present invention relates to a method for wavelength selection in a multi-wavelength TPSF-based optical imaging system. This consists of identifying several chromophores in a highly turbid medium and selecting optimized wavelengths whereby using these wavelengths optimizes the deduction of the chromophore concentrations. Such chromophore concentrations may be combined to deduce other properties of the turbid medium.

- 1 -

CHOICE OF WAVELENGTHS FOR MULTIWAVELENGTH OPTICAL IMAGING

Field of the Invention

5   The present invention relates to the field of optical imaging in which objects which diffuse light, such as some human body tissues, are imaged using signals resulting from the injection of light into the object and detection of the diffusion of the light in the object at a number of positions. More particularly, the present invention relates to the choice of wavelengths for multiwavelength optical imaging in order to provide enhanced information.

10   Background of the Invention

Time-domain optical medical images show great promise as a technique for imaging breast tissue, as well as the brain and other body parts. The objective is to analyze the temporal point spread function (TPSF) of an injected pulse as it is diffused in the tissue, and the information extracted from the TPSF is used in
15   constructing a medically useful image.

For example, one can extract time-gated attenuation information from the TPSF which improves the image spatial resolution over previous continuous wave methods. However, it is unclear whether such improvements in image spatial resolution are adequate for diagnosing breast cancer based on morphology.

20   An alternative approach is to use the TPSF to decouple the light attenuation into absorption and scattering components. This extra information, which cannot be obtained from continuous wave methods, may be clinically useful. Moreover, one can obtain the tissue absorption spectrum by performing time-domain measurements at multiple wavelengths. In tissue there are several molecules
25   which absorb the light and are known as chromophores. Spectroscopic analysis of the tissue absorption spectrum permits chromophore concentrations to be measured. Furthermore, combination of the chromophore concentrations can yield physiological information, as opposed to morphologic information, which could provide a more medically useful image.

30   The problem is one of knowing which are the dominant chromophores to include in a tissue model and then choosing the "best" wavelengths to deduce their concentrations most accurately.

- 2 -

Summary of the invention

It is an object of the invention to improve image quality in TPSF-based optical images by choosing an efficient combination of wavelengths and combining information from the combination of wavelengths.

5   It is an object of the present invention to provide an objective method for choosing the wavelengths for a multiwavelength TPSF-based optical imaging approach. For a given set of chromophores, the best selection of the wavelengths is performed for the set as a whole as opposed to choosing the best wavelength for each chromophore individually. Furthermore, hardware
10   constraints can be taken into consideration in order to optimize the selection of wavelengths for a given device.

Brief description of the drawings

Fig. 1 illustrates the absorption spectra used of oxy-Hb, deoxy-Hb, pure water and lipid;

15   Fig. 2 illustrates the inverse of the condition number of the hemoglobin specific absorption matrix as a function of wavelength $\lambda 1$ being plotted for a system of a) two wavelengths where the other wavelength is fixed at $\lambda 2 = 850$ nm, b) three wavelengths where the other wavelengths are fixed $\lambda 2 = 850$ nm and $\lambda 3 = 758$ nm and c) four wavelengths where the other wavelengths are fixed $\lambda 2 = 850$ nm,
20   $\lambda 3 = 758$ nm and $\lambda 4 = 800$ nm;

Fig. 3 illustrates the inverse of condition number C for the specific absorption spectra of oxy-Hb and deoxy-Hb as a function of $\lambda 1$ and $\lambda 2$. The plot is symmetric with respect to the diagonal. Regions of high values indicate combinations of wavelengths advantageous for spectroscopy;

25   Fig. 4 illustrates the deviation of calculated saturation and true saturation (S(calc)-S(true)) for a model tissue containing 15 μM [HbT], S(true) = 25%, 50% and 75% and a lipid concentration of 40%. Two wavelengths at 760 and 850 nm were used to fit [oxy-Hb] and [deoxy-Hb]. The sensitivity with respect to wrong assumptions of lipid and water concentrations are shown;

30   Fig. 5A illustrates the inverse of condition number C for the specific absorption spectra of oxy-Hb and deoxy-Hb and lipid for a fixed wavelength $\lambda = 830$ nm as a function of $\lambda 1$ and $\lambda 2$. The islands of high values indicate advantageous wavelengths (scaling 0-0.01);

- 3 -

Fig. 5B illustrates the inverse of condition number C for the specific absorption spectra of oxy-Hb and deoxy-Hb and lipid for a fixed wavelength $\lambda 3 = 830$ nm as a function of $\lambda 1$ and $\lambda 2$ (same as Fig. 5A but scaling 0-0.0005);

Fig. 6A illustrates the inverse of condition number C for the specific absorption
5   spectra of oxy-Hb and deoxy-Hb, lipid and water for two fixed wavelength at $\lambda 3 = 760$ nm and $\lambda 4 = 830$ nm as function of $\lambda 1$ and $\lambda 2$ (scaling 0-0.0015). Regions of high values are advantageous for spectroscopy;

Fig. 6B illustrates the inverse of condition number C for the specific absorption spectra of oxy-Hb and deoxy-Hb, lipid and water for two fixed wavelength at $\lambda 3 =$
10   760 nm and $\lambda 4 = 830$ nm as function of $\lambda 1$ and $\lambda 2$. (same as Fig. 6A but scaling 0-0.0005);

Fig. 7 illustrates the estimation of deviations from true saturation values for a model tissue of [HbT] = 20 µM, S= 75%, a lipid concentration of 40% and true water concentration corresponding to 0-100% water. Three wavelengths at 760,
15   780 and 850 nm were used for back calculation of S, shown here as a function of assumed water concentration;

Fig. 8 illustrates the estimation of the influence of errors (noise) in μ_a on the calculated Hb concentrations and saturation values. A model μ_a-spectrum based on 20 µM [HbT], S=50%, and a lipid and water concentration of 30% and 40%
20   was assumed. Matrix inversion was performed for wavelengths 760, 790, 830 and 850 nm. plotted is the change in calculated [oxy-Hb], [deoxy-Hb] and saturation value when the μ_a value at a single wavelength was changed by +0.0001mm^{-1}. This plot suggests that noise at 830 nm translates in the highest noise in saturation values;

25   Fig. 9 illustrates the estimation of the recovery of saturation values based on different wavelength combinations. A model tissue of 20 µM [HbT], a true saturation of S=75%, lipid and water concentration of 40% were used. in the lower plot an offset of 0.0005 mm^{-1} independent of wavelength was added to the model tissue µa-spectrum (no offset in the upper plot). Plotted are deviations of
30   the saturation values due to matrix inversion and the true 75% value. The following wavelength combinations were used: 1) 760 nm and 850 nm, 2) 760, 830 and 850 nm, 3) 760, 780, 830 and 850 nm, 4) 750-850nm, 5) 720-850 nm, 6) 720-900nm;

Fig. 10 illustrates the estimation of the recovery of saturation values based on
35   different wavelength combinations. A model tissue of 20 µM [HbT], a true

- 4 -

saturation of S=50%, lipid and water concentration of 40% were used. In the lower plot an offset of 0.0005 mm^{-1} independent of wavelength was added to the model tissue μa-spectrum (no offset in the upper plot). Plotted are deviations of the saturation values due to matrix inversion and the true 75% value. The

5   following wavelength combinations were used: 1) 760 nm and 850 nm, 2) 760, 830 and 850 nm, 3) 760, 780, 830 and 850 nm, 4) 750-850nm, 5) 720-850 nm, 6) 720-900nm;

Detailed Description of the invention

In accordance with the present invention, there is provided a method for
10 selecting wavelengths for multiwavelength optical imaging.

Tissue Chromophores

The dominant near infrared chromophores contained in breast tissue are considered to be hemoglobin (Hb) in its oxygenated (oxy-Hb) and deoxygenated (deoxy-Hb) forms, water and lipids. Fig. 1 shows the absorption spectra of oxy-
15 Hb (at 10μM concentration), deoxy-Hb (at 10μM concentration), pure water (100% concentration), lipid (absorption spectrum of olive oil has been used to estimate the absorption spectrum of fat). There are other interesting near infrared chromophores, such as glucose and cytochrome c oxidase, but their absorption contribution in the breast is considered negligible compared to the
20 aforementioned chromophores.

Physiological information

Potentially useful physiological information about the breast tissue can be obtained from concentrations,[], of the chromophores. The total hemoglobin concentration, [HbT], defined as [HbT] = [oxy-Hb] + [deoxy-Hb], is related to the
25 local vascular density. Since cancer is commonly associated with an increase in vascularisation (angiogenesis), a measurement of [HbT] could be medically useful. The fraction of hemoglobin that binds to oxygen is known as the oxygen saturation, S, and defined as. S=[oxy-Hb]/[HbT]. Increased metabolic activity increases oxygen demands which decreases the oxygen saturation. Since
30 cancer is commonly associated with increased metabolic activity, a measurement of S could also be medically useful.

Wavelength Choice

Historically as the biomedical optics field evolved the wavelengths were chosen for each chromophore individually by observing strong near infrared spectral

- 5 -

features for the given chromophore and using the closest hardware-available wavelength. Many researchers also used the isobestic wavelength of oxy-Hb and deoxy-Hb, the wavelength where their absorption per concentration are equal, since this wavelength is insensitive to the oxygenation state of the

5   hemoglobin and can be related to the [HbT].

However, the question both posed and addressed here is that for a given set of chromophores what are the optimal wavelengths to use in order to deduce the concentration of each chromophore? It is interesting to note that the isobestic wavelength used by many researchers turns out not to ·be one of the

10   wavelengths of choice.

It is an object of the present invention to provide an objective method for choosing the wavelengths for a multiwavelength TPSF-based optical imaging approach. For a given set of chromophores, the best selection of the wavelengths is performed for the set as a whole as opposed to choosing the

15   best wavelength for each chromophore individually. Moreover, it is also possible to investigate scenarios such as the influence on determining chromophore concentrations under certain assumptions about the concentration(s) of other chromophore(s) in the set. Furthermore, hardware constraints can also be taken into consideration in order to optimize the selection of wavelengths for a given

20   device. Fortunately, the recent advent of turn-key, pulsed, tunable near infrared wavelength lasers has permitted more viable availability of near infrared wavelengths.

Experimental brute force approach

One possible approach to optimize the choice of wavelengths for a given set of

25   chromophores is to conduct a brute force experimental study. This would consist of performing numerous experiments where different combinations of wavelengths are evaluated for the given set of chromophores at known concentrations until the optimum combination for deducing their concentrations . is found. Obviously, this approach is likely to be highly time-consuming and it is

30   not always trivial to provide a set of chromophores at known concentrations, particularly in the case of in vivo breast tissue.

Matrix Inversi n sensitivity approach

An alternative approach which avoids the numerous experiments of the experimental brute force approach is a matrix inversion sensitivity approach.

- 6 -

The equation which needs to be solved can be written for each wavelength as:

$$\mu_a(\lambda_1) = \sum_i m_{a,i}(\lambda_1) \cdot c_i$$

$$\mu_a(\lambda_2) = \sum_i m_{a,i}(\lambda_2) \cdot c_i$$

$$\cdots\cdots$$

5

$$\mu_a(\lambda_3) = \sum_i m_{a,i}(\lambda_3) \cdot c_i$$

where μ_a is the measured absorption coefficient, m_a is the specific absorption coefficient of the different chromophores and c_i is the corresponding concentration.

10   This is written is matrix form as:

$$\mu_a = M \cdot c$$

where printing in bold indicates a matrix or vector. μ_a is a vector with a number of rows corresponding to the number of wavelengths (n_λ). c is a vector with the number of rows corresponding to the number of chromophores (n_c). M is a

15   rectangular matrix of size $n_\lambda \times n_c$.

If $n_\lambda = n_c$ the system can be solved by matrix inversion $c = M^{-1}\mu_a$ and if $n_\lambda > n_c$ the system is overdetermined and can be solved by the pseudo-inverse $M^+ = (M^T M)^{-1} M^T$ where M^T is the transposed matrix of M.

$$c = (M^+)\mu_a$$

20   The pseudoinverse M^+ is an $n_\lambda \times n_c$ array which is unique. If M is square (i.e. not overdetermined) the $M^+ = M^{-1}$. For given (i.e. chosen) wavelengths the pseudoinverse M^+ can be precalculated once and the matrix inversion corresponds to a simple matrix multiplication. This is the basis for the calculation of chromophore concentration.

25   One means to quantify the expected sensitivity of a matrix inversion of a matrix M with respect to small errors in the data is the condition number C which is defined as:

$$C = norm (M) \cdot norm (M^{-1})$$

C gives an indication of the accuracy of the r sults and is an estimate of the
30   cross-talk between the different channels (i.e. chromophores concentrations).

-7-

Values of C near 1 indicate a well-conditioned matrix, large values indicate an ill-conditioned matrix. The condition number is closely related to singular value decomposition (SVD) as it is the ratio of the largest and the smallest singular value of a matrix.

5   The matrix M for oxy-Hb and deoxy-HB at λ = 760 and 770 nm is

$$M = \begin{matrix} 0.3871 & 0.1465 \lambda = 760nm \\ 0.3280 & 0.1625 \lambda = 770nm \end{matrix}$$

A matrix inversion is possible as the rank (M) = 2, however the absorption at the two wavelengths is 'similar'. The condition number is C = 20.49. Choosing the wavelengths to be λ = 760 and 850 nm gives the matrix

10

$$M = \begin{matrix} 0.3871 & 0.1465 \\ 0.1729 & 0.2645 \end{matrix}$$

Inspection by eye already shows that the absorption is very 'different'. This is confirmed by the condition number: C=3.206. In what follows below the inverse of the condition number is plotted and analyzed. It has value between 0 and 1. 1/C close to 1 means 'orthogonal' spectra and low sensitivity to cross-talk. Small
15   values of 1/C mean an ill-conditioned matrix. To find the best wavelengths, 1/C is calculated as a function of a wavelength. The wavelengths that give the highest values of 1/C are the best for a calculation of chromophore concentrations and the subsequent physiological information such as oxygen saturation, S.

20   Model absorption spectra were generated with the absorption spectra of Fig. 1 based on estimations of [HbT], S, lipid and water concentration. Matrix inversion based on different sets of wavelengths were performed to recover these parameters. These parameters were compared with the true ones for the different wavelengths and the sensitivity to noise or measurement offsets
25   considered.

Assuming that we fit for the hemoglobin concentrations only and assuming certain values for water and lipid concentration, for a x-wavelengths matrix inversion, the best combination of wavelengths to give a well-conditioned matrix, the sensitivity of calculated values of oxy-Hb and deoxy-Hb concentration and
30   oxygen saturation for variations of lipid or water concentration and sensitivity of S to measurement noise have been determined.

-8-

In Fig. 2 the inverse of the condition number is shown for matrices of oxy-Hb and deoxy-Hb specific absorption coefficients for 2, 3 and 4 wavelengths. In each case one wavelength (λ_1) was varied between 650 and 950 nm while the remaining wavelengths were fixed λ_2 = 850 nm (2-wavelength system), λ_2 = 850

5   nm and λ_3 = 758 nm (3-wavelength system), and λ_2 = 850 nm, λ_3 = 758 nm and λ_4 = 800 nm (4-wavelength system). Fig. 2 indicates that the selection of two wavelength at λ_1 = 850 nm and λ_2 = 700 nm gives the highest values of 1/C and when the wavelength range is restricted via hardware constraints to > 750 nm, a system that includes the peak wavelength of deoxy-Hb close to 760 nm is

10   advantageous. It does not matter whether two or more wavelengths are used. This somewhat counterintuitive result is valid only. without measurement noise and noise in the background absorption.

Fig. 3 further highlights this finding for a two-wavelength matrix inversion. In this figure 1/C is plotted as a function of both at λ_1 and λ_2 in the range 650-950 nm.

15   The plot is symmetric with respect to the diagonal. Regions of high 1/C-values can be chosen and the corresponding 'good' wavelengths can be read off the axis. It is apparent that (with the restriction to > 750 nm) the one wavelength should be close to 760 nm while the other one can be within the range 830-900 nm without substantially affecting the condition number.

20   Using the spectra shown in Fig.1, model tissue absorption spectra were generated. Based on matrix inversion values of [oxy-Hb], [deoxy-Hb] and S were backcalculated and the sensitivity to incorrect assumptions about the [water] and [lipid] tested. One approach is to take the measured μ_a spectra and subtract water and lipid absorption corresponding to certain assumed concentrations. For

25   the data shown in Fig. 4, a model tissue containing 15 µM [HbT], (true) saturation values of S = 25%, 50% and 75% was used. Lipid concentration was 40%. It was tested how a misjudgement of water concentration affects the recalculated S value. To test the error in a simple two-wavelengths-fit (760 and 850 nm), the assumed lipid concentration was varied between 0 and 100%.

30   When the assumed water concentration is right (lower three lines in Fig. 4), the deviation in saturation between true and calculated values is < ±2% (obviously with zero error for the right lipid concentration of 40%). A misjudgement about the water concentration by 20% (upper lines in Fig. 5) results in additional errors in S(calc)-S(true) of up to 2% for S=75%, 4% for S=50% and 8% for S=25%.

35   These errors in S are a function of the underlying tissue absorption coefficients. The values here giv an indication about the order of magnitude.

Having a system with more than two fit-parameters, best wavelength combinations, for a three-components system of oxy-Hb, deoxy-Hb and lipid system, for a four-components system of oxy-Hb, deoxy-Hb, lipid and water, and the sensitivity of calculation of S to noise at the different wavelengths have been

5   determined.

In Figs. 5A and 5B the inverse of the condition number is plotted for a three wavelengths system based on the oxy-Hb, deoxy-Hb and lipid specific absorption spectra as a function of λ_1 and λ_2. The third wavelength was fixed at $\lambda_3 = 830$ nm. Again, the plot is symmetric with respect to the diagonal. From Fig.

10   5A it is apparent, that there are three "islands" of high 1/C values. Unfortunately, all of these island would include wavelengths outside an imposed hardware constrained wavelength range of 750 to 850 nm. Plotting the same data in a different scale (Fig. 5B) shows that there is just a single preferential combination within this hardware constrained wavelength range: 760 and 780 nm.

15   Equivalent to Figs. 5A and 5B, the inverse of C for a 4-wavelengths system is plotted in Fig. 6A and 6B. Again, the difference between them is the scaling. Two wavelengths were fixed at $\lambda_3 = 760$ nm and $\lambda_4 = 830$ nm. Including the wavelengths outside the 750-850 nm range there appear four preferential combinations. Restricting the wavelength range to 750-850 nm there are just two

20   advantageous region (marked by the white rectangle in Fig. 6B): 780 nm and 850 nm, and 780 nm and 815 nm.

From the analysis based on matrix condition numbers, the best wavelength combinations for 2, 3 and 4 wavelengths measurements are the following:

- 10 -

Table 1

Wavelength combinations for 2, 3 and 4 wavelengths measurements

	Wavelength Range	Best wavelengths (nm)				fit for	see Fig.
		$\lambda 1$	$\lambda 2$	$\lambda 3$	$\lambda 4$		
2-λ	650-950 nm	700	>860			Oxy-Hb, deoxy-Hb	2,3
	750-850 nm	760	850				
3-λ	650-950 nm	700-760	830	925		+ lipid	5 A,B
		830	860-870	925			
	750-850 nm	760	780	830			
4-λ	650-950 nm	760	830	860	925	+ lipid, + water	6A,B
		700	760	830	925		
	750-850 nm	760	780	830	850	Best combination	
		760	780	815	830		

5   Furthermore, it must be pointed out that including more wavelengths does not increase the condition number. E.g. for the four chromophores and all wavelengths in the range 750-850 nm, $1/C = 0.000314$. This is lower than the value ($1/C = 0.00036$, compare with Fig. 6B) when only four wavelengths (760, 780, 830 and 850 nm) are used. In a system without noise and no other
10   chromophores than the four considered here, a 4-wavelengths system is the optimal.

While certainly only a 4-wavelengths measurement allows [oxy-Hb], [deoxy-Hb], [lipid] and [water] to be determined, and a 2-wavelengths system (see Fig. 5) is not sufficient, the question is posed whether a 3-wavelengths measurement
15   might supply S values with a high enough precision. In this case the concentration of one chromophore (water or lipid) must be guessed and the corresponding absorption subtracted from the measured μ_a values. This was tested with a model absorption spectrum and is shown in Fig. 7 for 760, 780 and 850 nm. True water concentration was varied between 10 and 100% (the
20   different lines), and the difference between calculated and true saturation values plotted as a function of assumed water concentration. For instance, for a true

- 11 -

water concentration of 50%, a misjudgment of the water concentration by 10% results in an error in S by about 4%.

Up to now, only "perfect" data sets were considered with no noise. In real situations there are problems due to measurement noise that is random for the
5   different wavelengths; unknown chromophores in the tissue, i.e. there is a background absorption coefficient the spectrum of which we do not know; and possible systematic errors in the primary μ_a recovery.

There are an ample number of parameters which can be considered and as examples the following two questions are considered. First, is the oxygen
10 saturation more susceptible to noise at certain wavelengths? Second, what is the influence of an offset in the μ_a data?

The influence of errors (noise) in μ_a on the calculated Hb concentrations and saturation values was estimated in a model tissue based on 20μM [HbT], S= 50% and a lipid and water concentration of 30% and 40% respectively. Matrix
15 inversion was performed on the μ_a - spectrum of this model tissue for wavelengths 760, 780, 830 and 850 nm. The sensitivity to noise (i.e. variations in μa) at the different wavelengths was estimated by changing the absorption coefficient at a single wavelength by +0.0001 mm^{-1}. In Fig. 8, the change in calculated [oxy-Hb], [deoxy-Hb] and oxygen saturation value due to this "noise"
20 is plotted. This figure shows that the change in oxygen saturation value is about -2% for changes at 760 nm, <0.5% at 780nm, while it translates to a variation of +6% at 830 nm.

There are two conditions that produce an offset in the measured μa-spectra with respect to the true values. First, the algorithm for μ_a-calculation based on TPSF-
25 based optical imaging might lead to a systematic offset e.g. due to residual crosstalk between absorption and scattering parameters. Second, the tissue absorption might have a background of unknown origin (chromophore). Under both conditions the fitting of μ_a-data with the four chromophores is hampered. The effect of such an offset for different wavelength combinations is estimated
30 with a model spectrum of 20 μM [HbT], S=75% and water and lipid concentration of 40%. An offset of 0.0005 mm^{-1} was added to the μ_a-values independent of wavelength. The effect on the calculated oxygen saturation values is known in Fig. 9 for combination of 2, 3 and 4 wavelengths as well as continuous spectra between 750-850, 720-850 and 720-900 nm. It is apparent that the lowest error
35 in S is achieved by the 4-wavelengths combination. Including more wavelengths

- 12 -

increases the error. In Fig. 10 the same calculation was done, however, for a true oxygen saturation value of 50%. Here the lowest error is achieved by the 720-850 nm wavelength range, while using less wavelengths or increasing the fitting range to 900 nm results in larger errors.

5   Based on the assumption that the dominant tissue chromophores are oxy-Hb, deoxy-Hb, water and lipid and analysis of the matrix condition number, measurements at the wavelengths 760, 780, 830 and 850 nm supply an optimal data set when the wavelength range is limited to 750-850 nm under ideal conditions. As shown in Figs. 5 and 6, inclusion of shorter and longer

10 wavelengths promise a better matrix inversion. Under real conditions there is no clear-cut answer about the improvement when more wavelengths are included (see Figs. 9 and 10). It might be advantageous to reduce measurement noise at 4 wavelengths due to longer scan times rather than to include more wavelengths. As demonstrated in Fig. 8, to achieve an optimal accuracy the

15 noise level at different wavelengths has to be adjusted which might require different measurement times at certain wavelengths.

Strictly speaking the work presented here was achieved by optimizing a 2-wavelength system and then optimizing a 4-wavelength system where 2 of the wavelengths were fixed at the optimized 2-wavelength system values. Whilst this

20 is easier to display graphically, preferably all 4 wavelengths would be permitted to vary in a global optimization process. Fortunately, for the specific example presented here when all 4 wavelengths are permitted to vary the same optimal solution is found. However, this may not be true for all situations and a global optimization is preferred.

25 It is also understood that it will be obvious to those skilled in the art that the same approach for choosing optimal wavelengths can be applied to optical absorption spectroscopy in general. For example, in other embodiments of the present invention the method of the present invention is also used for choosing the optimal wavelengths for analyzing the components of paints, pharmaceutical

30 products, food, grain or any other turbid media.

It is also understood that the proposed method applies both to the analysis of absolute chromophore concentrations as to their changes or relative concentrations.

While the invention has been described in connection with specific embodiments

35 thereof, it will be understood that it is capable of further modifications and this

- 13 -

application is intended to cover any variations, uses, or adaptations of the invention following. In general, the principles of the invention and Including such departures from the present disclosures as come within known or customary practice within the art to which the invention pertains and as may be applied to
5   the essential features herein before set forth, and as follows in the scope of the appended claims.

- 14 -

CLAIMS

1.   A method of optical imaging of turbid media using a plurality of discrete wavelengths in an optical imaging system, the method comprising the steps of:

selecting a set of chromophores for characterizing a property of the turbid media;

defining parameters of the system including at least a number of said discrete wavelengths, a value of each of said wavelengths, source power and detector aperture for each of said wavelengths, a choice of image algorithm and source/detector geometries, a choice of source and detector and noise characteristics;

fixing a value of all of said parameters except a plurality of said parameters values to be optimized;

determining an optimal value for each of said parameter values to be optimized as a function of a performance of the system in measuring a concentration of said chromophores in said turbid media for characterizing said property as a whole; and

using said optimal value for each of said parameter values in imaging said turbid media.

2.   The method of claim 1, wherein said imaging is medical imaging, said highly turbid medium being body tissue and said property is physiological.

3.   The method of claim 1 or 2, wherein said parameter values to be optimized comprise a value of each of said wavelengths.

4.   The method of claim 3, wherein said parameter values to be optimized further comprise said number of said discrete wavelengths.

5.   The method of claim 4, wherein said step of determining comprises fixing said number of discrete wavelengths at each of a plurality of numbers, and

- 15 -

determining an optimized performance of the system in measuring a concentration of said chromophores in said turbid media at each of said plurality of wavelengths, and selecting one of said plurality of numbers having a best optimized performance.

6.   The method of claim 3, wherein said step of determining an optimal value for each of said parameters comprising minimizing a condition number of a matrix of specific absorption coefficients of said chromophores as a function of wavelength.

7.   The method of claim 4, wherein said step of determining an optimal value for each of said parameters comprises minimizing a condition number of a matrix of specific absorption coefficients of said chromophores as a function of wavelength.

8.   The method of claim 5, wherein said step of determining an optimal value for each of said parameters comprises minimizing a condition number of a matrix of specific absorption coefficients of said chromophores as a function of wavelength.

9.   The method of claim 1, wherein said step of determining comprises empirically determining said performance of the system for a range of said values for each of said parameter values to be optimized.-

10.   The method of claim 2, wherein said plurality of chromophores comprise at least oxy-hemoglobin and deoxy-hemoglobin.

11.   The method of claim 10, wherein said chromophores are water, lipids, oxy-hemoglobin and deoxy-hemoglobin.

12.   The method of claim 10, wherein said body tissue is breast tissue.

- 16 -

13.   The method of claim 10, wherein said number of wavelengths selected is from 2 to 4.

14.   The method of claim 13, wherein said number is 4.

15.   The method of claim 11, wherein values of said wavelengths are 760 nm, 780 nm, 830 nm and 850 nm.

16.   The method of claim 1, wherein the step of determining an optimal value of said parameters to be optimized comprises:

        deriving an inherent wavelength-dependent sensitivity to noise in calculating said chromophore concentrations, and

        determining an optimal correlation of said sensitivity and at least one other of said parameters.

17.   The method of claim 16, wherein one of said parameters to be optimized is a distribution of an acquisition time at each of said wavelengths.

18.   The method of claim 1, wherein one of said parameters to be optimized is a distribution of an acquisition time at each of said wavelengths.

19.   The method of claim 18, further comprising a step of determining a minimum value for said acquisition time at which said performance of said system attains a minimum threshold value.

20.   The method of claim 1, wherein one of said parameters to be optimized is at least one of said source power and said detector aperture for each of said wavelengths.
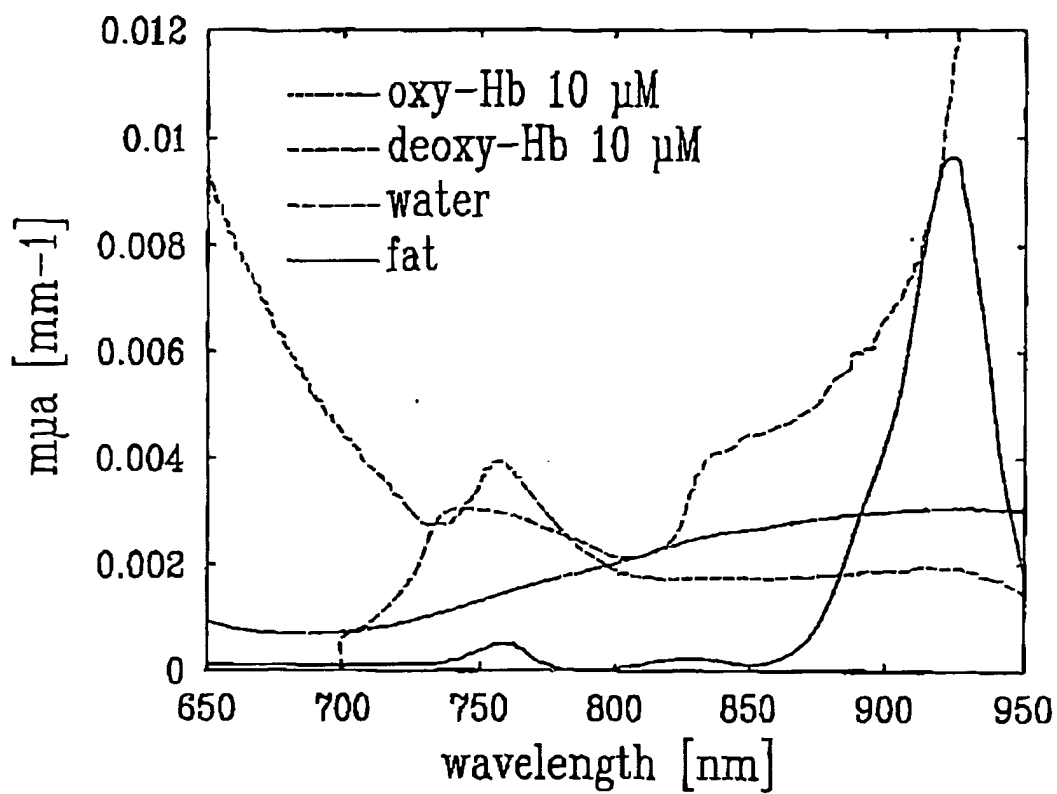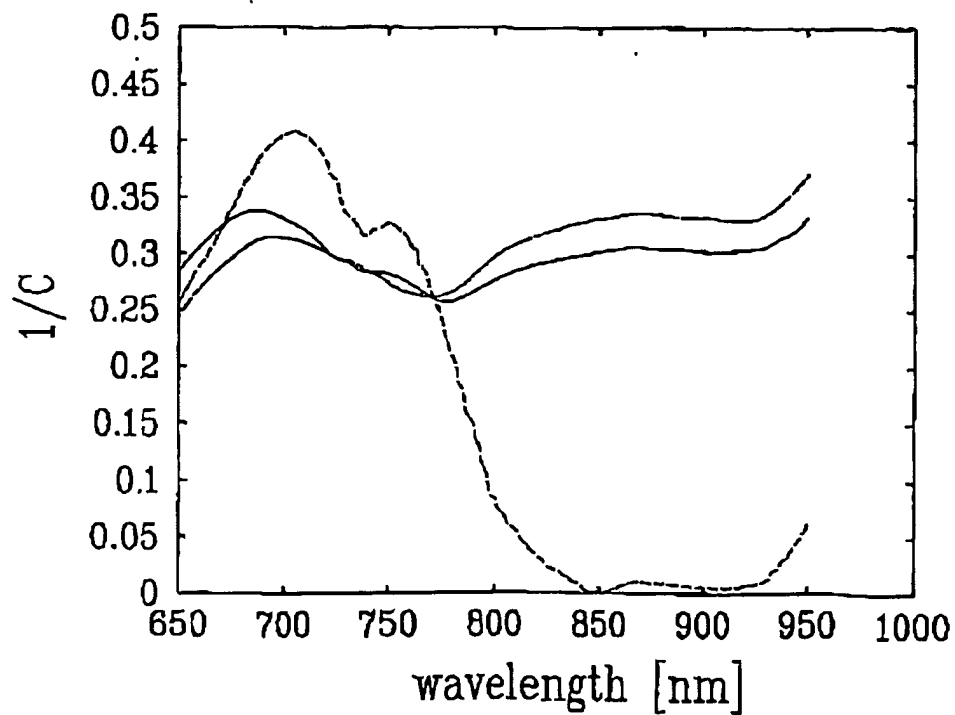
- 17 -

21.   The method of claim 20, further comprising a step of determining a minimum value for an acquisition time at which said performance of said system attains a minimum threshold value.

1/7

Fig. 1

Fig. 2
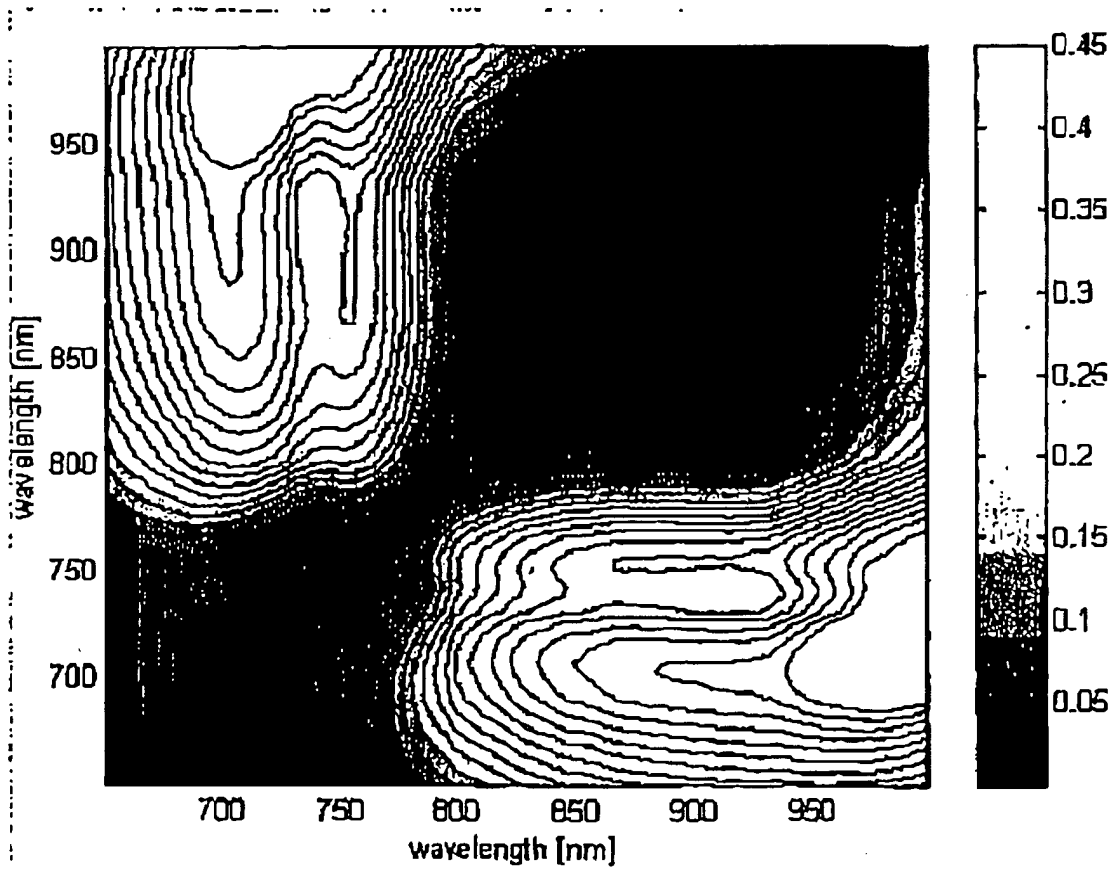
2 / 7

FIG. 3

3/7

assumed lipid concentration/100 [%]

Fig 4

4/7

FIG. 5a

FIG. 5b

5/7

FIG. 6a

FIG. 6b

6/7

FIG. 7

FIG. 8A

FIG. 8B

7/7

FIG 9A

FIG 9B

FIG 10A

FIG 10B
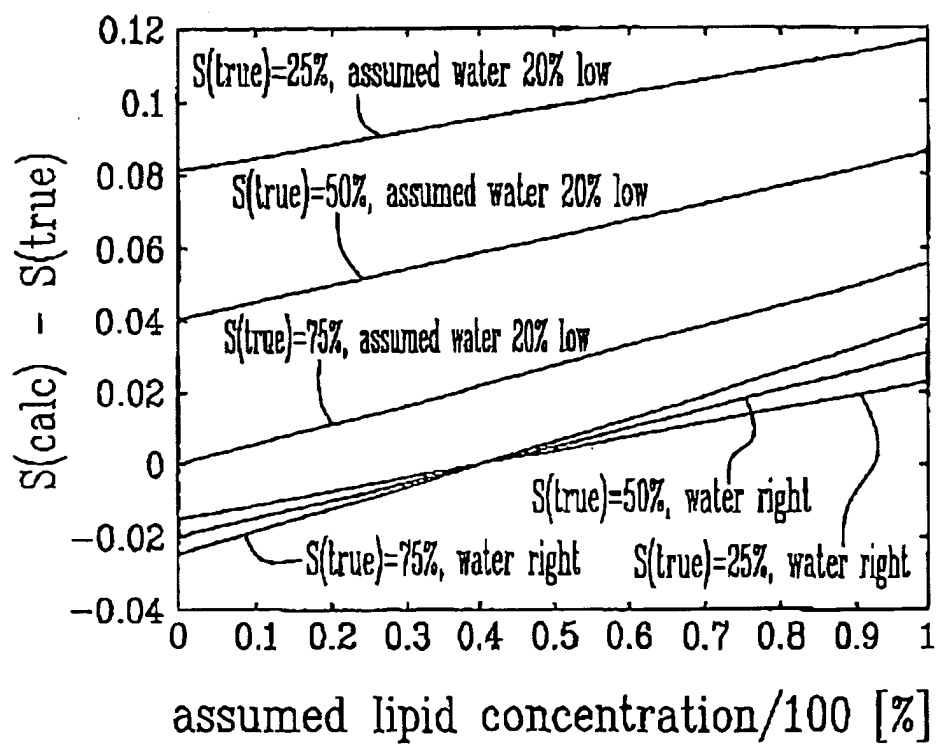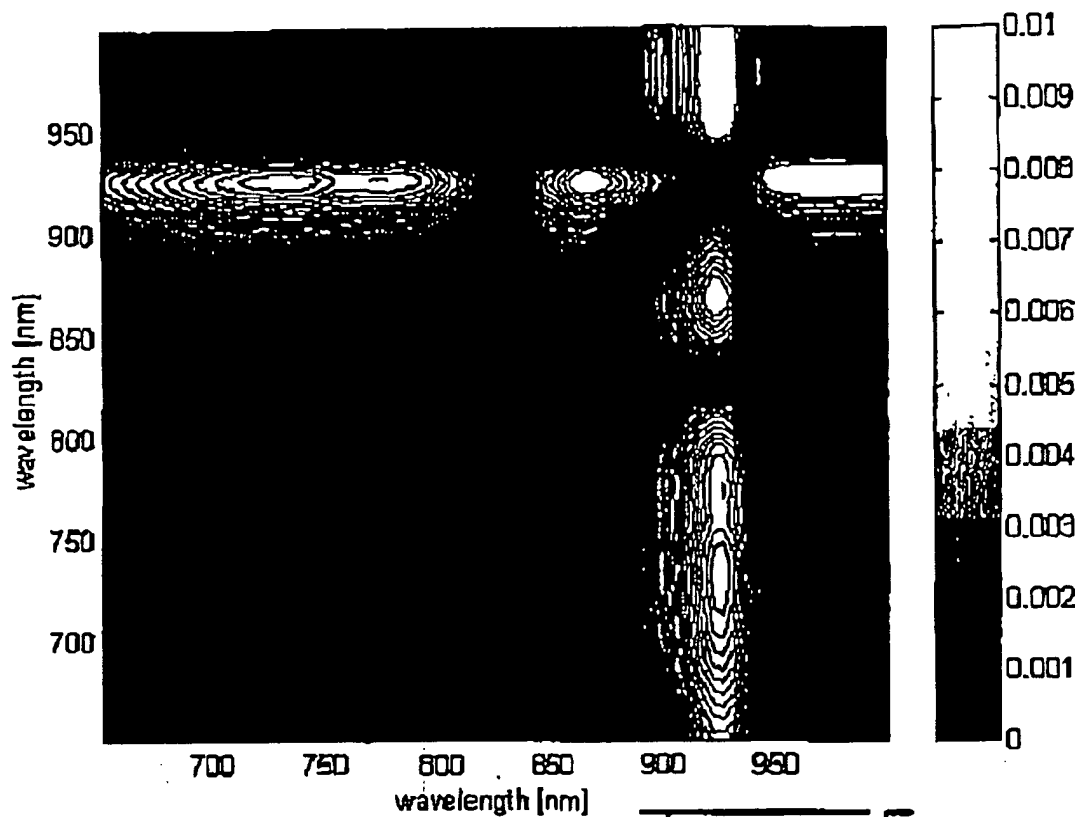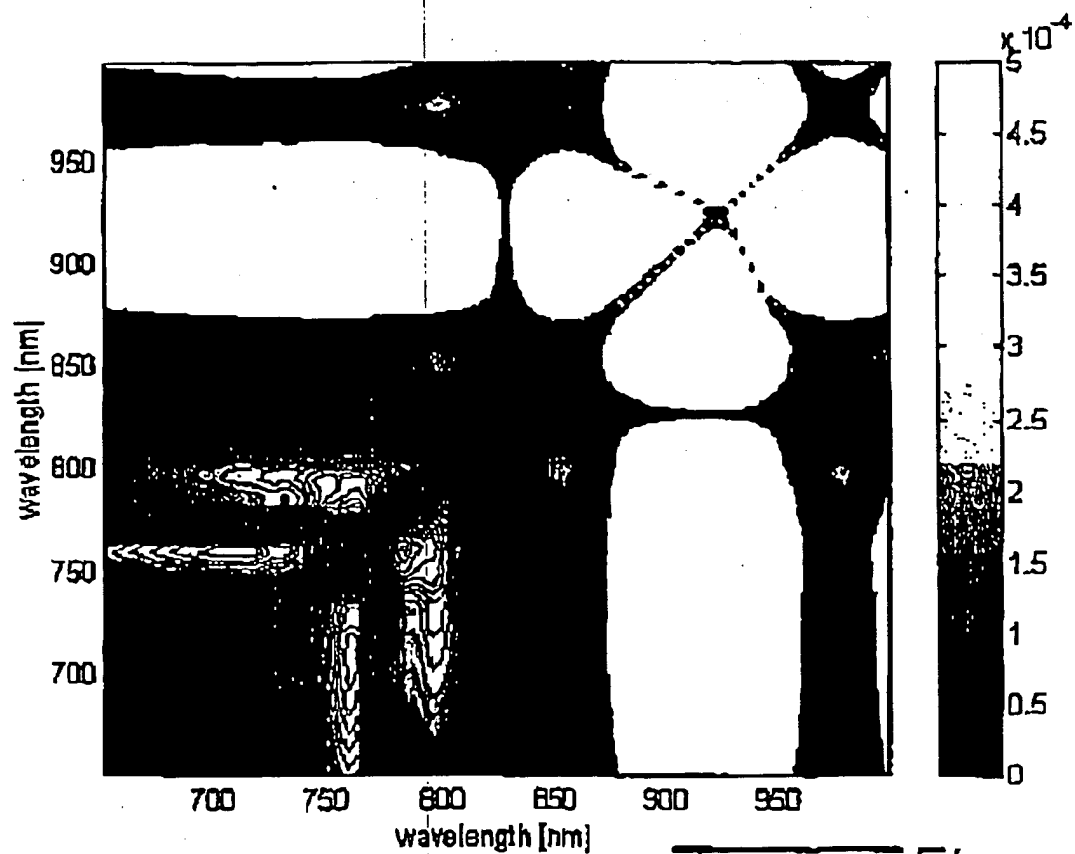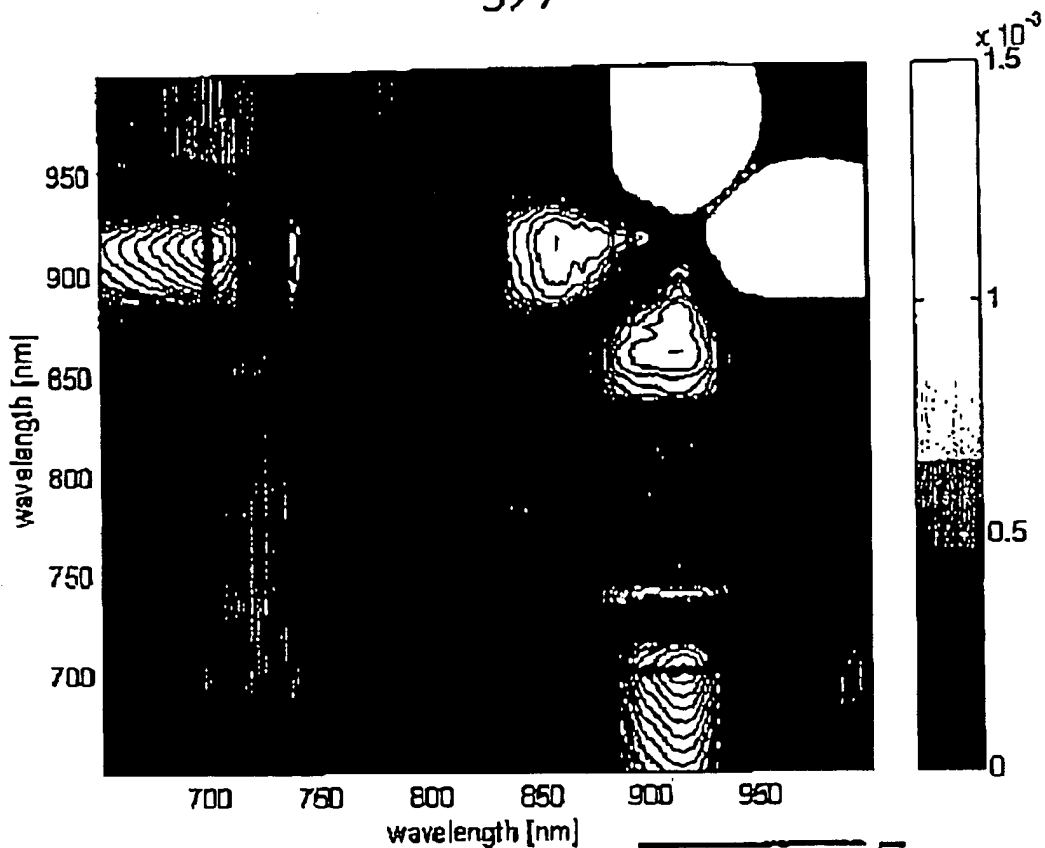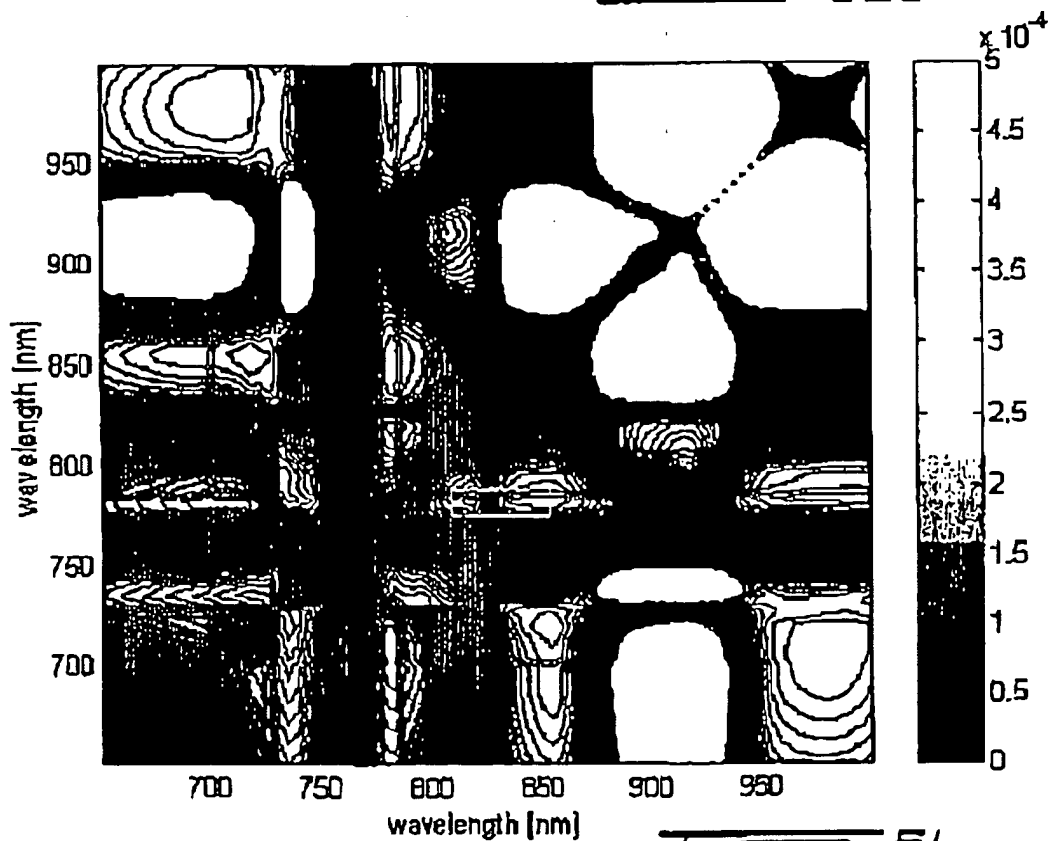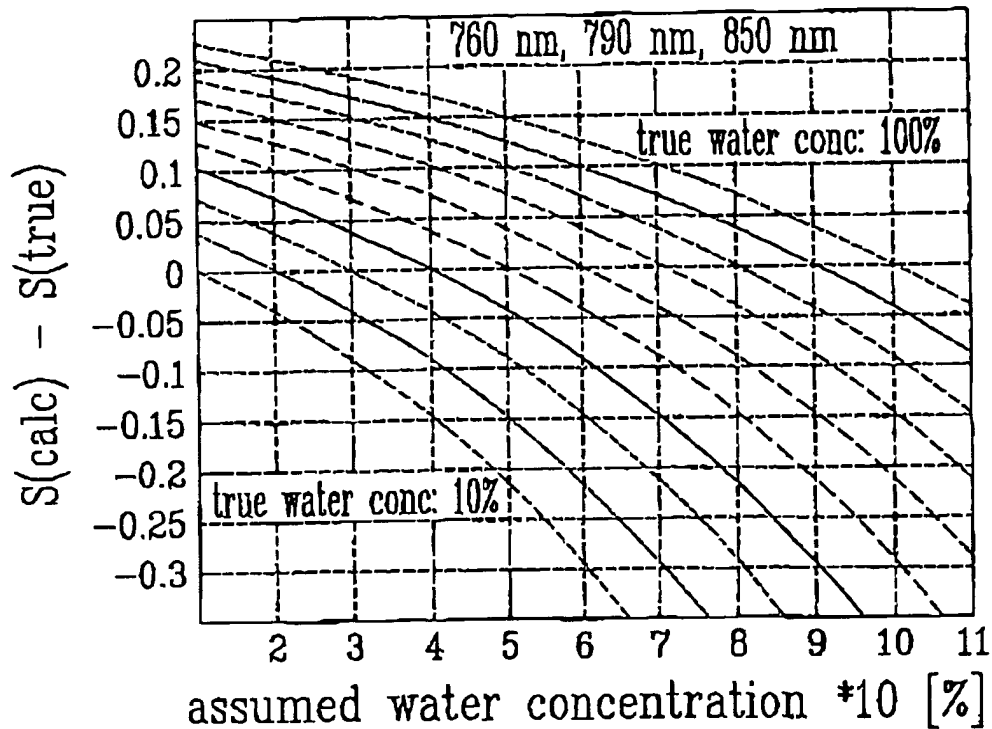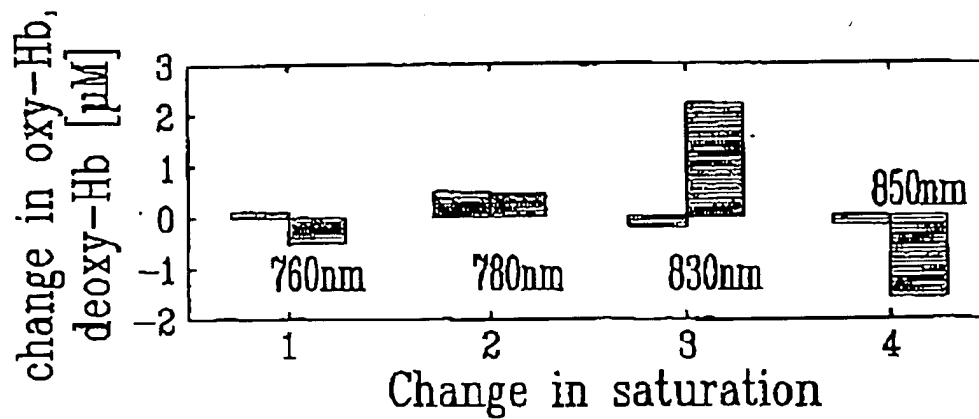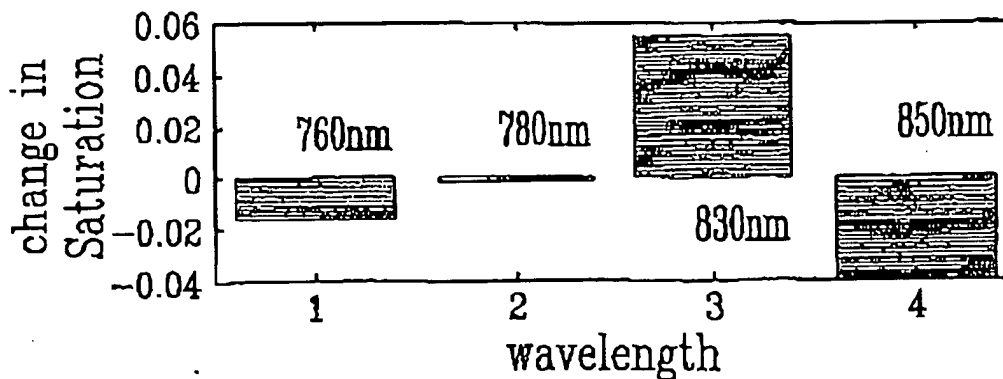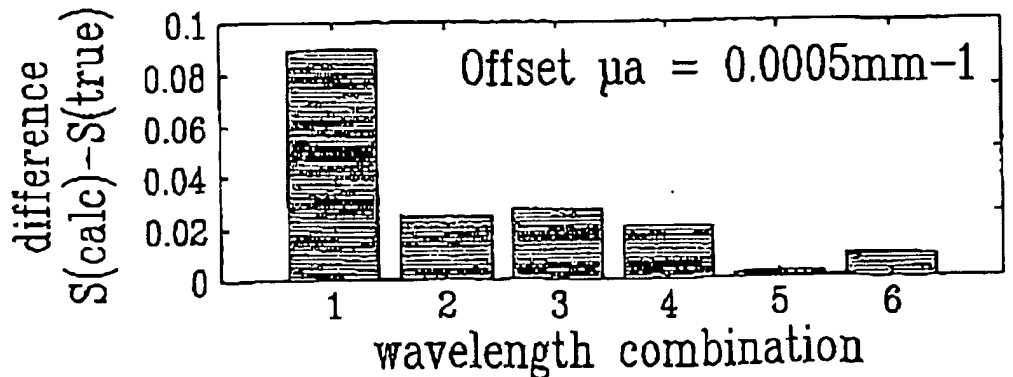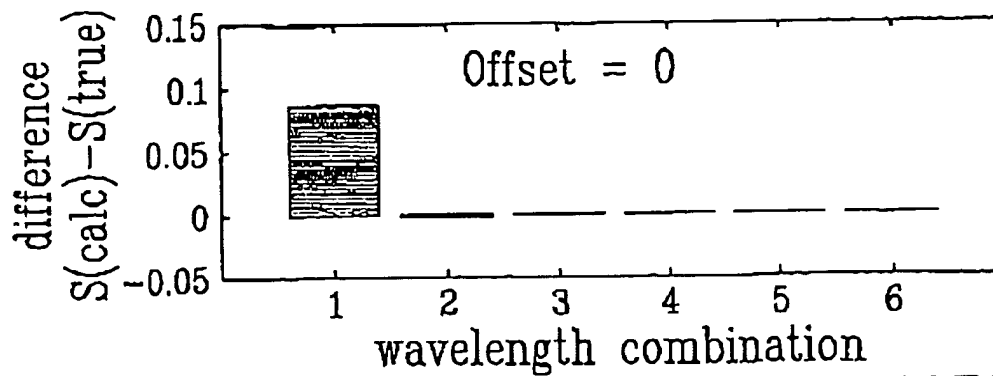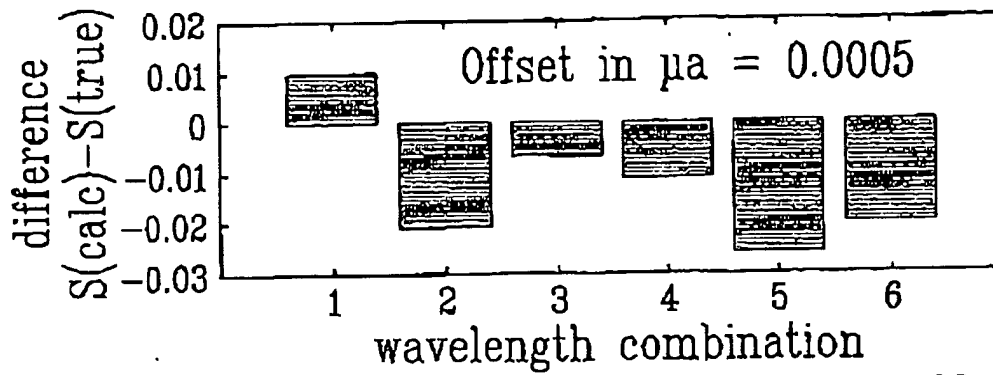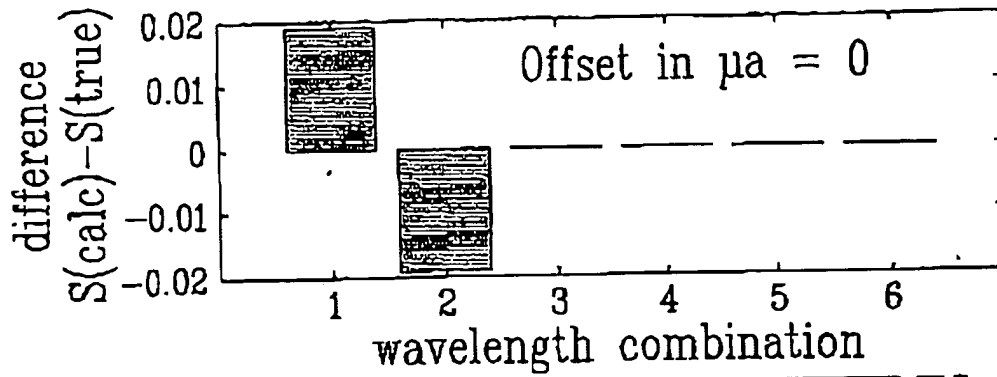
√N 2219   XP-001019599   P. 1153-1164 = ⑩   PD: 01|03|2001

Fiber-optic probe for noninvasive real-time det rmination of tissue optical properties at multiple wavelengths

Jan S. Dam, Carsten B. Pedersen, Torben Dalgaard, Paul Erik Fabricius,
Prakasa Aruna, and Stefan Andersson-Engels

We present a compact, fast, and versatile fiber-optic probe system for real-time determination of tissue optical properties from spatially resolved continuous-wave diffuse reflectance measurements. The system collects one set of reflectance data from six source–detector distances at four arbitrary wavelengths with a maximum overall sampling rate of 100 Hz. Multivariate calibration techniques based on two-dimensional polynomial fitting are employed to extract and display the absorption and reduced scattering coefficients in real-time mode. The four wavelengths of the current configuration are 660, 785, 805, and 974 nm, respectively. Cross-validation tests on a 6 × 7 calibration matrix of Intralipid–dye phantoms showed that the mean prediction error at, e.g., 785 nm was 2.8% for the absorption coefficient and 1.3% for the reduced scattering coefficient. The errors are relative to the range of the optical properties of the phantoms at 785 nm, which were 0–0.3/cm for the absorption coefficient and 6–16/cm for the reduced scattering coefficient. Finally, we also present and discuss results from preliminary skin tissue measurements. © 2001 Optical Society of America

OCIS codes: 170.1470, 170.1580, 170.3890, 170.6510.

1. Introduction

The optical properties of human tissue,[1] i.e., the absorption coefficient μ_a, the scattering coefficient μ_s, and the anisotropy factor g, may provide important information on the composition and the physiological dynamics of the tissue. Whereas μ_a may provide information on tissue chromophores,[2-4] μ_s and g may be used to characterize the form, size, and concentration of various scattering components in the tissue.[5-8]

Owing to the obvious advantages of noninvasive and minimally invasive measurements, determination of tissue optical properties based on diffuse reflectance measurements has a significant potential in biomedical diagnostics and monitoring. Diffuse reflectance measurements may be roughly divided into time-resolved[9,10] (TR), frequency-domain[11,12] (FD),

and spatially resolved continuous-wave[13-21] (cw) methods. Traditionally, TR- and FD-based methods have been considered to be more accurate for absolute determination of optical properties than cw based methods. However, TR and FD methods also require more bulky and expensive equipment, and a larger sample volume, which may restrict some biomedical applications, e.g., implementation in portable monitoring equipment or in endoscopes and catheters. Recent research[19] has shown that cw-based methods may yield absolute determination of the optical properties of tissue with accuracies similar to the TR and FD methods, which makes cw-based methods a better choice for many practical applications.

Continuous-wave diffuse reflectance methods may be further divided into methods based on probes in contact with the tissue and noncontact methods, i.e., image reflectometry. The latter method is advantageous in clinical applications because of the noncontact and thus sterile properties. The advantage of contact probes is that they can be made small and portable. Therefore they are well suited for (a) optical biopsies of body cavities or organs, because a probe may be implemented in existing endoscopic equipment, or (b) for long-time monitoring of tissue optical properties, because the probe may be fixed to the skin and still allow the patient to move around.

J. S. Dam (jan.sorensen_dam@fysik.lth.se), C. B. Pedersen, T. Dalgaard, and P. E. Fabricius are with Bang & Olufsen Medicom a/s, DK-7600, Struer, Denmark. S. Andersson-Engels is with the Department of Physics, Lund Institute of Technology, P.O. Box 118, SE-22100, Lund, Sweden. P. Aruna is with Anna University, 600 025 Madras, India.

Received 26 May 2000; revised manuscript received 7 December 2000.

Temperature Controller

(4)

Laptop PC

(5)

SI Detector

Detector Fiber Fanout   Source Fiber

Temp. Detector

3 cm

Probe Head: Front View

DSP Board

SI Detectors
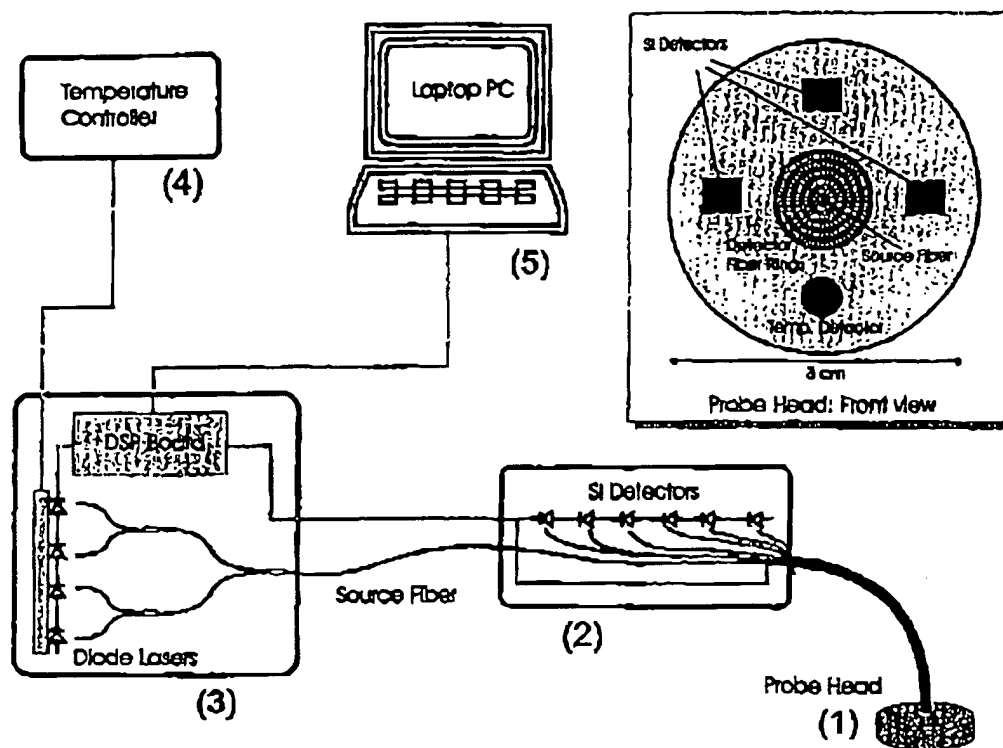
Source Fiber

(2)

Diode Lasers

(3)

Probe Head

(1)

Fig. 1. Diagram of the fiber-optic system for R(r) measurements applied in this paper. (1) Probe head with source and detector optical fibers mounted in a rotational symmetric configuration. (2) Handheld box with silicon photodiodes and amplifier electronics. (3) Stationary box containing a digital signal processing (DSP) board and the light sources in the form of diode lasers. (4) External temperature controller to maintain a constant temperature of the diode lasers. (5) Laptop PC to analyze, display, and store the acquired R(r) data.

However, there are a number of drawbacks related to skin tissue monitoring using a contact probe system. First, the static mechanical pressure of the probe may influence the tissue optical properties, e.g., by displacement of blood in the sample volume. Second, physical activities of the patient may lead to motion artifacts, i.e., movements of the probe relative to the skin tissue. Finally, obstruction of the tissue and sweating may cause long-term changes in the tissue optical properties and the probe–skin optical interface. All such contributions have to be isolated to extract the relevant information from diffuse reflectance measurements.

Accurate closed-form mathematical analytical expressions for spatially resolved diffuse cw reflectance $R(r)$ as a function of the optical properties are strongly limited by requirements to the range of the optical properties and the specific geometry of the setup.[22] Therefore methods based on more-accurate numerical light-propagation models, e.g., Monte Carlo simulations,[23] are often used in conjunction with various forms of multivariate analysis[19,24] to solve the inverse problem of extracting the optical properties from $R(r)$ measurements. However, as a consequence of the similarity principle,[25,26] normally only μ_a and the reduced scattering coefficient $\mu_s' = (1 - g)\mu_s$ are extracted from $R(r)$ measurements.

In this paper we present a fiber-optic probe system for in vivo real-time determination of tissue optical properties based on $R(r)$ measurements at four arbitrary wavelengths. The probe system collects the diffuse reflectance at six distances, extracts the corresponding μ_a and μ_s', and displays the results immediately on a laptop personal computer (PC). The prediction of μ_a and μ_s' is based on multiple polynomial regression[27] and calibration on a set of Intralipid–dye phantoms with well-known optical properties within a range typical for biologic tissue[28] in the visible and the near-infrared regions. In the following sections we first give a description of the probe specifications and the principles of the calibration and prediction algorithms. Next, we present and discuss the results obtained from phantom measurements and simulated numerical tests with respect to prediction errors, robustness, and the like. Finally, we present the results of preliminary prediction tests obtained from a series of clinical measurements on normal skin tissue.

2. Materials and Methods

A. Fiber Probe System

Figure 1 shows the basics of the fiber probe system we used for the measurements described below. The

system consists of a probe head with a 200-μm source fiber in the center surrounded by five equally spaced concentric rings of 250-μm detector fibers. We chose this ring geometry instead of, e.g., a simpler linear geometric configuration, in part to be able to collect more light at farther distances and in part to minimize any problems arising from tissue inhomogeneities during clinical measurements. The fibers of each single ring detector are bundled and terminated on separate silicon photodiodes. In addition, three photodiodes and a temperature sensor are mounted directly near the perimeter of the probe head. Thus $R(r)$ can be collected at six distances, in part at the five fiber rings ($r = 0.6, 1.2, 1.8, 2.4,$ and 3.0 mm) and in part at the directly mounted photodiodes ($r = 7.8$ mm). These distances were chosen on the basis of previous studies.[19] The gain of each reflectance detector was calibrated in an integrating sphere setup to obtain equal outputs at constant input light intensities. The source fiber is coupled into four separate fibers, each connected to four replaceable low-power diode lasers. The diode lasers are mounted on a heat sink with a constant temperature maintained by an external controller. Furthermore, a separate reference detector monitors the output of the source fiber at the probe head. The diode lasers may be selected arbitrarily to suit different applications. In this paper we used diode lasers with the wavelengths 660, 785, 805, and 974 nm, which are well suited for applications involving hemodynamic monitoring. The data acquisition and storage is controlled by a laptop PC connected to a digital signal processing (DSP) board. In each $R(r)$ measurement the detector hardware collects data simultaneously in eight parallel channels from the probe head, i.e., from the six detector rings, from the reference detector at the source fiber, and from the temperature sensor. One cycle of four successive measurements (i.e., one at each wavelength) including dark measurements may be performed in ~10 ms; thus the maximum sampling rate of the system is ~100 Hz. To minimize any interference from background light or drift of the light source, the dark measurements are subtracted from the measured reflectance data after which they are normalized relative to the source reference. The DSP board accomplishes this prior to when the data are analyzed, displayed, and stored by the PC.

B. Calibration and Prediction Algorithms

In theory, μ_a and μ_s' may be determined with $R(r)$ data from only two of the six detector distances of the fiber probe. Building on our previous research,[19,27] we thus applied multiple polynomial regression (MPR) to create a calibration model and subsequently extract μ_a and μ_s' from $R(r)$ measurements at $r_1 = 0.6$ mm and at $r_2 = 7.8$ mm. For the sake of clarity we give a summary of the MPR method here. We first measure $R(r)$ at r_1 and at r_2 for a set of calibration samples with well-defined optical properties and de-

note them $R_{1,cal}$ and $R_{2,cal}$. Then we find a double-polynomial fit to $R_{1,cal}$ and $R_{2,cal}$:

$$R_{1,fit}(\mu_a, \mu_s', m) = (a_0 + a_1\mu_a + a_2\mu_a^2 + \ldots a_m\mu_a^m)$$
$$\times (b_0 + b_1\mu_s'^2 + \ldots b_n\mu_s'^m),$$

$$R_{2,fit}(\mu_a, \mu_s', m) = (c_0 + c_1\mu_a + c_2\mu_a^2 + \ldots c_m\mu_a^m)$$
$$\times (d_0 + d_1\mu_s'^2 + \ldots d_n\mu_s'^m), \quad (1)$$

Where a, b, c, and d are fitting coefficients determined by least-squares regression. $R_{1,fit}$ and $R_{2,fit}$ thus constitute the calibration model. The next step is to solve the inverse problem of determining μ_a and μ_s' from $R(r)$ measurements on a set of prediction samples, i.e., $R_{1,meas}$ and $R_{2,meas}$. First we define

$$F(\mu_a, \mu_s') = R_{1,fit} - R_{1,meas},$$

$$G(\mu_a, \mu_s') = R_{2,fit} - R_{2,meas}. \quad (2)$$

Then we use a Newton–Raphson algorithm to perform converging iterative calculations of μ_a and μ_s':

$$-\begin{bmatrix} F(\mu_{a,k}, \mu_{s,k}') \\ G(\mu_{a,k}, \mu_{s,k}') \end{bmatrix} = \begin{bmatrix} \dfrac{\partial F}{\partial \mu_a} & \dfrac{\partial F}{\partial \mu_s'} \\ \dfrac{\partial G}{\partial \mu_a} & \dfrac{\partial G}{\partial \mu_s'} \end{bmatrix} \begin{pmatrix} h_{a,k} \\ h_{s,k} \end{pmatrix}$$

$$\begin{pmatrix} \mu_{a,k-1} \\ \mu_{s,k-1}' \end{pmatrix} = \begin{pmatrix} \mu_{a,k} \\ \mu_{s,k}' \end{pmatrix} + \begin{pmatrix} h_{a,k} \\ h_{s,k} \end{pmatrix}$$

$$k = 0, 1, 2, 3, \ldots, \quad (3)$$

where k is an index and h_a and h_s are correction terms of μ_a and μ_s'. The iterations were stopped when both h_a and $h_s < 1 \times 10^{-8}$ (cm^{-1}). With such strict criteria, previous research[27] showed that the contribution of the Newton–Raphson method to the total prediction error was negligible.

Since in this study we want to extract two optical properties only, i.e., μ_a and μ_s', the MPR method implies exactly two input variables as well, i.e., $R(r_1)$ and $R(r_2)$. However, owing to tissue inhomogeneity and/or noisy measurement conditions, it might be advantageous to include more source–detector distances during measurements and then subsequently apply some sort of dimension-reduction method before the data are fed into the MPR method. To test such a procedure, we also applied principal component analysis (PCA) on the data from all six source-detector distances of the probe system and then used the resulting two main principal components P_1 and P_2 as input to the MPR method instead of $R(r_1)$ and $R(r_2)$.

All the prediction algorithms we applied in this paper were implemented in Matlab and run on a 166-MHz PC. With this configuration, the prediction of a single set of μ_a and μ_s' could be performed in ~60 ms.

Table 1. Optical Property Ranges of 6×7 Matrix of Intralipid-Ink
Phantoms Determined from Integrating Sphere Measurements

λ (nm)	Optical Property Range (cm^{-1})	
	μ_a	μ_s'
660	0–0.36	7.3–19.5
785	0–0.32	6.1–16.3
805	0–0.31	6.0–16.0
974	0.45–0.68	4.8–12.7

C. Phantoms

Because of the unknown numerical apertures of the fiber probe light source and detectors, we chose to calibrate the system directly on a set of phantoms instead of using a mathematical light-propagation model. The phantoms consisted of well-defined aqueous solutions of Intralipid and black ink in cylindrical glass containers with a diameter of 10 cm and a height of 4 cm. We determined the scattering and absorption spectra of the Intralipid and the black ink from integrating sphere[27] and traditional transmission spectroscopy measurements. On the basis of these spectra, we mixed a 6 × 7 matrix of phantoms with μ_a and μ_s' ranges typical for skin tissue (see Table 1). The applied ranges of Intralipid concentrations were 0.6, 0.8, ..., 1.6%, and the range of the ink concentrations were 0.0, 0.2, ..., 1.2%. It should be noted that the absorption of pure ink is much higher than that of typical biologic substances; thus the ink concentrations in the following refers to a premixed basic ink–water solution with a biologically relevant absorption level. To perform the prediction experiments, we calibrated the probe system directly to the concentrations of the Intralipid and the ink in the phantoms, assuming that both the absorption of pure Intralipid[29,30] and the scattering of the ink were negligible. At 660, 785, and 805 nm we assumed that the background absorption was negligible as well. However, water exhibits substantial absorption[31] at 974 nm ($\mu_{a,water}$ = 0.45 cm^{-1}). This was incorporated in the concentration-to-absorption tabulation by assuming a constant water absorption contribution at this particular wavelength (i.e., c_{ink} = 0% ⇒ μ_a = 0.45 cm^{-1}).

3. Results

Once the 6 × 7 matrix of phantoms was mixed, we determined the actual optical properties of a subset of the phantom matrix, using integrating sphere measurements. Figure 2(a) shows the mean absorption spectra of the six phantoms with 1% ink concentrations but varying Intralipid concentrations, and Fig. 2(b) shows the mean scattering spectra of the seven phantoms with 1% Intralipid concentrations but varying ink concentrations. We used the results from Fig. 2(a) to relate the concentrations of Intralipid and ink to the optical properties of the phantoms. The resulting optical property ranges of the 6 × 7 matrix phantoms are listed in Table 1.

Figures 3(a) and 3(b) show the measured intensity

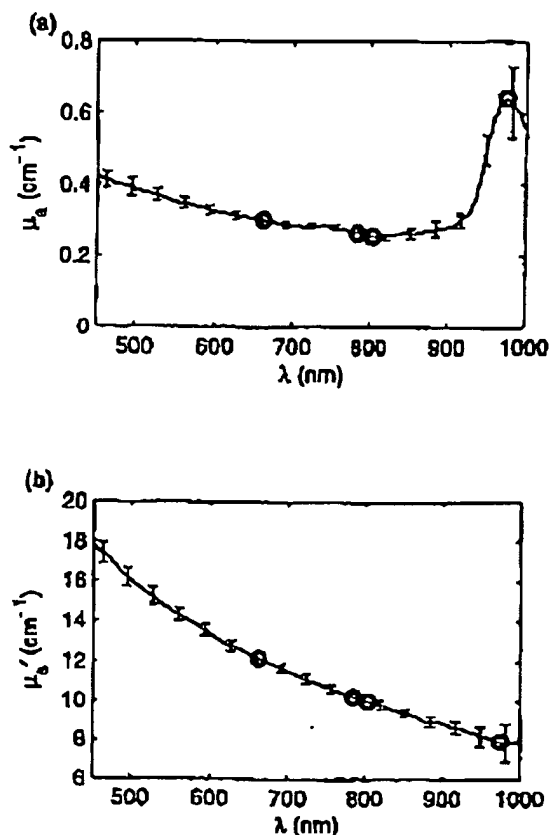Fig. 2. Optical property spectra of the applied Intralipid-ink phantoms. (a) Mean of μ_a as a function of the wavelength λ for the six phantoms with 1% ink concentration but varying Intralipid concentrations. (b) Mean of μ_s' as a function of the wavelength for the seven phantoms with 1% Intralipid concentration but varying ink concentrations. The error bars of the spectra in panels (a) and (b) show the standard deviations of μ_a and μ_s', respectively. The circles indicate the values at the four wavelengths of the probe. The two spectra were measured and calculated with an integrating sphere setup in conjunction with the MPR method.

$R(r)$ at 785 nm as a function of μ_a and μ_s' at $r = 0.6$ mm and $r = 7.8$ mm, respectively. Corresponding plots at the three remaining wavelengths of the probe, i.e., 660, 805, and 974 nm, showed similar characteristics; i.e., they were also smooth and monotonic, which suggests that they may be fitted well by Eq. (1) with relatively low-order polynomials. Preliminary experiments showed that using Eq. (1) with $m = 3$ provided the best overall calibration model, concerning accuracy and robustness. The prediction accuracy of the MPR method was tested with leave-one-out cross validation. This means that we successively performed predictions with the data from one phantom for prediction and the data from the remaining 41 phantoms of the 6 × 7 matrix for calibration. To ensure that all $R(r)$ variations were covered by the calibration models, we carried out predictions only on the 4 × 5 interior subset of the 6 × 7 matrix. Table 2 presents the results from these cross-validation prediction tests.
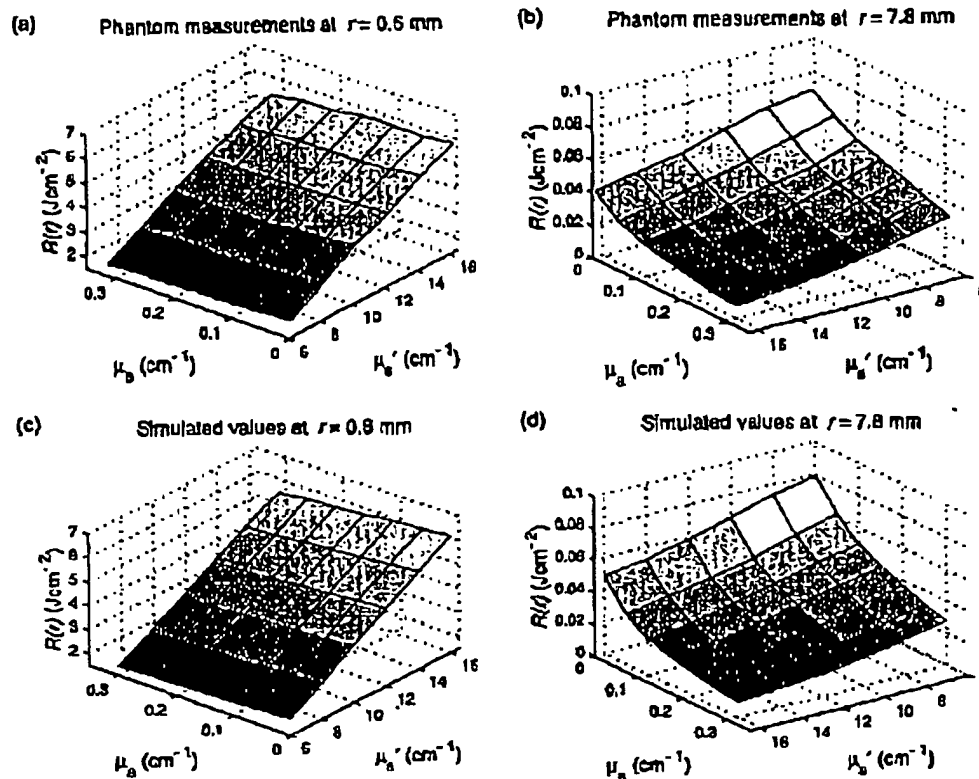
Fig. 3. Surface plots of $R(r)$ at $r_1 = 0.6$ mm and $r_2 = 7.8$ mm as a function of μ_a and μ_s'. Panels (a) and (b) show the $R(r)$ plots of the 6×7 Intralipid phantoms at 785 nm, and panels (c) and (d) show the corresponding $R(r)$ plots based on Monte Carlo simulations. Note that the arbitrary intensity units of measured $R(r)$ plots have been scaled in order to compare them with the simulated plots.

To check our experimental results, and to examine the robustness, noise sensitivity, and so on, of the applied calibration model and prediction algorithms, we also performed a series of numerical tests based on Monte Carlo simulations with a geometric configuration analogous to the fiber probe setup described in Subsection 3.A. However, unlike the measurements, the simulations were based on a collimated incident beam, a semi-infinite medium, and $\frac{1}{2}\pi$ acceptance angle for collection of the diffuse reflectance. The tests were carried out as follows: (I) First, we generated a basic 6×7 calibration matrix with optical properties corresponding to the 6×7 phantom

Table 2. Leave-One-Out Cross-Validation Prediction Tests Based on Phantom Measurements[a]

| | Prediction Errors (%) | | | |
| | μ_a | | μ_s' | |
λ (nm)	Mean	Max	Mean	Max
600	3.3 (2.5)	18 (6.7)	1.7 (1.7)	3.7 (4.0)
785	2.8	8.3	1.3	3.4
805	2.6	9.0	1.5	4.2
974	3.7	9.7	1.6	3.8

[a]The errors are relative to the ranges of μ_a and μ_s' of the phantoms. The bracketed values at $\lambda = 660$ nm have been corrected for an outlier detected by visual inspection of the measured $R(r)$ data.

matrix at $\lambda = 785$ nm and then performed prediction tests similar to the phantom cross-validation tests described above. Figure 4 shows a selected set of $R(r)$ profiles from these simulations [see also Figs. 3(c) and 3(d)]. (II) Next, to test the algorithms with independent calibration and prediction data, we generated a series of 20 $R(r)$ data sets with random μ_a and μ_s' distributions and then performed predictions on this randomized set with a calibration model based on the full 6×7 basic matrix. (III) The basic 6×7 matrix was generated with 1×10^6 photons. To examine the impact of random measurement noise on the prediction performance, we generated a second 6×7 matrix with less noise by using 1×10^7 photons and performed identical cross-validation tests on this set. (IV) We also wanted to investigate the effect of using a calibration model with a higher μ_a and μ_s' resolution; thus we also carried out cross-validation tests on a 11×13 calibration matrix with the same μ_a and μ_s' range and number of photons as the basic 6×7 matrix. (V) Finally, we tested the effect of using PCA for dimension reduction as described in Subsection 3.B. The resulting mean and maximum prediction errors from the numerical tests (I–V) described above are summarized in Fig. 5.

To validate the optical property range of the applied calibration model, we performed a series of
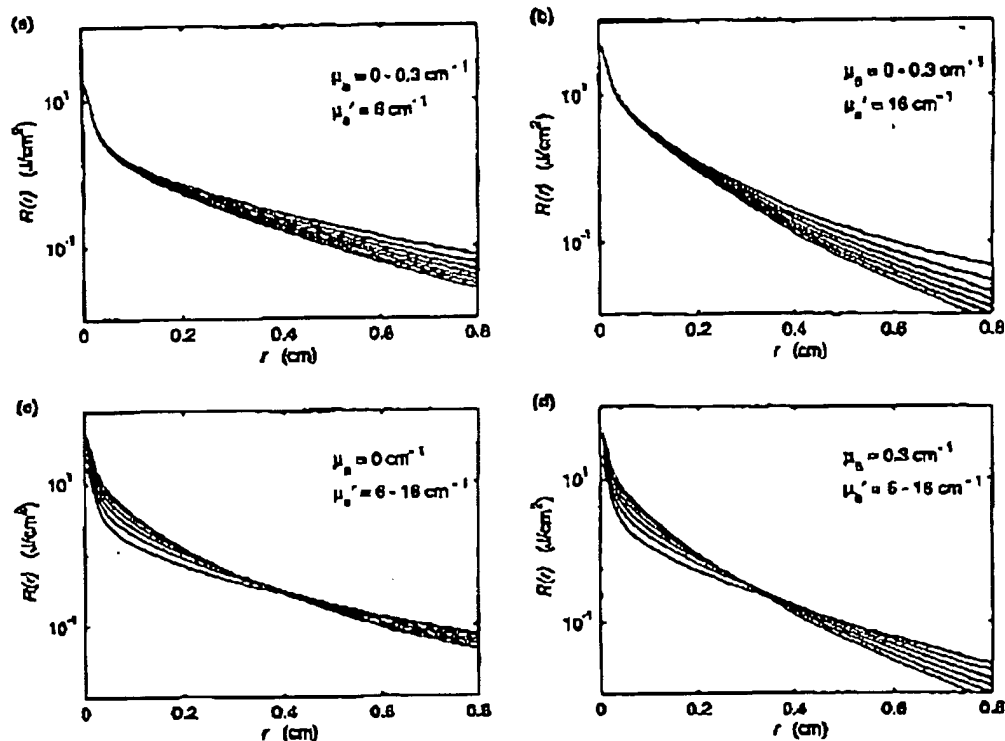
Fig. 4. Monte Carlo simulated $R(r)$ data for various combinations of μ_a and μ_s' within ranges typical for skin tissue at 785 nm. In (a) and (b), μ_s' is kept constant at 8 cm^{-1} and 16 cm^{-1}, respectively while μ_a is varied within the range 0–0.3 cm^{-1}. In (c) and (d) μ_a is kept constant at 0 cm^{-1} and 0.3 cm^{-1}, respectively, whereas μ_s' is varied within the range 6–16 cm^{-1}.

probe measurements on the inner forearm of five healthy individuals. Figure 6 shows how the mean $R(r)$ of all five individuals (circles) at each probe distance is situated relative to the $R(r)$ ranges of the calibration model (vertical bars). Figure 6 also shows the predicted optical properties at all four wavelengths calculated from the mean $R(r)$ data with Eq. (1)-(3). It can be seen that the measured skin tissue at $\lambda = 660$ nm and $r = 7.8$ mm is outside the calibration model range, and therefore it is not possible to predict μ_a and μ_s' correctly in this case.

4. Discussion

A. Geometry Considerations

In Fig. 4(a) and 4(b) μ_s' is kept constant at values of 6 and 16 cm^{-1}, respectively. In these two cases, it appears that changes in μ_a have a negligible effect on $R(r)$ at distances close to the source. In Figs. 4(c) and 4(d), μ_a is kept constant at values of 0 and 0.3 cm^{-1}, respectively. Here it is notable that there is very little variation in $R(r)$ at $r \sim 0.35$ cm in Fig. 4(c) and at $r \sim 0.3$ in Fig. 4(d). Using a figure of speech, we say that there is a *pivot point* in the $R(r)$ graphs at $r \sim 0.3$ cm, when μ_a is kept constant. The simulations in Figs. 4(a) and 4(b) indicates that μ_s' may be determined with good accuracy from close distance measurements only. To determine μ_a as well, Figs. 4(c) and 4(d) suggest that $R(r)$ measurements close to the pivot point should be included, since there is little

variation in $R(r)$ as a function of μ_a at this point. Although, other authors[32,33] support this argument, we based our experiments in this paper on close range distances in conjunction with distances well beyond the pivot point. We did this because our previous studies[19] showed that this geometrical configuration provided a better accuracy than a configuration with close range distances in conjunction with distances near the pivot point.

B. Phantom Measurements

The prediction tests using Intralipid–ink phantoms show a good accuracy (see Table 2). The mean prediction errors at all four wavelengths is roughly 3% for μ_a, and 1.6% for μ_s', whereas the maximum prediction errors for μ_a and μ_s' are approximately 11% and 4%, respectively. The prediction algorithm converged in all cases; however, the maximum error of μ_a at $\lambda = 660$ nm is remarkably high (18%). A visual inspection of the raw $R(r)$ data at 660 nm revealed an outlier at $r = 7.8$ mm in one of the phantom measurements. This outlier could be due to an air bubble or a piece of dirt at one of the three 7.8-mm detectors in this particular measurement. When we removed the outlier from the calibration and prediction analysis at $\lambda = 660$ nm, we obtained the improved results shown in brackets in Table 2. In general, the prediction errors of μ_a are approximately twice as high as the errors of μ_s'. This may be attributed in part to the fact that μ_a is mainly deter-
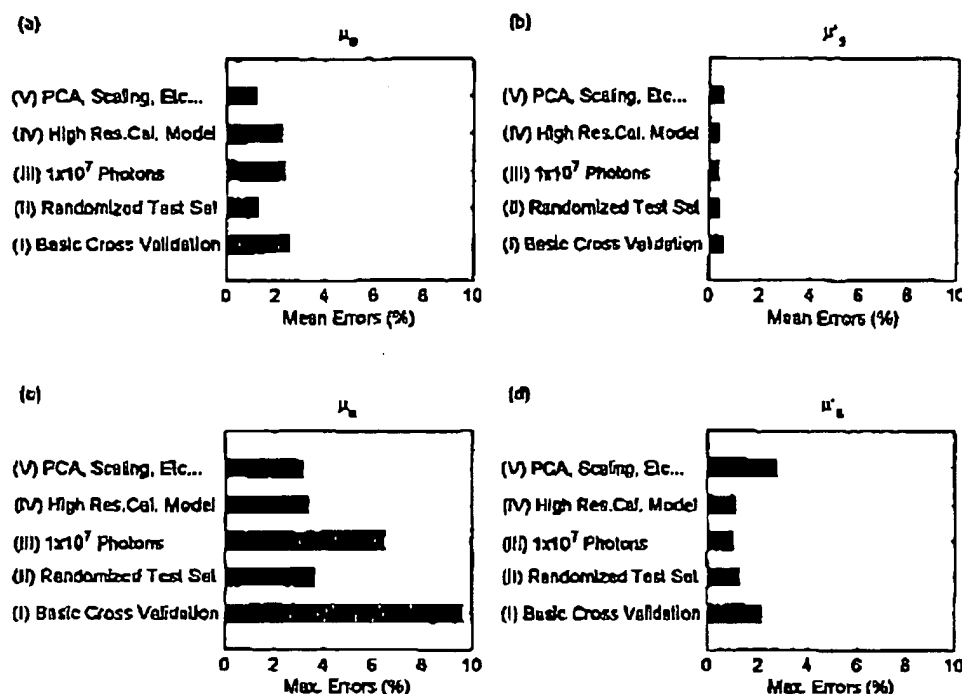
Fig. 5. Various numerical tests on Monte Carlo simulated $R(r)$ data. Panels (a) and (b) show the mean prediction errors of μ_a and μ_s', respectively. Panels (c) and (d) show the corresponding maximum prediction errors. From below: (I) cross validation on a basic 6 × 7 calibration matrix (10^6 photons) corresponding to phantom measurements at 785 nm, (II) predictions on data with random μ_a and μ_s' distribution, (III) cross validation on 6 × 7 matrix generated with 1 × 10^7 photons, (IV) cross validation on a high-resolution 11 × 13 calibration matrix, (V) cross validation on the basic 6 × 7 calibration matrix with principal component analysis.

mined on the basis of the $R(r)$ data at $r = 7.8$ mm, whereas μ_s' is almost solely determined from $R(r)$ data at $r = 0.6$ mm, where the signal level is ~1000 times the level at $r = 7.8$ mm. The μ_a predictions are therefore more sensitive to any background noise interference during the measurements.

With reference to the comments on the pivot point in Subsection 5.A we also performed a series of prediction tests, in which we replaced the $R(r)$ probe data at $r_2 = 7.8$ mm with probe data at the pivot point $r_{pivot} = 8.0$ mm. This had no significant effect on the μ_s' prediction errors, but both the mean and the maximum μ_a prediction errors increased ~30% compared with results reported in Table 2.

C. Numerical Tests

The general shape of the measured and the simulated $R(\mu_a, \mu_s')$ plots in Fig. 3 are very similar at corresponding detector distances. However, the simulated plots do show slightly higher $R(\mu_a, \mu_s')$ levels for low μ_a and μ_s' values at $r = 7.8$ mm. This difference is severe enough to prevent the direct use of a calibration model based on Monte Carlo simulations for prediction analyses of $R(r)$ data collected with the fiber probe. The difference between the simulated and the measured $R(r)$ data in Figs. 3(b) and 3(d) may be attributed to the different numerical apertures of the sources and the detectors in the two cases; e.g., the Monte Carlo simulations employ a

collimated source beam, whereas the probe source beam is divergent.

The μ_a prediction errors of the simulated data shown in Figs. 5(a) and 5(c) are comparable with the errors of the measured data Table 2, whereas the μ_s' prediction errors of the simulated data [Figs. 5(b) and 5(d)] are lower than the errors of the measured data. In both cases the μ_a prediction errors are significantly higher than the μ_s' errors, probably owing to the noise sensitivity at $r = 7.8$ mm as discussed above. Figure 5 also shows a drop in the prediction errors when a randomized prediction data set is used. This may be because the quality of the calibration model fit during leave-one-out cross validation is reduced in the vicinity of the μ_a and μ_s' to be predicted.

From Fig. 5 it also appears that a reduction in measurement noise (i.e., more photons) or use of a calibration model with a higher μ_a and μ_s' resolution in both cases lead to a significant drop in maximum prediction errors, whereas the effect on the mean prediction errors is moderate. Finally, it can be seen from Fig. 5 that the use of PCA before calibration and prediction has a positive effect on the μ_a prediction errors, whereas the μ_s' prediction errors are slightly increased. In summary, the prediction accuracies obtained from calibration and prediction on phantoms are comparable with the accuracies obtained from calibration and prediction on Monte Carlo simulated data. The numerical tests suggest that the
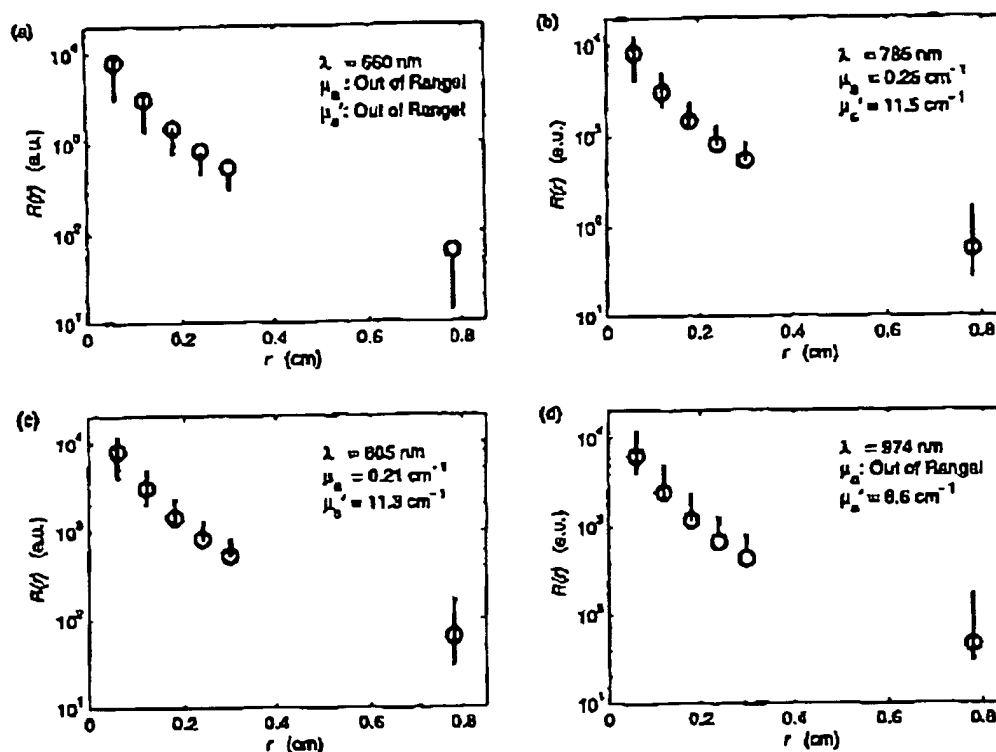
Fig. 6. Mean optical properties at all four wavelengths determined from R(r) measurements on the forearm of five healthy individuals. The vertical bars indicate the valid range of the applied calibration model at various distances and wavelengths, and the circles indicate the mean measured R(r) of the five individuals. At each of the four wavelengths, the stated values of μ_a and μ_s' were determined on the basis of the mean R(r) values at $r_1 = 0.6$ mm and $r_2 = 7.8$ mm.

prediction accuracy may be improved slightly by use of more samples during creation of the calibration model. However, the improvements may hardly justify the additional efforts of creating more calibration phantoms.

D. Clinical Measurements

From Fig. 6 it appears that the range of calibration model covers the span of the measured tissue R(r) data in most cases, except at $\lambda = 660$ nm. At this wavelength the mean of the measured R(r) at $r_2 = 7.8$ mm is above the range of the calibration model. This suggests that either μ_a or μ_s' (or both) of the skin tissue is lower than the minimum values of the calibration model. In the case of μ_a this is not possible, since the model range at $\lambda = 660$ nm is 0–0.36 cm^{-1}. The minimum value of μ_s' of the model at this wavelength is 7.3 cm^{-1}, and it is not likely that the measured μ_s' should be beneath this limit either. At the three remaining wavelengths the measured R(r) at $r_1 = 0.6$ mm and $r_2 = 7.8$ mm are within the limits of the calibration mode, and the extracted μ_a or μ_s' shows a reasonable correlation with other studies.[20,34] However, at 974 nm, it appears that the measured R(r) data, at some of the intermediate distances (i.e., at $r = 2.4$ and 3.0 mm), are not within the ranges of the calibration model; i.e., the shape of the tissue R(r) profiles are different from the shape of phantom profiles. There may be several reasons for this. First,

in contrast to the phantoms, the volume of the skin tissue sampled by the probe is not homogeneous but basically consists of distinct layers, i.e., the stratum corneum, the vivid epidermis, the epidermis, and so on. Each of these layers has specific optical properties, and therefore the predicted values of μ_a or μ_s' in Fig. 6 are a compound of the optical properties of each separate layer. Second, the ratio of the refractive indices between the probe and the sample (n_{probe}/n_{sample}) is different in the two cases; i.e., $n_{tissue} \approx 1.40$ (Ref. 35) and $n_{phantom} \approx 1.33$. Finally, the probe–tissue interface may not have been optimal, which in turn may lead to light piping effects between the probe and the stratum corneum. Such effects may cause an increase of the farther R(r) values relative to the values close to the light source, which also might explain the out-of-range problems encountered at $\lambda = 660$ nm. To summarize, it is essential to ensure a proper optical contact and apply a uniform and reproducible mechanical pressure in order to obtain valid predictions from contact probe measurements.

E. Acquisition and Analysis Speed

As stated in Subsection 3.A, the maximum acquisition rate of the fiber probe system for all four wavelengths is ~100 Hz, which is sufficient for analyzing the optical property dynamics of most physiological systems. The current software implementation of the prediction algorithms leads to an analysis time

for one set of μ_a or μ_s' of ~50 ms, i.e., an analysis rate of 5 Hz when all four wavelengths are included. To match the analysis rate to the acquisition rate of the probe system, the speed of the prediction algorithms may be increased substantially by application of a more contemporary PC and/or by compiling the algorithms in, e.g., the C programming language.

5. Conclusions

We have demonstrated a versatile, fast, and accurate probe system for real-time noninvasive determination of tissue optical properties from continuous wave (cw) spatially resolved diffuse reflectance measurements. The current calibration of the system was intended to match a typical range of absorption and reduced scattering coefficients of skin tissue, and preliminary clinical trials on a set of healthy individuals showed a good consistency except at $\lambda = 660$ nm. At this wavelength the measured tissue data were outside the range of the calibration model in some instances. This problem may be solved by extension of the calibration model range, but the problem may also originate in the fact that the system was calibrated on homogeneous one-layer phantoms, whereas skin tissue is an inhomogeneous multilayer structure. Furthermore, the clinical trials clearly demonstrated that it is imperative to ensure proper and reproducible refractive-index matching and mechanical contact properties to obtain valid results. All things considered, the system and the method we have presented here provide a sound basis for future development of compact and dedicated systems for noninvasive or minimally invasive medical diagnostics and monitoring. Still, further research is required for exploring the applicability for specific biomedical implementations.

References

1. J. Welch, M. J. C. van Gemert, M. W. Star, and B. C. Wilson, "Overview of tissue optics," *Optical-Thermal Response of Laser-Irradiated Tissue*, A. J. Welch and M. J. C. van Gemert, eds. (Plenum, New York, 1995), Chap. 2.

2. J. W. Feather, D. J. Ellis, and G. Leslie, "A portable reflectometer for the rapid quantification of cutaneous haemoglobin and melanin," Phys. Med. Biol. 33, 711–722 (1988).

3. S. L. Jacques, "Reflectance spectroscopy with optical fiber devices, and transcutaneous bilirubinometers," in *Biomedical Optical Instrumentation and Laser-Assisted Biotechnology*, A. M. Verga Scheggi, S. Martellucci, A. N. Chester, and R. Pratesi, eds., Vol. E325 of NATO ASI Series (Kluwer Academic, Dordrecht, The Netherlands, 1996), pp. 83–94.

4. M. A. Franceschini, E. Gratton, and S. Pantini, "Noninvasive optical method of measuring tissue and arterial saturation: an application to absolute pulse oximetry of the brain," Opt. Lett. 24, 829–831 (1999).

5. S. L. Jacques, "Origins of tissue optical properties in the UVA, visible, and NIR regions," in *Advances in Optical Imaging and Photon Migration*, R. R. Alfano and J. G. Fujimoto, eds., Vol. 2 of OSA Topics in Optics and Photonics Series (Optical Society of America, Washington, D.C., 1996), 364–369.

6. A. H. Hielscher, J. R. Mourant, and I. J. Bigio, "Influence of

7. J. R. Mourant, J. P. Freyer, A. H. Hielscher, A. A. Eick, D. Shen, and T. M. Johnson, "Mechanisms of light scattering from biological cells relevant to noninvasive optical-tissue diagnostics," Appl. Opt. 37, 3586–3593 (1998).

8. J. T. Bruulsema, J. E. Hayward, T. J. Farrell, M. S. Patterson, L. Heinemann, M. Berger, T. Koschinsky, C. J. Sandahl, H. Orskov, M. Essenpreis, R. G. Schmelzeisen, and D. Bocker, "Correlation between blood glucose concentration in diabetics and noninvasively measured tissue optical scattering coefficient," Opt. Lett. 22, 190–192 (1997).

9. M. S. Patterson, B. Chance, and B. C. Wilson, "Time resolved reflectance and transmittance for the non-invasive measurement of tissue optical properties," Appl. Opt. 28, 2331–2336 (1989).

10. S. Andersson-Engels, R. Berg, A. Persson, and S. Svanberg, "Multispectral tissue characterization with time-resolved detection of diffusely scattered white light," Opt. Lett. 18, 1697–1699 (1993).

11. B. Chance, M. Cope, E. Gratton, N. Ramanujam, and B. Tromberg, "Phase measurement of light absorption and scatter in human tissue," Rev. Sci. Instrum. 69, 3457–3481 (1998).

12. S. Fantini, M. A. Franceschini, J. S. Maier, S. A. Walker, B. Barbieri, and E. Gratton, "Frequency-domain multichannel optical detector for noninvasive tissue spectroscopy and oximetry," Opt. Eng. 34, 32–42 (1995).

13. T. J. Farrell, M. S. Patterson, and B. Wilson, "A diffusion theory model of spatially resolved, steady-state diffuse reflectance for noninvasive determination of tissue optical properties in vivo," Med. Phys. 19, 879–888 (1992).

14. P. Marquet, F. Bevilacqua, C. Depeursinge, and E. B. DeHaller, "Determination of reduced scattering and absorption coefficients by a single charge-coupled-device array measurement. I. Comparison between experiments and simulations," Opt. Eng. 34, 2055–2063 (1995).

15. A. Kienle, L. Lilge, M. S. Patterson, R. Hibst, R. Steiner, and B. C. Wilson, "Spatially resolved absolute diffuse reflectance measurements for noninvasive determination of the optical scattering and absorption coefficients of biological tissue," Appl. Opt. 35, 2304–2314 (1996).

16. R. Bays, G. Wagnieres, D. Robert, D. Braichotte, J. F. Savary, P. Monnier, and H. van den Bergh, "Clinical determination of tissue optical properties by endoscopic spatially resolved reflectometry," Appl. Opt. 35, 1756–1766 (1996).

17. J. R. Mourant, T. Fuselier, J. Boyer, T. M. Johnson, and I. J. Bigio, "Predictions and measurements of scattering and absorption over broad wavelength ranges in tissue phantoms," Appl. Opt. 36, 949–957 (1997).

18. M. G. Nichols, E. L. Hull, and T. H. Foster, "Design and testing of a white-light, steady-state diffuse reflectance spectrometer for determination of optical properties of highly scattering systems," Appl. Opt. 36, 93–104 (1997).

19. J. S. Dam, P. E. Andersen, T. Dalgaard, and P. E. Fabricius, "Determination of tissue optical properties from diffuse reflectance profiles by multivariate calibration," Appl. Opt. 37, 772–778 (1998).

20. R. M. Doornbos, R. Lang, R. Aalders, F. W. Cross, and H. J. C. M. Sterenborg, "The determination of in vivo human tissue optical properties and absolute chromophore concentrations using spatially resolved steady-state diffuse reflectance spectroscopy," Phys. Med. Biol. 44, 967–981 (1999).

21. T. H. Pham, F. Bevilacqua, T. Spott, J. S. Dam, B. Tromberg, and S. Andersson-Engels, "Quantifying the absorption and reduced scattering coefficients of tissuelike turbid media over a broad spectral range with a noncontact Fourier transform hyperspectral imaging," Appl. Opt. 39, 6487–6497.

22. L. V. Wang, "Source of error in calculation of optical diffuse reflectance from turbid media using diffusion theory," Comput. Methods Program Biomed. 61, 163–170 (2000).

23. L. H. Wang, S. L. Jacques, and L. Q. Zheng, "MCML—Monte Carlo modeling of photon transport in multi-layered tissues," Comput. Methods Program Biomed. 47, 131–146 (1995).

24. T. J. Farrell, B. C. Wilson, and M. S. Patterson, "The use of a neural network to determine tissue optical properties from spatially resolved diffuse reflectance measurements," Phys. Med. Biol. 37, 2281–2286 (1992).

25. H. C. van de Hulst, Multiple Light Scattering (Academic, New York, 1980), Vols. I and II.

26. R. Graff, J. G. Aarnoudse, F. F. M. de MulHcok, and W. Jentink, "Similarity relations for anisotropic scattering in absorbing media," Opt. Eng. 82, 244–252 (1993).

27. J. S. Dam, T. Dalgaard, P. E. Fabricius, and S. Andersson-Engels, "Multiple polynomial regression method for determination of biomedical optical properties from integrating sphere measurements," Appl. Opt. 89, 1202–1209 (2000).

28. W. F. Cheong and A. J. Welch, "A review of the optical properties of biological tissue," IEEE J. Quantum Electron. 26, 2166–2185 (1990).

29. H. J. van Staveren, C. J. M. Moes, J. van Marle, S. A. Prahl, and M. J. C. van Gemert, "Light scattering in Intralipid-10% in the wavelength range of 400–1100 nm," Appl. Opt. 30, 4507–4514 (1991).

30. S. T. Flock, S. L. Jacques, B. C. Wilson, W. M. Star, and M. J. C. van Gemert, "Optical properties of Intralipid: a phantom medium for light propagation studies," Lasers Surg. Med. 12, 510–519 (1992).

31. S. J. Matcher, M. Cope, and D. T. Delpy, "Use of the water absorption spectrum to quantify tissue chromophore concentration changes in near-infrared spectroscopy," Phys. Med. Biol. 39, 177–196 (1994).

32. J. R. Mourant, I. J. Bigio, D. A. Jack, T. M. Johnson, and H. D. Miller, "Measuring absorption coefficients in small volumes of highly scattering media: source-detector separations for which path lengths do not depend on scattering properties," Appl. Opt. 36, 5655–5661 (1997).

33. G. Kumar, "Optimal probe geometry for near-infrared spectroscopy of biological tissue," Appl. Opt. 36, 2286–2293 (1997).

34. C. R. Simpson, M. Kohl, M. Essenpreis, and M. Cope, "Near-infrared optical properties of ex vivo human skin and subcutaneous tissues measured using the Monte Carlo inversion technique," Phys. Med. Biol. 48, 2465–2478 (1998).

35. F. P. Bolin, L. E. Preuss, R. C. Taylor, and R. J. Ference, "Refractive index of some mammalian tissues," Appl. Opt. 28, 2297–2303 (1989).

P.D. 00/12/96
p1977-1986 = ⑩

A multiple wavelength algorithm in color image analysis and its applications in stain decomposition in microscopy images

Ruixia Zhou
Department of Cellular Pathology; Armed Forces Institute of Pathology/American Registry of Pathology, Walter Reed Medical Center, Washington, D.C. 20306-6001

Elizabeth H. Hammond
Department of Pathology, University of Utah, Salt Lake City, Utah 84132

Dennis L. Parker
Department of Radiology and Medical Informatics, University of Utah, Salt Lake City, Utah 84132

Stains have been used in optical microscopy to visualize the distribution and intensity of substances to which they are attached. Quantitative measures of optical density in the microscopic images can in principle be used to determine the amount of the stain. When multiple dyes are used to simultaneously visualize several substances to which they are specifically attached, quantification of each stain cannot be made using any single wavelength because attenuation from the several stain components contributes to the total optical density. Although various dyes used as optical stains are perceived as specific colors, they, in fact, have complex attenuation spectra. In this paper, we present a technique for multiple wavelength image acquisition and spectral decomposition based upon the Lambert–Beer absorption law. This algorithm is implemented based on the different spectral properties of the various stain components. By using images captured at N wavelengths, N components with different colors can be separated. This algorithm is applied to microscopy images of doubly and triply labeled prostate tissue sections. Possible applications are discussed. © *1996 American Association of Physicists in Medicine.*

I. INTRODUCTION

In pathology, human tissue sections are commonly stained biochemically or immunocytochemically in order to use color to enhance the contrast of specific structures in the microscopic images. The distribution of stain provides an indicator of the distribution of the substance or structure to which the stain is specifically attached. The optical density of the stain can then be used to determine the amount of stain. This measurement can be simply obtained through a monochromic image.

In nearly every situation, pathologists desire to simultaneously evaluate a number of substances or structures in a single piece of tissue. There are generally two purposes for the evaluation of multiply stained slides: (1) To evaluate a specific substance in the structure that can only be visually recognized through the second dye. For instance, in order to study the distribution of immunocytochemical PSAP staining in prostate tumor cells, a second nuclear stain is used for recognition of malignant cells. (2) To obtain the relationship of two or more substances or to simultaneously examine the photometric and morphometric parameters of one or more structures. For example, in the study of prostate cancer, the PSAP staining and nuclei shape may provide some diagnostic information.[1] In order to evaluate the percentage of PSAP staining over malignant prostate cytoplasm and the shape of the nuclei, PSAP protein, cytoplasm, and nuclei need to be labeled by three different dyes. In both cases, multiple dyes can be attached to several substances in a single structure or each dye can be attached to a specific structure. Although

these dyes are visualized to have specific colors, they actually have complex attenuation spectra. Therefore, in regions where the stains overlap, the quantification of each stain component cannot be obtained at any single wavelength because the optical density at any single wavelength or a broad range of wavelength is determined by the total attenuation from the multiple stains.

Recent studies have shown that the optical mixtures of several absorbing substances can be analyzed in certain cases. Where the absorption bands of the individual component of the mixture do not overlap, the analysis is simple and straightforward. Wavelengths are selected where each component in turn displays an absorption adequate for measurement and the other components display negligible absorption. Thus one attenuation measurement at each chosen wavelength suffices to determine each individual substance in the mixture. This technique has been successfully used in pathology specimens by Bacus et al.[2-4] The advantages of this technique are that (1) it provides insight into the biochemical composition of the cell or tissue; (2) image acquisition is simply performed by using narrow band filters. Unfortunately, current cytochemistry and histochemistry offer a very limited number of such dyes with nonoverlapping spectra.

During the past few years, the growing interest in color processing has led to the development of spectral decomposition techniques using three channel color video cameras. The color video model uses three broadband filters in red, green, and blue to obtain a color image. Various color space transformation models from RGB have been developed.[5-12]

In the transformed three-dimensional color space, color objects can be distinguished. After a user defines a thresh ld, the image can be segmented. The amount of each stain in objects with similar color can be determined by optical densitometry. This technique allows object discrimination without prior determination of the spectral properties of the stains. Image acquisition is also simply done using a commercially available RGB camera. The RGB technique is based on the human visual system with broad attenuation spectra. However, the spectral basis provided by the RGB detectors will in general be suboptimal for the specific stain combinations. Further, this technique does not permit insights into the biochemical composition. The user defined thresholds may result in some errors in segmentation, which in turn affect the accuracy of quantification. Moreover, spectral information is lost during image acquisition by using broadband filters. Finally, spatial resolution is lower in RGB cameras than in monochromic cameras because three pixels (red, green, and blue) must be interleaved, and the spacing between pixels is increased.

To overcome the drawbacks of the above two techniques, we have developed a new color decomposition technique based upon the differences of mass absorptivity ratios at any two wavelengths. This technique can be used to quantify each stain component in a mixture or the stains in various structures. We start with a general formulation of the multiple wavelength algorithm according to Lambert–Beer law. From this general formulation, dual and triple wavelength algorithms for two and three colors are derived. We describe the modifications that were necessary to implement this spectral decomposition technique on a conventional transmitted light microscope. *An excellent review of the basic hardware and the hardware setup procedures for video microscopy are provided by Inoue.*[15] We also provide the details of specimen preparation that are necessary for accurate measurements. Results of preliminary experiments are presented.

II. THEORY

A. Multiple wavelength algorithm

In this discussion we assume a video microscopy system, where, to first order, the pixel values of the digital image are proportional to the distribution of light intensity incident on the detector: $G(x,y)=kI(x,y)$. In this system, when light of wavelength λ_k passes through N components of concentration $c_i(x,y)$ and thickness $t_i(x,y)$, we have from the Lambert–Beer law,[12,14]

$$G_k(x,y)=G0_k(x,y)\exp\left(-\sum_{i=1}^{N} m_{ik}c_i(x,y)t_i(x,y)\right), \quad (1)$$

where m_{ik} is the mass absorptivity of the ith component obtained at wavelength λ_k. $G_k(x,y)$ and $G0_k(x,y)$ are the images obtained through the N components and in their absence, respectively.

We define A_k to be the absorbance at wavelength λ_k and define the mass density as $\delta_i(x,y)=c_i(x,y)\cdot t_i(x,y)$. A_k can then be written as

$$A_k(x,y)=\ln\left(\frac{G0_k(x,y)}{G_k(x,y)}\right)=\sum_{i=1}^{N} m_{ik}\delta_i(x,y). \quad (2)$$

If N sets of images G_k ($k=1,2,\dots,N$) are acquired at N different wavelengths, $\lambda_1,\lambda_2,\dots,\lambda_k,\dots,\lambda_N$, we obtain the following N linear equations:

$$A_1(x,y)=m_{11}\delta_1(x,y)+m_{21}\delta_2(x,y)+\cdots+m_{N1}\delta_N(x,y),$$

$$A_2(x,y)=m_{12}\delta_1(x,y)+m_{22}\delta_2(x,y)+\cdots+m_{N2}\delta_N(x,y),$$

$$A_N(x,y)=m_{1N}\delta_1(x,y)+m_{2N}\delta_2(x,y)+\cdots$$
$$+m_{NN}\delta_N(x,y). \quad (3)$$

Equation (3) can be written as a matrix equation:

$$A=M\cdot D, \quad (4)$$

where we define

$$A=\begin{bmatrix} A_1 \\ A_2 \\ \cdots \\ A_N \end{bmatrix}, \quad D=\begin{bmatrix} \delta_1 \\ \delta_2 \\ \cdots \\ \delta_N \end{bmatrix},$$

$$M=\begin{bmatrix} m_{11} & m_{21} & \cdots & m_{N1} \\ m_{12} & m_{22} & \cdots & m_{N2} \\ \cdots & \cdots & \cdots & \cdots \\ m_{1N} & m_{2N} & \cdots & m_{NN} \end{bmatrix}.$$

If $|M|\neq 0$, we can solve for δ_i as

$$\delta_1(x,y)=\frac{\Delta_1}{|M|}, \quad \delta_2(x,y)=\frac{\Delta_2}{|M|}\cdots, \quad \delta_N(x,y)=\frac{\Delta_N}{|M|}. \quad (5)$$

where

$$\Delta_1=\begin{bmatrix} A_1 & m_{21} & \cdots & m_{N1} \\ A_2 & m_{22} & \cdots & m_{N2} \\ \cdots & \cdots & \cdots & \cdots \\ A_N & m_{2N} & \cdots & m_{NN} \end{bmatrix},$$

$$\Delta_2=\begin{bmatrix} m_{11} & A_1 & \cdots & m_{N1} \\ m_{12} & A_2 & \cdots & m_{N2} \\ \cdots & \cdots & \cdots & \cdots \\ m_{1N} & A_N & \cdots & m_{NN} \end{bmatrix},$$

and

$$\Delta_N=\begin{bmatrix} m_{11} & m_{21} & \cdots & m_{N-1,1} & A_1 \\ m_{12} & m_{22} & \cdots & m_{N-1,2} & A_2 \\ \cdots & \cdots & \cdots & \cdots & \cdots \\ m_{1N} & m_{2N} & \cdots & m_{N-1,N} & A_N \end{bmatrix}. \quad (6)$$

If the absolute value of the mass absorptivity, m_{ij} ($i,j=1,2,3,\dots,N$) is known for each of N components and at

each of the N wavelengths, then we see from Eq. (5) that the mass density distribution f each of the N components can be determined using the N absorbance images A_k ($k = 1,2,....,N$) obtained at these same wavelengths.

In practice, it is difficult to determine the absolute mass absorptivity of the stain components in tissue. Although accurate measurements of each stain absorptivity spectrum could be made in solution, the stain absorption spectra is different in tissue than it is in solution. Thus, accurate measurements of the absorption spectra would be required in the tissue. In our current methods, we do not have an independent measurement of stain concentration in tissue. We have, therefore, chosen to measure the shape of the attenuation spectra for each stain in tissue, and then solve only for the relative mass density distribution of each stain. To begin, we write Eq. (2) in the form

$$A_k(x,y) = \sum_{i=1}^{N} \frac{m_{ik}}{m_{NK}} m_{Ni} \delta_i(x,y). \tag{7}$$

Equation (4) is then written as the matrix equation

$$A = R \cdot D'. \tag{8}$$

where

$$R = \begin{bmatrix} \dfrac{m_{11}}{m_{1N}} & \dfrac{m_{21}}{m_{2N}} & \cdots & \dfrac{m_{N1}}{m_{NN}} \\ \dfrac{m_{12}}{m_{1N}} & \dfrac{m_{22}}{m_{2N}} & \cdots & \dfrac{m_{N2}}{m_{NN}} \\ \cdots & \cdots & \cdots & \cdots \\ \dfrac{m_{1N}}{m_{1N}} & \dfrac{m_{2N}}{m_{2N}} & \cdots & \dfrac{m_{NN}}{m_{NN}} \end{bmatrix}$$

$$= \begin{bmatrix} r_{11} & r_{21} & \cdots & r_{N1} \\ r_{12} & r_{22} & \cdots & r_{N2} \\ \cdots & \cdots & \cdots & \cdots \\ 1,N-1 & r_{2,N-1} & \cdots & r_{N,N-1} \\ 1 & 1 & \cdots & 1 \end{bmatrix} \tag{9}$$

and

$$D' = \begin{bmatrix} m_{1N}\delta_1 \\ m_{2N}\delta_2 \\ \cdot \\ m_{NN}\delta_N \end{bmatrix}. \tag{10}$$

The matrix R contains the wavelength-dependent mass absorptivity ratios f each component. Equation (8) can be solved for the N mass densities as

$$\delta_1 = \frac{\Pi_1}{m_{1N}|R|}, \quad \delta_2 = \frac{\Pi_2}{m_{2N}|R|}, ..., \quad \delta_N = \frac{\Pi_N}{m_{NN}|R|}, \tag{11}$$

where we define

$$\Pi_1 = \begin{bmatrix} A_1 & r_{21} & \cdots & r_{N1} \\ A_2 & r_{22} & \cdots & r_{N2} \\ \cdots & \cdots & \cdots & \cdots \\ A_{N-1} & r_{2,N-1} & \cdots & r_{N,N-1} \\ A_N & 1 & \cdots & 1 \end{bmatrix},$$

$$\Pi_2 = \begin{bmatrix} r_{11} & A_1 & \cdots & r_{N1} \\ r_{12} & A_2 & \cdots & r_{N2} \\ \cdot & \cdots & \cdots & \cdots \\ r_{1,N-1} & A_{N-1} & \cdots & r_{N,N-1} \\ 1 & A_N & \cdots & 1 \end{bmatrix},$$

and

$$\Pi_N = \begin{bmatrix} r_{11} & r_{21} & \cdots & r_{N-1,1} & A_1 \\ r_{12} & r_{22} & \cdots & r_{N-1,2} & A_2 \\ \cdots & \cdots & \cdots & \cdots & \cdots \\ r_{1,N-1} & r_{2,N-1} & \cdots & r_{N-1,N-1} & A_{N-1} \\ 1 & 1 & \cdots & 1 & A_N \end{bmatrix}. \tag{12}$$

Equation (11) demonstrates that the different stain components in the image can be separated based upon the mass absorptivity ratios of each component. When the absolute mass absorptivities are unknown, we can select a wavelength for which all of the mass absorptivity coefficients are nonzero and use that as the Nth wavelength in Eq. (9). Then relative δ values can be obtained according to Eq. (11). Therefore, a mixture containing N components can be decomposed at N wavelengths with $N(N-1)$ mass absorptivity ratios.

B. Two-wavelength algorithm

Consider a mixture containing two stain components, δ_1 and δ_2. At two chosen wavelengths, λ_a and λ_b, the wavelength-dependent mass absorptivity ratios of these two components are $\alpha = r_{11}$ and $\beta = r_{21}$, respectively. The absorbances at the two wavelengths are A and B respectively. Then we can solve for δ_1 and δ_2 as

$$\delta_1(x,y) = \frac{A(x,y) - \beta \cdot B(x,y)}{m_{1b} \cdot (\alpha - \beta)}.$$

$$\delta_2(x,y) = \frac{\alpha \cdot B(x,y) - A(x,y)}{m_{2b} \cdot (\alpha - \beta)}. \tag{13}$$

C. Three-wavelength algorithm

Similarly, consider an image that contains three components, δ_1, δ_2, and δ_3. At three wavelength, λ_a, λ_b, and λ_c, the wavelength-dependent mass absorptivity ratios of the first component are $\alpha_1 = r_{11}$ and $\alpha_2 = r_{12}$, those of the second component are $\beta_1 = r_{21}$ and $\beta_2 = r_{22}$, and those of the third component are $\gamma = r_{31}$ and $\gamma_2 = r_{32}$ respectively. The absorbances at the three wavelengths are A, B, and C, respectively. The three components can be determined as

$$\delta_1(x,y)$$

$$= \frac{A(\beta_2-\gamma_2)+B(\gamma_1-\beta_1)+C(\beta_1\gamma_2-\beta_2\gamma_1)}{m_{1e}\cdot[\alpha_1\beta_2-\alpha_2\beta_1+\alpha_2\gamma_1-\alpha_1\gamma_2+\beta_1\gamma_2-\gamma_1\beta_2]},$$

$$\delta_2(x,y)$$

$$= \frac{A(\gamma_2-\alpha_2)+B(\alpha_1-\gamma_1)+C(\alpha_2\gamma_1-\alpha_1\gamma_2)}{m_{2e}\cdot[\alpha_1\beta_2-\alpha_2\beta_1+\alpha_2\gamma_1-\alpha_1\gamma_2+\beta_1\gamma_2-\gamma_1\beta_2]},$$

$$\delta_3(x,y)$$

$$= \frac{A(\alpha_2-\beta_2)+B(\beta_1-\alpha_1)+C(\alpha_1\beta_2-\alpha_2\beta_1)}{m_{3e}\cdot[\alpha_1\beta_2-\alpha_2\beta_1+\alpha_2\gamma_1-\alpha_1\gamma_2+\beta_1\gamma_2-\gamma_1\beta_2]}.$$

(14)

In practice, the doubly labeled tissue sections have three attenuation components: tissue itself and two stains. We assume that the tissue section itself appears translucent and has no color. We approximate the tissue attenuation at any wavelength as Δ. In this case, we can replace the A and B in Eq. (11) by $A'=A-\Delta$ and $B'=B-\Delta$. Similarly, the A, B, and C in Eq. (14) can be replaced by $A'=A-\Delta$ and $B'=B-\Delta$, and $C'=C-\Delta$, respectively.

III. METHODS

A. Microscope hardware

In order to implement the multiple wavelength decomposition algorithm, a microscope image analysis system was configured using a transmitted light OLYMPUS BH-2 microscope which is interfaced to a PC 486 DX 33 MHz computer with 16 Mbyte of ram and 500 Mbyte disk and an SVG monitor. The necessary microscope functions, including translation stage positioning, light illumination, and filter selection, are interfaced to the PC 486 computer using a MAC-2000 microscope controller and the PC RS232 serial port. The traditional microscope stage was replaced by a step motorized x/y stage. The resolution, reproducibility, and accuracy of the stage are 0.1, 4, and 3 μ respectively. Maximum stage movement speed is 30 000 μ/s. The focus was also controlled with a z axis stepper motor, with resolution of 0.01 μ and movement speed of 27 000 μ/s. The filter wheel, with positions for six filters, was also motorized for computer control. The light intensity was either manually, or by computer control of a DC stabilized power source.

An OLYMPUS achromatic objective, model Apo 20X, and a photo eyepiece with x5 magnification, giving a total magnification of x100, were used in image acquisition of all the image demonstrated in this paper. A XILLIX 1400 monochromatic CCD camera (XILLIX Technologies Corp., Vancouver, British Columbia, Canada) (1280×1024×10 bit) was attached to the microscope photo tube and used as the detector. For our system, with a total magnification of x100 and the image matrix of 1280×1024, we obtained pixel dimensions of 0.22 μ by 0.22 μ. Image acquisition was under computer control. The sensitivity of the camera is approximately 10^{-4}–100 lux (compared to the traditional 3–2000 lux). The acquired images were not subjected to any pro-
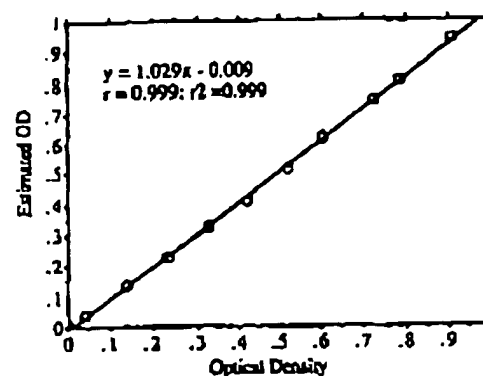
FIG. 1. The linear correlation between measured optical densities and calibrated standards. The correlation is indicated by the slope 1.029, intercept minus 0.009, and correlation coefficient 0.999.

cessing algorithms other than the specific image decomposition algorithms outlined in the theory section.

Before the acquisition of any images, the light path was adjusted for Koehler illumination, as described by Inoue.[15] The illumination was found to vary by about 1% over the imaged field of view. Any deviation in illumination uniformity or variation in sensitivity as a function of wavelength is compensated by the normalization procedure of the measurement technique described in Sec. II. Although the microscope MTF was not measured, the performance of the entire system was judged to be quite adequate by an experienced pathologist. Tissue structures were observed with sharpness although the magnification and the resulting pixel dimensions are at the diffraction limit. For the study of this paper, the stains covered large regions, with moderately slow spatial variation and the measurements were primarily in the low spatial frequency portion of the system MTF. We refer the reader to the text by Inoue[15] for technical details pertaining to the hardware setup necessary for accurate quantitative measurements of stain intensity.

The system linearity was measured using a stepped neutral density filter of known optical densities. The stepped filter had ten strips with gradually increasing density from zero to one and the densities were independently measured with an optical densitometer. For measurements, the zero optical density was used as the reference intensity. The results are shown in Fig. 1. The relationship between the measured and known optical density was $OD_{measured}=1.03\, OD_{true}-0.009$ with a correlation coefficient of $r^2=0.999$.

Two interference filters centered at 480 (λ_a) and 570 nm (λ_b) with 10 nm bandwidths were used to acquire the images for the dual wavelength algorithm. Three interference filters centered at 480 (λ_a), 570 (λ_b), and 630 nm (λ_c) with 10 nm bandwidths were used to acquire the images for the triple wavelength algorithm. These filters are manually switched on the filter mount in the base of microscope. The wavelengths were chosen to provide a difference in the mass absorptivity ratios at any two wavelengths among stain components. At these wavelengths, we found chromatic aberration to be insignificant. Any image shifts due to filter misalignments were measured and corrected using an alignment grid.

A small wavelength-dependent focus adjustment was also necessary for the 630 nm filter but was not required for the other filters. Image magnification was the same for all wavelengths used.

B. Sample preparation

All the prostate tissue sections were cut with a thickness of 4 μ. A two stain test sample was created by double staining a prostate tissue section with PSAP-DAB (brown stain) and hematoxylin (blue stain). In this sample, the cytoplasm was strongly stained by brown color and nuclei were strongly stained by blue color. To test the efficiency of the triple-wavelength color segmentation, a second prostate tissue section was triply labeled by the PSAP-DAB (brown stain), hematoxylin (blue stain), and Keratin-FastRed (pink stain). In this case, the cytoplasm is partially stained with brown DAB and completely stained with pink while the nuclei are stained with blue. Each stain will slightly precipitate in the connective tissue surrounding the prostate glands. This partial precipitation occurs throughout the sample and we refer to this weak stain in the connective tissue as the background. In order to estimate the wavelength-dependent absorptivity ratio of each stain component and the attenuation of nonstained tissue, four sets of control tissue sections were stained by (1) PSAP-DAB (brown) only, (2) hematoxylin (blue) only, (3) Keratin-FastRed (pink) only, and (4) none of these stains. In each case, the control samples were processed in the same solutions as the multiple stain test samples. A detailed description of sample preparation and control slide preparation is for a set of two-wavelength experiments has been published previously.[16,17] The preparation technique for the three-wavelength experiments is a logical extension of these techniques.

C. Estimation of relative mass absorptivities

The tissue section background values are obtained from measurements on corresponding regions in the nonstained tissue section at each wavelength. After correction for this wavelength-dependent background, the relative mass absorptivities are estimated by making optical density measurements in regions of stain uptake on the singly stained slides. For the PAP-DAB and FastRed stains, regions are drawn that include only cytoplasm (no nuclei) within the gland area. For the Hematoxylin stain, regions are drawn to only include the stained nuclei. To obtain an estimate of the precision of the measurement, multiple regions are measured. We report the standard deviation of the absorptivity ratios.

Although not necessary for these experiments, the full spectra of the three stains used in this paper were measured using the singly labeled tissue sections from one control batch. The measurements were made using a ZEISS microphotometer 400 and the results are shown in Fig. 2. Because of the spatial resolution of this system, the measurements did not exclude regions of nonstain uptake, and these curves are only approximations to actual stain spectra that would be required in this study.
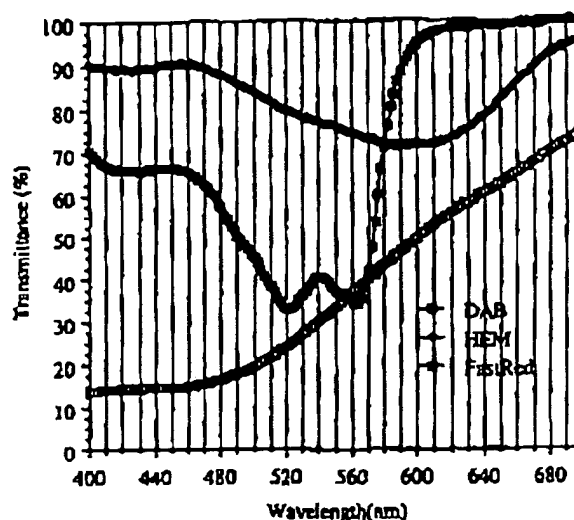

FIG. 2. A spectral transmittance plot of PAP-DAB, hematoxylin and Keratin-FastRed stain products in prostate tissue sections. The data are obtained from ZEISS microphotometer 400.

D. Test of system accuracy

Although it is difficult to obtain independent measurements of the amount of stain in a tissue section, we configured a set of experiments where the same set of regions on a slide were imaged during the various stages of staining by the multiple components. By carefully repositioning the slide using our computer controlled x/y stage we were able to get very accurately placed sets of multiple images at the same tissue locations. By measuring the optical density in essentially identical regions after each stain component was added, the differential optical density at each location was obtained. This differential optical density was used as the measurement standard for the corresponding stain. At the same time (in the same batch), singly labeled control slides were prepared for each stain used in the procedure. These were also imaged at the various preparation stages to ensure that the subsequent staining procedures did not modify stain density. The control slides were then used, as outlined above, to obtain the relative absorptivities of each component at the imaged wavelengths and these were then used to segment the multiply labeled slides, again as described above. The measurements obtained from the multiple wavelength segmentation were then compared with those obtained from the direct measurements at the same locations.

IV. RESULTS

The assumption that the tissue section itself has no color has been validated in an earlier study,[16] where the absor-

TABLE I. Absorptivity ratios, dual wavelength.

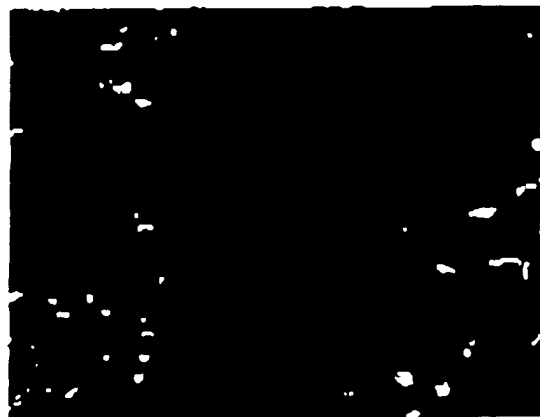| Stain	Absorptivity ratio $m_s(480)/m_s(570)$	Standard deviation
PAP-DAB	$\alpha = 1.71$	0.039
HEM	$\beta = 0.51$	0.007

(a)

(b)

(c)

(d)

(e)

FIG. 3. (a) Photomicrograph of the imaging field on the prostate tissue slide that is stained with PAP-DAB (brown) and Hematoxylin (blue) (magnification= ×100). Image intensity is inversely proportional to the absorption of hematoxylin and PAP stain. (b) The image of (a) captured at wavelength 480 nm. (c) The image of (a) captured at 570 nm. (d) The brown component (100×δ) image of (a). Image intensity is proportional to the absorption of the PAP stain. (e) The blue component (100×δ) image of (a).

bance of a 4 μ thick section without any stains was found to be approximately 0.010, 0.011, and 0.009 at 480, 570, and 630 nm. respectively. Any errors in this estimate contribute only small errors in our measurements. Therefore, $A' = A - 0.010$. $B' = B - 0.011$, and $C' = C - 0.009$ are used in Eqs. (13) and (14) instead of A, B. and C. Because the absolute mass absorptivity is not known, relative δ values were obtained by assuming that the m_{1b} and m_{2b} are equal to 1 in Eq. (13) and m_{1r} and m_{2c} and m_{3c} are equal to 1 in Eq. (14).

From the singly labeled tissue sections, we obtained an estimate of α equal to 1.71 for the brown only slide and β equal to 0.51 for the blue only slide (see Table I). Images of a prostatic carcinoma slide stained with PAP-DAB (brown) and hematoxylin (blue) are shown in Fig. 3(a) was obtained with white light. Images captured at wavelength 480 and 570 nm are shown in Fig. 3(b) and Fig. 3(c), respectively. From these images, we can see that the absorption spectra of the two components overlap at the wavelengths used. It is difficult to separate them adequately in these monochromic im-

TABLE II. Absorptivity ratios, triple wavelength.

Stains	Absorptivity ratio SD $m_i(480)/m_i(630)$	Absorptivity ratio SD $m_i(570)/m_i(630)$
PAP-DAB	$\alpha_1 = 2.44$, 0.049	$\alpha_2 = 1.42$, 0.021
HEM	$\beta_1 = 0.67$, 0.002	$\beta_2 = 1.37$, 0.032
FastRed	$\gamma_1 = 4.03$, 0.052	$\gamma_2 = 6.39$, 0.091

ages. After applying the dual wavelength method with the absorptivity ratios of α equal to 1.71 and β equal to 0.51, we obtained the brown and blue stain component images shown in Figs. 3(d) and 3(e). The image intensities in Figs. 3(d) and 3(e) are proportional to the mass per unit area of stain material on the slide so that image intensities of these figures are inverted compared to the image intensities in Fig. 3(a), Fig. 3(b), and Fig. 3(c). It is obvious that the blue stain is localized in the nuclei and the brown stain is in the cytoplasm and they are completely separated.

From the singly labeled tissue sections, estimates of $\alpha_1 = 2.44$ and $\alpha_2 = 1.42$ for the brown stain and $\beta_1 = 0.67$ and $\beta_2 = 1.37$ for the blue stain and $\gamma_1 = 4.03$ and $\gamma_2 = 6.39$ for the pink stain were obtained (see Table II). Similarly, the images of the tissue stained with PSAP-DAB (brown), hematoxylin (blue), and Keratin-FastRed (pink) are displayed in Fig. 4. Figures 4(a)–4(d) are images of the same field captured at white light, 480, 570, and 630 nm, respectively. Again, it is difficult to separate the three components by using a conventional histogram threshold method because the absorption of these stain components overlap. Applying the triple wavelength algorithm by using the ratios listed above, we obtain the three component images as shown in Figs. 4(e)–4(g). In these images, the stains are segmented completely. The brown stain is only found in cytoplasmic area, the blue stain is only on the nuclei, and the pink stain is only in the cytoplasmic area.

The system accuracy results are plotted in Figs. 5 and 6 for the dual and triple wavelength algorithms, respectively.

V. DISCUSSION

We have presented a multiple wavelength image decomposition algorithm, which can be used to obtain relative distributions of multiple components with different attenuation spectra. This method allows the segmentation of tissue structures marked by different dyes or the decomposition of stain components in a mixture when these dyes have overlapping spectral absorption properties. Two wavelengths and two mass absorptivity ratios are required to separate two stain components while three wavelengths and six ratios are required to separate three stain components. In general, N measures at N wavelengths and knowledge of $N(N-1)$ mass absorptivity ratios are required in the decomposition of an image containing N components.

The mass absorptivity ratios at any two wavelengths can be simply estimated from attenuation measurements on singly labeled tissue sections. To eliminate any errors that might occur from variations in processing, these singly labeled tissue sections should be prepared as controls and be processed in the same batch in which the multiply labeled specimens are prepared. In this way, errors due to the staining variations from one batch to another or from one tissue type to another can be greatly reduced.

The multiple wavelength decomposition method should be useful in a wide variety of applications, where components with different attenuation spectra need to be separated for distribution determinations and quantitative analysis. The method overcomes the drawbacks of exclusive filtering techniques.[1-4] Compared with RGB color segmentation methods, our multiple wavelength method may facilitate the determination of insights into the biochemical composition in the tissue. Most important, it leads to the accurate quantitation of the relative distribution of each stain component. The use of narrow band filters limits the loss of spectral information in the image acquisition process. In theory, the use of the narrow band filters and the use of optimally selected wavelengths should reduce the random error in the distribution measurements.

Figures 5 and 6 give a good indication of the accuracy and reproducibility of the measurements made using this decomposition technique. Although the "true" measurements are made using the microscopy system, they are obtained directly for each of the sample points plotted. The estimated values are obtained using the absorptivity ratios measured on the control slides to decompose the values on the multiply stained slide. In each case the test shows excellent correlation between the two types of measurements. These results are consistent with reproducibility measurements made previously using the dual wavelength method.[26]

Variations in section thickness as well as variations in the staining, tissue fixation, and processing can occur for different sample preparation batches. The effect of these variations can be significantly reduced by measuring the mass absorptivity using internal controls for each of the study slides. For example, the variations of the color due to the physical and chemical conditions in the staining process can be eliminated by determining the relative wavelength absorption coefficients using the singly labeled sections that are processed along with each staining procedure. Our preliminary study (unpublished observation) shows that the color of the stain components changes very little (coefficient of variation <0.05) from batch to batch. After extended periods of storage, a bleaching effect can occur, causing the tissue stains to fade. This effect was not observed over the short time period of this study.

In another study, we have successfully applied this multiple wavelength technique in the quantification of PSAP staining in doubly labeled prostate tissue sections.[27] In this study, the quantifications of PSAP (either intensity and extent over prostate gland cytoplasm) were used to test the hypothesis that the amount of PSAP in prostate cancer correlates to the patient survival. Normal glands that were positively stained with PSAP were used as an internal control for each of the multiply labeled tissue slides. The PSAP activity of the prostate tumor was evaluated by the ratio of PSAP intensity (or extend) in malignant glands versus PSAP inten-
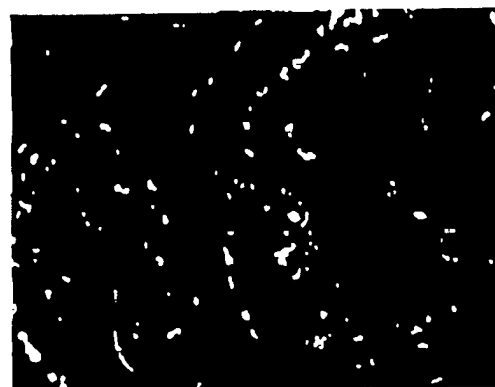
(a)

(e)

(b)

(f)

(c)

(g)

(d)

FIG. 4. (a) Photomicrograph of the imaging field on the prostate tissue slide that is stained with PAP-DAB (brown), Hematoxylin (blue), and Keratin-FastRed (Pink) (magnification=×100). Image intensity is inversely proportional to the absorption of hematoxylin and PAP stain. (b) The image of (a) captured at wavelength 480 nm. (c) The image of (a) captured at wavelength 570 nm. (d) The image of (a) captured at wavelength 630 nm. (c) The brown component (100×δ) image of (a). Image Intensity is proportional to the absorption of the PAP stain. (f) The blue component (100×δ) image of (a). (g) The pink component (100×δ) image of (a).
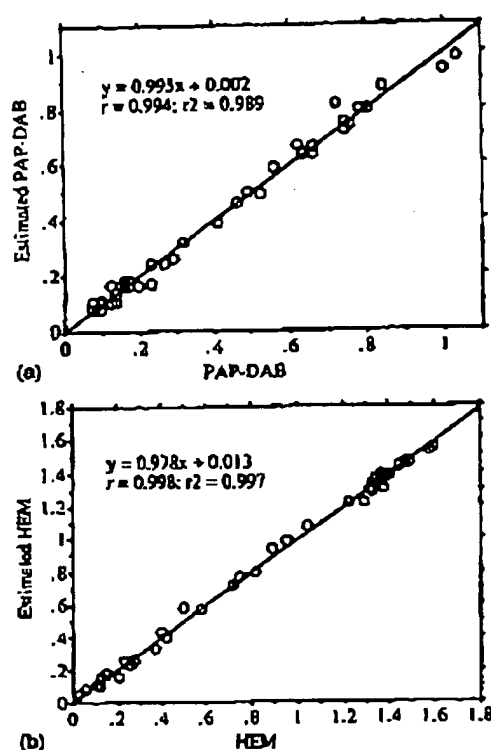
FIG. 5. Accuracy of dual wavelength decomposition: System measurement (43 samples) versus standards. (a) The estimated amount of the PAP-DAB stain. Here $r=0.994$ with slope 0.995 and intercept 0.002. (b) The estimated amount of hematoxylin stain. Here $r=0.998$ with slope 0.978 and intercept 0.013.
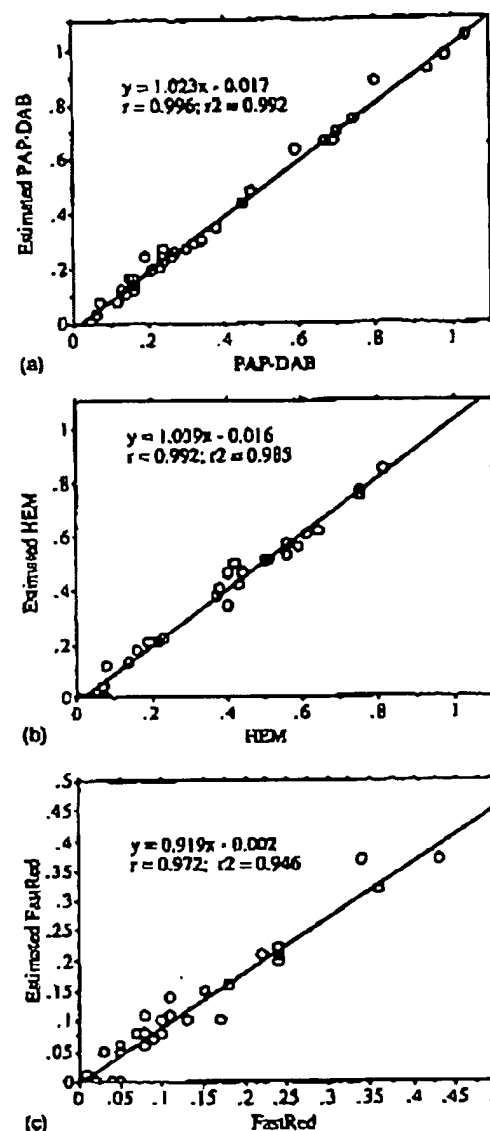

FIG. 6. Accuracy of triple wavelength decomposition. System measurements on 31 samples versus standards. (a) The estimated amount of PAP-DAB stain. Here $r=0.996$ with slope 1.023 and intercept -0.017. (b) The estimated amount of hematoxylin stain. Here $r=0.992$ with slope 1.039 and intercept -0.016. (c) The estimated amount of FastRed stain. Here $r=0.972$ with slope 0.919 and intercept -0.002.

sity (or extent) in normal glands presented in the same slide. We found significant correlation between the PSAP intensity and extent indices and patient survival.[27] We are continuing to study this correlation in a larger group of patients using the same technique. If our study in the large population confirms this hypothesis. it is likely that the multiple wavelength alg rithm may offer a new means for quantitatively evaluating and specifying the treatment for patients with prostate cancer.

The developed multiple wavelength algorithm is indeed worthwhile in quantitative histology and cytology since many prognostically and diagnostically important substances in the tissue are commonly studied by labeling them with multiple stains. Numerous studies have addressed the quantitative immunohistochemical analysis of proteins or other antigens.[1,18-25] We believe that this technique will be useful in the quantitative analysis of a variety of biological materials in multiply stained tissue sections for which the stain absorptivity spectra overlap. The technique permits decomposition and quantification of multiple stain components in a mixture and opens a new way to perform functional studies in various fields where the Lambert–Beer absorption law h lds. The Lambert–Beer absorption law is generally valid except in some cases. such as when chemical interaction between the stain components occurs.[12-14] In this case, the proposed algorithm would need to be modified after the spectral

properties of the post-interaction stain components are known.

Image acquisition for the multiple wavelength technique is labor and time consuming, especially when the number of stain components is large. In order to solve this problem. an automatic microscopic imaging system has been established in our laboratory by utilizing a computer controlled stage, a filter wheel, and a power supply for controlling the illuminating light. By using this system, the user defined region of interest in a slide can be automatically scanned. The efficiency of the multiple wavelength image acquisition has been impr ved by this updated system.

Finally, this study has been performed without the ability

to obtain the absolute spectral absorption curve of the stain components. With only a knowledge of the relative absorption spectra. only relative measures were made. Thus. the main goal of this paper has been to demonstrate the multiple wavelength algorithm in multiple stain segmentation when only absorptivity ratios of the stain components are required. The wavelengths utilized in this study were chosen to give good separation of the stains which that used in our experiment. After making accurate measurements of the complete attenuation spectra. it would be possible to select wavelengths that would give better separation. Instead. we have limited our study to wavelengths in a range that seemed to give minimal image distortions due to wavelength-dependent imaging effects.

ACKNOWLEDGMENTS

[1]M. E. Hammond. T. W. Sause. L. K. Martz. and V. M. Pilepich. "Correlation of prostate-specific acid phosphatase and prostate-specific antigen immunocytochemistry with survival in prostate carcinoma." Cancer 63. 461 (1989).

[2]S. Bacus. J. L. Flowers. M. F. Press. and J. W. Bacus. "The evaluation of estrogen receptor in primary breast carcinoma by computer-assisted image analysis." Am. J. Clin. Pathol. 90. 233–239 (1988).

[3]B. R. Schwartz. G. Pinkus. S. Bacus. M. Toder. and D. S. Weinberg. "Cell proliferation in non-Hodgkin's lymphomas." Am. J. Pathol. 134. 327 (1989).

[4]S. S. Bacus. R. Goldschmidt. D. Chin. G. Moran. D. S. Weinberg. and J. W. Bacus. "Biological grading of breast cancer using antibodies to proliferating cells and other markers." Am. J. Pathol. 135. 783–792 (1989).

[5]G. S. Wasserman. Color Vision: A Historical Introduction (Wiley. New York. 1978).

[6]J. Y. Mary and J. P. Rigaut. Quantitative Image Analysis In Cancer Cytology and Histology (Elsevier. Amsterdam. 1986). pp 19–31.

[7]J. M. Chassery and C. Garbay. "An interactive segmentation method based on a contextual color and shape criterion." IEEE Trans. Pattern Anal. Machine Int. 6. 794 (1984).

[8]S. E. Umbaugh. R. H. Moss. and W. V. Stoecker. "An automatic color segmentation algorithm with application to identification of skin tumor borders." Comput. Med. Imag. Graph. 16. 227–235 (1992).

[9]C. MacAulay. H. Tezcan. and B. Palcic. "Adaptive color basis transformation: An aid in image segmentation." Anal. Quant. Cytol. Histol. 11. 53–58 (1989).

[10]S. Bacus. "A whitening transformation for two-color blood cell images." Pattern Recog. 8. 53–60 (1976).

[11]C. Charpin. J. Jacqueminer. L. Andrac. H. Vacheret. M. C. Gabib. B. Devictor. M. N. Lavau. and M. Toga. "Multiparametric analysis

(SAMBA 200) of the progesterone receptor immunocytochemical assay in nonmalignant and malignant breast disorders." Am. J. Pathol. 133. 199–211 (1989).

[12]G. Brugal. "Colour processing in automated image analysis for cytology." In Quantitative Image Analysis in Cancer Cytology and Histology. edited by J. Y. Mary and J. P. Rigaut (Elsevier. Amsterdam. 1986). pp. 19–30.

[13]H. Piller. Microscope Photometry (Springer-Verlag. Berlin. 1977). pp. 132–135.

[14]G. L. Wied. Optics: A Short Course For Engineers & Scientists (Wiley-Interscience. New York. 1972). pp. 35–38.

[15]S. Inoue. Video Microscopy (Plenum. New York. 1986).

[16]R. Zhou. D. L. Parker. and E. H. Hammond. "Quantitative peroxidase-antiperoxidase complex-substrate mass determination in tissue sections by a dual wavelength method." Ann. Quant. Cytol. Histol. 14. 73–80 (1992).

[17]R. Zhou. "Quantitative evaluation of the peroxidase-antiperoxidase-diaminobenzindine stain in double stained prostatic tumor slides by dual wavelength technique." M.S. thesis. University of Utah. 1992.

[18]R. J. Skelarew. S. C. Bodmer. and L. P. Periscfuk. "Quantitative imaging of the immunocytochemical (PAP) estrogen receptor staining pattern in breast cancer sections." Cytometry 11. 359–378 (1990).

[19]L. Kitayama. A. M. Janson. K. Huxe. L. F. Agnati. A. Cintra. S. O. Ogren. A. Harfstrand. and P. Encroth. "Effect of acute and chronic treatment with imipramine on 5-hydroxytryptamine nerve cell groups and on bulbospinal 5-hydroxytryptamine/substance P/thyrotropin releasing hormone immunoreactive neurons in the rat. A morphometric and microdensitometric analysis." J. Neural Transmission 70. 231–285 (1987).

[20]C. Charpin. "Estrogen receptor immunocytochemical assay (ER-ICA): Computerized image analysis system. immunoelectron microscopy and comparisons with estradiol assays in 115 breast carcinomas." Cancer Res. 46. 4271s–4277s (1986).

[21]C. Charpin. L. Andrac. M. C. Habib. H. Vacheret. L. Xerri. B. Devictor. and M. N. Lavau. "Immunodetection in fine-needle aspirates and multiparametric (SAMBA) image analysis." Cancer Res. 63. 863–872 (1989).

[22]C. Charpin. P. M. Martin. B. Devictor. M. N. Lavau. and M. C. Habib. "Multiparameter study of estrogen receptor immunocytochemical assay in 400 human breast carcinomas: Analysis of estrogen receptor distribution heterogeneity in tissue and correlation with dextran coated charcoal assays and morphological data." Cancer Res. 48. 1578–1586 (1988).

[23]P. H. Nibbering. P. C. J. Leijh. and R. van Furth. "A cytophotometric method to quantitate the binding of monoclonal antibody to individual cells." J. Histochem. Cytochem. 33. 453–462 (1985).

[24]J. Rahier. M. Stevens. Y. Meuten. and J. C. Hengqin. "Determination of antigen concentration in tissue sections by immunodensitometry. Laboratory investigation." 61. 357–363 (1989).

[25]D. S. Gross and J. M. Rothfeld. "Quantitative immunocytochemistry of hypothalamic and pituitary hormones." J. Histochem. Cytochem. 33. 11–20 (1985).

[26]R. Zhou. E. H. Hammond. W. T. Sause. P. Rubin. B. Emami. M. V. Pilepich. S. D. Asbell. and D. L. Parker. "Quantitation of prostate-specific acid phosphatase in prostate cancer: Reproducibility and correlation with subjective grade." Mod. Pathol. 7. 440–448 (1994).

[27]R. Zhou. W. Sause. E. Hammond. and D. Parker. "Correlation of survival with quantitative tissue staining of prostate specific acid phosphatase in patients with prostate carcinoma by using microscopic image analysis: A preliminary report of correlative studies on RTOG protocols 75-06. 77-06. and 83-07." Int. J. Radiat. Oncol. Biol. Phys. 33. 823–829 (1995).
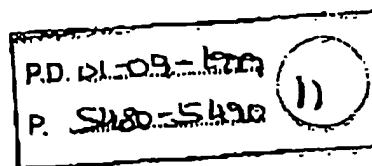
D1

XP-002241596

Spectroscopic diffuse optical tomography for the quantitative assessment of hemoglobin concentration and oxygen saturation in breast tissue

Troy O. McBride, Brian W. Pogue, Ellen D. Gerety, Steven B. Poplack,
Ulf L. Österberg, and Keith D. Paulsen

.. Near-infrared (NIR) spectroscopic diffuse tomography has been used to map the hemoglobin conct tion and the hemoglobin oxygen saturation quantitatively in tissuelike phantoms and to deter average values in vivo. A series of phantom calibrations were performed to achieve quantita accurate images of the absorption and the reduced scattering coefficients at multiple optical wavelen A least-squares fit was applied to absorption-coefficient images at multiple NIR wavelengths to c hemoglobin images of the concentration and the hemoglobin oxygen saturation. Objects of va hemoglobin concentration and oxygen saturation within highly scattering media were localizec imaged to within 15% of their actual values. The average hemoglobin concentration and oxygen ration of breast tissue was measured in vivo for two women volunteers. The potential application f diagnosis of breast tumors is discussed. © 1999 Optical Society of America

OCIS codes: 170.6270, 110.3080, 170.3880, 170.6510, 170.6960, 170.3830.

1. Introduction

Recent studies have suggested that diffuse optical signals measured over the near-infrared (NIR) spectral range may provide sufficient information for the noninvasive mapping of hemoglobin concentration and oxygen saturation in biological tissues.[1-6] One driving force behind the development of NIR spectroscopy and imaging has been the observed local increase in angiogenesis, hence in blood volume, within cancerous tumors that corresponds to a local increase in the hemoglobin concentration, which has been estimated to exist at 4-times contrast with normal tissue.[2,9,7] Breast malignancies have been shown to have a lower median oxygen pressure than the healthy breast.[6,9] Some studies have pointed to a link between the oxygenation level in cancerous tumors and tumor characteristics.[10-12] For exam-

ple, Brizel et al.[10] found tumor oxygenation leve be related to the likelihood of metastases, whe studies by Okunieff et al.[11] and Hoeckel et showed a low-oxygenation status of tumors to b indicator of the effectiveness of radiation ther. In light of these findings it appears that noninva quantitative hemoglobin-concentration and oxy saturation measurements have the potential to vide beneficial information for diagnostic therapeutic decisionmaking. Hence the realiza of NIR spectroscopic diffuse optical tomography fers an opportunity to obtain this information only noninvasively but also spatially resolved an modest cost.

In the diagnostic setting the ultimate goal of s an imaging modality would be to detect and diagr tissue pathologies on the basis of the spatially solved spectroscopic recovery of the optical abs tion properties of tissue. These properties car mapped into physiological parameter distributi of interest, such as hemoglobin concentration oxygen saturation. Success in the spectrosc dimension has been demonstrated in terms point measures of bulk-tissue response, leading single numerical indicators of functional tie characteristics.[1-6] Likewise, considerable effort been devoted to spatially resolving optical proper at a single wavelength by use of diffuse optical in

ing techniques.[13-15] However, ther have been very few attempts to combine spectroscopic data with an imaging method to produce spatially resolved images of the functional parameters that can be derived from measured spectra.

Although optical images have been formed from diffusing light at multiple wavelengths *in vivo*,[3] existing methods are unable to recover quantitative images of hemoglobin-related functional parameters. In breast tissue the primary absorbers are presumed to be oxygenated and deoxygenated hemoglobin, lipids, and water,[16-18] which have significantly different absorption spectra in the near infrared. Quantitatively mapping the absorption coefficient within breast tissue allows the contribution from each component to be approximated, and, in principle, images of the spatial distribution of all major chromophore concentrations can be obtained. This requires that data be recorded from a sufficient number of wavelengths and processed by an appropriate image-reconstruction scheme to recover quantitative absorption-coefficient distributions. Previous research has suggested that quantitative optical-property reconstruction demands that the nonlinear relation between the optical-property distribution and the measured optical response be preserved.[19,20] To date, such techniques have not been applied to spectroscopic tomography data, and it remains an open question as to whether the accuracy required to derive quantitative images of hemoglobin concentration and oxygen saturation can be maintained in the absorption-coefficient reconstructions at each wavelength.

In this paper we combine the well-known concepts of optical spectroscopy with diffuse optical tomography to investigate the potential of spatially resolving functional hemoglobin parameters on the basis of noninvasively obtained, multisensor, multiwavelength NIR measurements. Experiments were conducted on homogeneous and heterogeneous tissue-simulating phantoms of human blood mixed in a scattering medium that consists of Intralipid and water. Varying the blood volume and the oxygen pressure within these phantoms demonstrates the verification of the capability to quantify both bulk and spatially resolved hemoglobin-concentration and oxygen-saturation levels. Experiments reporting *in vivo* bulk hemoglobin concentration and oxygen saturation are also described. The results suggest that spatially resolved quantitative maps of hemoglobin-related parameters should be possible with NIR diffuse optical tomography in the breast-imaging context. This experience is the first report, to our knowledge, of quantitative NIR tomographic images of the hemoglobin concentration and the oxygen saturation obtained from multispectral experimental data with model-based image-reconstruction methods that preserve the important nonlinearities between the functional property distribution and the measured optical response.

2. Methods and Materials

A. Data-Acquisition System

Our current data-acquisition system (Fig. 1) i: signed for cross-sectional imaging of breast ti It consists of 16 source and 16 detector optical f positioned in a circular array.[21] (An in-depth scription of an earlier version of the instrument can be found in Ref. 21.) The optical fibers w: the array are attached to a radial positioning sy: that allows for variable-diameter fiber moven which provides direct-contact coupling with breast. The position of the circular array can al: varied vertically to allow for selective or mul cross-sectional slices.

A Ti:sapphire laser (Lexel Laser, Model 710) · an argon-ion pump laser (Coherent, Model Innov: is used as a light source for our imaging sys The laser is tunable between 700 and 850 nm by of a single optical setup. The laser beam is an tude modulated with an electro-optic modul (ConOptics, Model 360-80) that is driven by a MHz signal amplified by a 75-W rf amplifier (A: fier Research, Model 75A250). The laser bea: passed through a source optical fiber and dete sequentially through each of the 16 detector op fibers by means of multiplexing the fibers by use linear translation stage (Anorad Corp.). A se: . translation stage is used to multiplex the laser b through each of the 16 source optical fibers, crea a total of 256 measurements. A photomulti tube (Hamamatsu, Model R-928) is used for detec with a housing that contains a heterodyning ci: (ISS, Model K209), that allows for detection of signal amplitude and the phase shift at a lower quency of 1 kHz.

B. Image-Reconstruction Algorithm

The 256 data points acquired for a single wavele: are reconstructed into an image of tissue optical p erties (absorption and reduced scattering coefficie by use of a finite-element-based calculation of diffusion equation.[22] The solution is obta: through a least-squares minimization [minimiz: of χ^2 in Eq. (1), below] of the difference between measured fluence-rate Φ° intensity and phase at: detector i and the calculated fluence-rate Φ^c inter and phase determined from an estimated set of ti: optical properties, summed over the total numbe of observations:

$$\chi^2 = \sum_{i=1}^{M} (\Phi_i^c - \Phi_i^m)(\Phi_i^c - \Phi_i^m)^*,$$

where the asterisk represents conjugation of complex-valued fluence rate. Newton's metho employed to solve the nonlinear minimization p lem iteratively; this problem results from the fi: element solution of the diffusion equation for values of Φ^c. Further details on the reconstruc algorithm can be found elsewhere.[18,19,22]
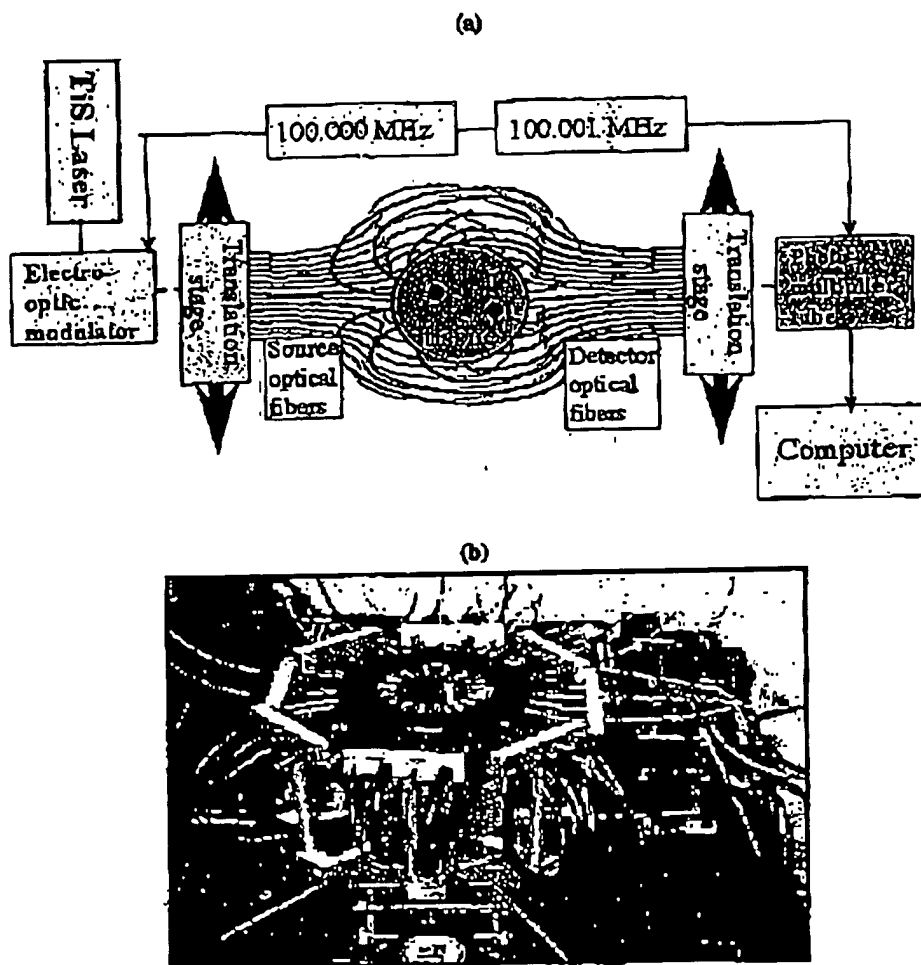
(a)

(b)

Fig. 1. (a) Schematic diagram of the imaging system. TiS, Ti:sapphire. (b) Photograph of the circular array of 16 source optical fi (small, clear, 2-mm plastic fibers) and 16 detector optical fibers (larger, 6-mm, core glass fiber bundles with black exterior). This a allows for a variable radial diameter and vertical translation of the array. A fiberglass sheet with a circular opening is placed over system during patient studies.

C. Tissue Optical Properties

The hemoglobin concentration can be mapped approximately solely on the basis of the absorption coefficient of tissue, as calculated at 800 nm, and an assumed level of water with other absorbers. Hemoglobin oxygen-saturation mapping requires the calculation of the absorption coefficient at a minimum of two wavelengths. Although approximate images can be obtained from two wavelengths, in many of our experiments we chose to reconstruct quantitative images at three wavelengths or more to derive the hemoglobin-concentration and the oxygen-saturation images. This method tends to minimize the effects of noise and can be used to account for absorption that is due to additional chromophores such as water and lipids. Additional wavelengths can be added, if necessary, to account for other absorbers, such as proteins.

We assumed that the calculated absorption coefficient is a combination of absorption arising from water, oxygenated hemoglobin (Hb-O$_2$), deoxygenated

hemoglobin (Hb-R), and lipids. In these expe ments, we neglected the absorption caused by ot tissue chromophores. For theoretical absorption efficients, we used the measured values from Wra al.[23] for Hb-O$_2$ and Hb-R, from Hale and Querry[24] water, and from Quaresima et al.[18] for lipids. plots of the absorption coefficients for water, lipi Hb-O$_2$, and Hb-R taken from the data provided these papers are shown in Fig. 2. For full-ima scans, we used three wavelengths: 750, 800, ε 830 nm. In choosing these wavelengths, we selec 750 nm to emphasize the large difference in abso tion coefficient between Hb-O$_2$ and Hb-R, 800 : because this is the isobestic point for Hb-O$_2$ ε Hb-R, and 830 nm because Hb-O$_2$ is more absorb than Hb-R at this wavelength. The photomultipli tube detector quantum efficiency decreases rapidl; wavelengths longer than 850 nm, making detect at longer wavelengths impossible with the curre setup.
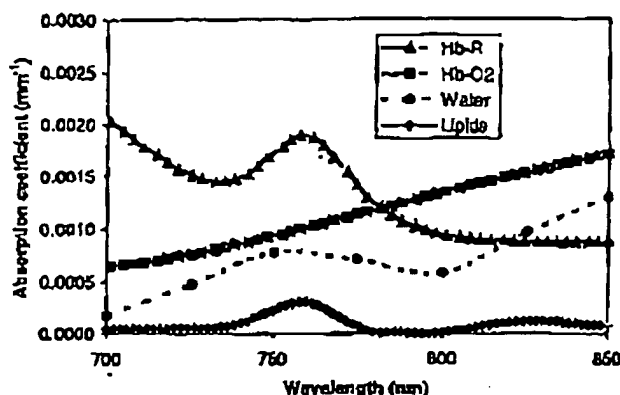
Our imaging method and algorithm also provid

Fig. 2. Plot of the NIR absorption spectra for water, lipids, Hb-O₂, and Hb-R. Values for the absorption coefficient are displayed for anatomically relevant concentrations for breast tissue (31% water, 57% lipid, 10 μM hemoglobin concentration at 60% oxygen saturation).[18,23,24] Relevant values are estimated for Hb-O₂ and Hb-R from data by Tromberg et al.[1] and values for the water and the lipid content are estimates from the data summarized by Woodard and White.[17]

quantitative mapping of the reduced scattering coefficient μ,' of the same region.[19] Measured quantitative values for the reduced scattering coefficient are compared with theoretical values by use of an equation reported by Staveren et al.[25] The scattering-coefficient images generated are not used in the calculations of hemoglobin-concentration or hemoglobin oxygen-saturation level.

D. Imaging Experiments

Our initial experiments were focused on the verification of the capability to quantify correctly the absorption coefficient for oxygenated and deoxygenated blood (more specifically, Hb-O₂ and Hb-R) in a turbid medium. We deoxygenated the phantoms by flushing them with nitrogen gas. Verification of the deoxygenation status was obtained by measurement of the partial pressure of oxygen (pO₂) with a co-oximeter (Chiron Diagnostics, Model Rapidlab 800). This device was also used to confirm the hemoglobin content of our blood samples in terms of the grams per liter of hemoglobin mass in blood volume; this value was used to convert from blood volume to hemoglobin concentration. We found the co-oximetry readings to yield useful measurements of pO₂ as long as the sample pressures were higher than 20 mmHg, below which considerable variance appeared in the pO₂ as a result of transportation of the samples from the phantom to the device. Nitrogen bubbling for 30 min was apparently sufficient to deoxygenate the hemoglobin effectively in the phantoms. Using our standard setup, we imaged homogeneous phantoms of water, Intralipid, and blood with 1 source and 16 detectors. Applying the forward solution of the diffusion equation, we iteratively fitted the computations to the measured data to determine the closest tissue optical properties for a homogeneous medium. The two-dimensional fit was performed on the phase

θ in radians and the log of the intensity A o: measured transmitted light:

$$\chi^2 = \sum_{i=1}^{M-1} ([A_{i+1}{}^o - A_i{}^c] - [A_{i+1}{}^o - A_i{}^o])^2$$
$$+ ([\theta_{i+1}{}^c - \theta_i{}^c] - [\theta_{i+1}{}^o - \theta_i{}^o])^2,$$

where differences (shown in square brackets) used as an approximation of the first derivative: independent of the initial phase angle and so intensity, as described in Eq. (2). The term : minimized on the basis of the comparative chan; the calculated difference in phase θ and the log o: intensity A^c between detectors i and $i + 1$ and difference in the measured values of θ° and A^o for corresponding detectors summed over the comp set of $M - 1$ pairs of detector sites.

Both lipids and water are significant NIR abs ers[18,24] and affect the estimation of hemoglobin centration. In addition, the spectra of l compounds have small absorbance peaks near nm, similar to Hb-R, which can lead to an unde timation of the hemoglobin oxygen saturation. C sequently, for phantom studies the absorbano water was subtracted from the calculated absorpt coefficient spectrum at each wavelength. For in measurements a percentage of the lipid and the ter absorbance spectrum that was based on the erage lipid and water content was subtracted f the absorption-coefficient spectrum prior to perfo ing the least-squares fit to determine the hemogl concentration and the hemoglobin oxygen saturat

A goal of these experiments is to show that po by-point mapping within a tomographic cross sec of either breast tissue or tissuelike phantoms is : sible. To image the hemoglobin concentration : the oxygen saturation in this manner, we applied finite-element method reconstruction algorithm data acquired at multiple wavelengths. For e wavelength the phase and the intensity data are corded at 16 circumferential detector locations each of the 16 source locations. An image of absorption coefficient and the reduced-scattering efficient is formed by use of the reconstruction al rithm. Each different absorption image is t considered as a mapping of the absorption coeffici for that wavelength. A least-squares fit is applied each point in the image; the result is a point-by-pc approximation of the hemoglobin-concentration a the oxygen-saturation levels within breast tissue tissuelike phantoms.

The absorption-coefficient and the redu scattering-coefficient error bars displayed in Fi 3-7 and 9 (below) were determined experimenta by use of the standard deviation of repeated m surements btained at each wavelength and bl concentration. The experimental uncertainties ported in Tables 1-3 for the measurement of t molar absorption coefficient, the Hb-R and t Hb-O₂ concentrations, and the total hemoglok concentration and oxygen saturation were det mined by consideration of the worst-case situati
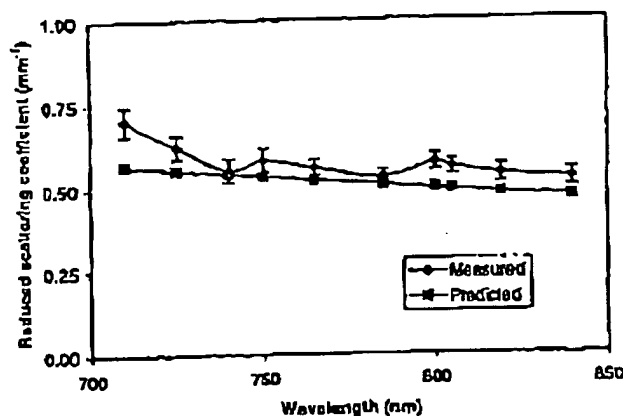
Fig. 9. Comparison of measured values and those predicted by Staveren et al.[25] for the reduced scattering coefficient μ_s' of a phantom containing 0.5% Intralipid in water. Experimental estimates are reached by means of fitting the data from a homogeneous phantom to the finite-element model.

that results from applying the calculated experimental error for the absorption coefficient.

3. Results

A. Reduced Scattering Coefficient

Although the reduced scattering-coefficient images are not used in the estimation of the hemoglobin-concentration or the hemoglobin oxygen-saturation level, the ability to calculate these values quantitatively is an important step in the validation of the imaging algorithm. The quantitative values for the reduced scattering coefficient at several NIR wavelengths for a 0.5% Intralipid solution can be verified by use of an equation reported by Staveren et al.[25] A comparison of the values calculated from the equation of Staveren et al. and the measured data from our system is shown in Fig. 9.

B. Homogeneous Phantom Studies

A preliminary verification of the ability to quantify the Hb-O_2 and the Hb-R content in a tissuelike phantom was accomplished through experimental determination of the molar absorption coefficients of Hb-R and Hb-O_2 at different wavelengths by the imaging of different concentrations of oxygenated and deoxygenated blood in a 0.5% Intralipid and water solution contained in a plastic-beaker phantom. Blood-volume concentrations were converted to hemoglobin concentrations by use of the hemoglobin molecular weight (64,500 g/mole) and the content values obtained from co-oximetry measurements; the hemoglobin content of the blood was found to be roughly 156 g/l of hemoglobin mass in the blood volume. The experimentally determined molar absorption coefficient is the slope of a linear regression that relates the absorption coefficient to the concentration. The results for Hb-R and Hb-O_2 at 750, 800, and 830 nm are shown in Fig. 4, with numerical values tabulated in Table 1. (The R^2 value reported for the linear
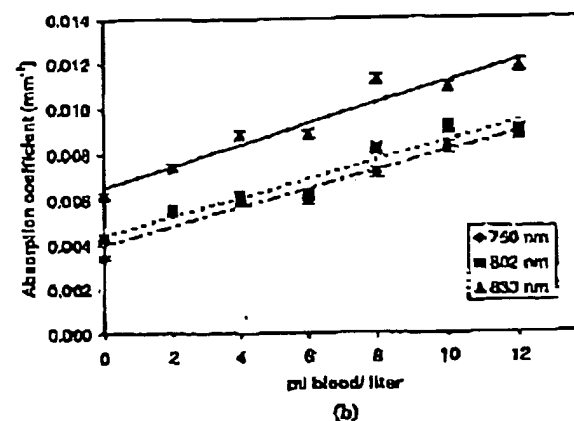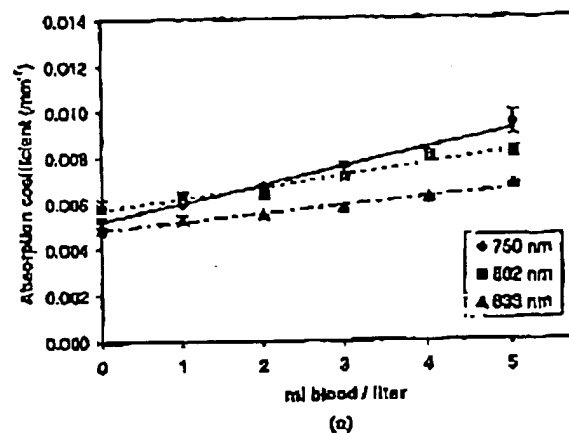

Fig. 4. Plot of the experimentally measured absorption coeffi versus the concentration of blood for three wavelengths: (a) and (b) Hb-O_2. Measurements were recorded from a hon neous scattering medium of 0.5% Intralipid in a 72-mm-diar cylindrical phantom.

regression is the standard correlation coefficie The offset at 0% blood does not match the value: water absorption reported by Hale and Querry.[2]

To investigate further the ability to distingt Hb-O_2 and Hb-R within a turbid medium, we tempted to reproduce the infrared spectra of 1C Hb-O_2 and 10μM Hb-R (hemoglobin concentrat calculated from blood volume) mixed with 0.5% tralipid and water. The NIR absorption-coeffic spectra were again measured by use of data fro source and 16 detectors. The spectra are plotte Fig. 5 and compared with the expected values water plus blood. Again, the curves are relati accurate except for an overall offset.

The offset in the absorption coefficient appear be due to the translucent millimeter-thick pls walls of the beakers used to contain the tissue phantoms. To verify this hypothesis, we meast the spectrum of the water plus 0.5% Intralipid s tion in both a plastic beaker and a thin-walled ball (see Fig. 6). The offset was not apparent in the constructed absorption-coefficient spectrum from thin-walled balloon-phantom data.

Table 1. Comparison of the Experimental Determination of the Molar Absorption Coefficient (Slope of a Linear Regression to the Data) with Values of Wray et al.[20] and Hale and Querry[24]

Substance	Wavelength	Molar Absorption Coefficient		Offset (Value at 0-ml Blood)		R^2 Va
		Wray et al.	Experiment	Hale and Querry	Experiment	
Hb-R	750 nm	0.00076	0.00081 ± 0.00009	0.0026	0.0052 ± 0.0001	0.97
	802 nm	0.00046	0.00050 ± 0.00011	0.0020	0.0057 ± 0.0003	0.92
	833 nm	0.00086	0.00035 ± 0.00005	0.0035	0.0048 ± 0.0001	0.95
Hb-O$_2$	750 nm	0.00031	0.00041 ± 0.00004	0.0025	0.0039 ± 0.0001	0.93
	802 nm	0.00045	0.00042 ± 0.00004	0.0020	0.0044 ± 0.0001	0.94
	833 nm	0.00053	0.00047 ± 0.00004	0.0035	0.0065 ± 0.0001	0.93

Using the assumption that the observed offset is caused by the plastic walls, we applied a correction at each wavelength for a given plastic-beaker phantom. Then, using the spectra for Hb-R, Hb-O$_2$, and water, we performed a least-squares fit on the corrected spectral data to approximate the concentration of each of the three components. For the data presented in Fig. 5 the fitting results after correction are shown in Table 2.
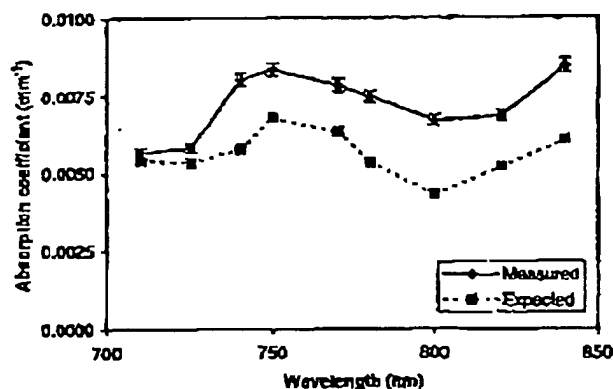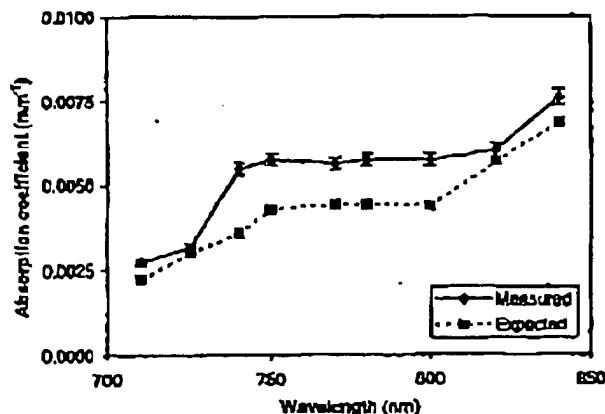
Fig. 5. Comparison of the absorption coefficient calculated from expected values with measured values for blood[20] and water[24]: (a) 10μM deoxygenated hemoglobin in a 0.5% Intralipid and water solution and (b) 10μM oxygenated hemoglobin in a 0.5% Intralipid and water solution.

C. In Vivo Homogeneous Measurements

Similar tests can be performed with in vivo meas ments of breast-tissue NIR spectra. Althc breast tissue is heterogeneous, we can realize proximations to bulk values by assuming hom neous tissue and using the same measure scheme as for the homogeneous phantom stuc An interesting comparison in terms of bulk he globin concentration and oxygen saturation cai obtained by the imaging of the breasts of young older female subjects. By performing similar spectral scans of a 33-year-old woman and a year-old woman, we applied least-squares fits to absorption-coefficient data to approximate the I hemoglobin-concentration and the average he globin oxygen-saturation levels in each case. measured spectra and the corresponding le squares curve fits generated from the calcul concentrations (numerical values are shown in ble 3) and the spectral values of Hb-R, Hb-O$_2$, ter, and lipids are plotted in Fig. 7 for each sub The concentration levels of water and lipid v constrained to the average anatomical values 31% water content and a 57% lipid content breast tissue, as summarized by Woodard White.[17] These values for the average water lipid content are approximate and can vary sig icantly with age and between individuals. To
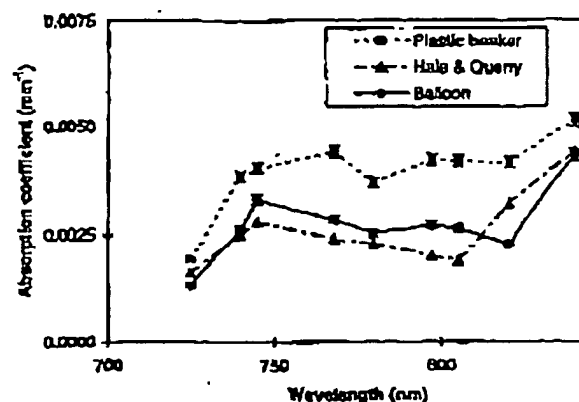

Fig. 6. Comparison of the absorption-coefficient values from and Querry[24] with the absorption coefficient of water meas un a plastic beaker versus a thin-walled balloon. Note that the o is not apparent with the thin-walled balloon.

Table 2. Results of the Least-Squares Fits for Calculating the Hb-O₂ and the Hb-R Contents of a Homogeneous Phantom of Known Composition 10μM Hemoglobin Concentration, 0.5% Intralipid, and Water

	Hb-O₂		Hb-R	
	Calculated	Approximated Real	Calculated	Range of Real
Hb-O₂ concentration (μM)	8.9 ± 1.6	10.0	3.7 ± 1.5	0.0–2.5
Hb-R concentration (μM)	1.7 ± 0.9	0.0	8.9 ± 1.0	7.5–10.0
Total Hb concentration (μM)	10.6 ± 0.9	10.0	12.7 ± 0.8	10.0
Oxygen saturation (%)	84 ± 11	100	29 ± 16	0–25
Preset value of the water content	100%	100%	100%	100%

count for this variation, we included in Table 3 the uncertainty introduced from a possible 50% variation in the average water and lipid concentrations in addition to the experimental uncertainty.

D. Heterogeneous Phantom Studies

To verify the ability to quantify correctly the absorption coefficient of localized blood at three NIR wavelengths, we measured a series of different concentrations of blood objects. A 72-mm phantom (plastic beaker) containing 0.5% Intralipid in water and 0.5% blood was used with a 25-mm object placed just off center. The concentration of blood in the object (a thin-walled clear plastic cylinder) was varied from 0% to 2.0%. The resulting images at 750, 800, and 830 nm are shown in Fig. 8. The absorption-coefficient value from the center region of the object is compared with the expected values calculated from the known hemoglobin (calculated from the blood volume by use of the value of 156 g hemoglobin/l of blood) and water concentrations (based on values from Wray et al.[23] and Hale and Querry[24]). These data are plotted in Fig. 9, and the results of a linear regression on the data are presented in Table 4.

The 25-mm objects used in the heterogeneous phantom studies are thin-walled (200-μm) clear plastic cylinders. The effect of the 200-μm-thick cylinder walls was evaluated through imaging experiments by use of identical contents for the object and the background; these measurements produced no localized evidence of an absorption-coefficient increase. In contrast with the millimeter-thick walls of the exterior beaker, the 200-μm walls of the cylin-

Table 3. Numerical Results of the Least-Squares Fits for Determining the Hemoglobin Concentration and the Homoglobin Oxygen Saturation for Two Subjects[a]

	33-Year-Old Woman	62-Year-Old Woman
Hb-O₂ concentration (μM)	44 ± 4	15 ± 2
Hb-R concentration (μM)	19 ± 3	7 ± 1
Total Hb concentration (μM)	63 ± 2	22 ± 2
Oxygen saturation (%)	70 ± 6	67 ± 7
Preset values of the water content	31%	31%
Preset values of the lipid content	57%	57%

[a]The water and the lipid concentrations were constrained to the approximate values displayed.

der appear to be negligible in comparison with experimental noise.

Absorption-coefficient images at multiple wavelengths can be used to generate an image of the moglobin concentration and the oxygen saturati The merit of this approach was tested with a serie Intralipid phantoms containing objects with vari concentrations of oxygenated and deoxygena blood. Figure 10 shows a sample analysis of a suelike phantom. In this case an 84-mm-diame phantom consisted of a background of a fully oxyg ated 10μM hemoglobin concentration in 0.5%
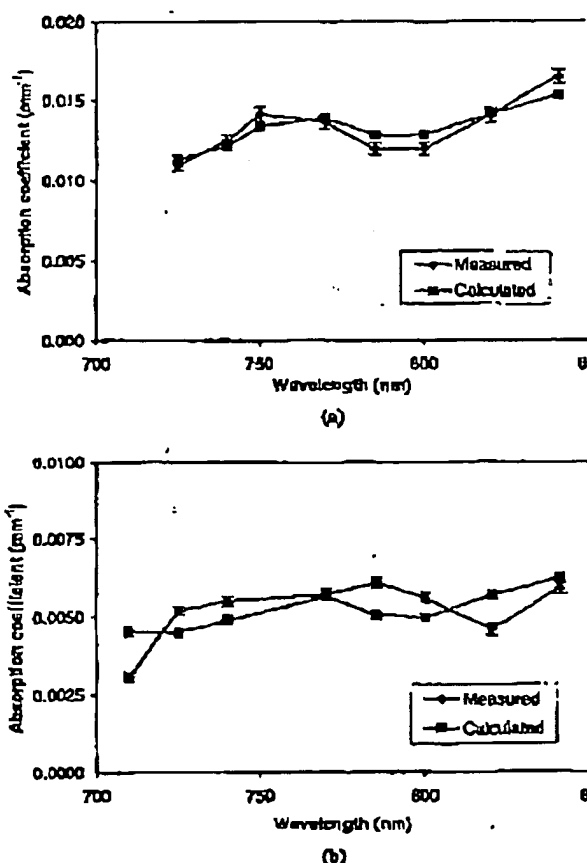

(a)

(b)

Fig. 7. NIR spectra and graphical results of a least-squares fit determine the hemoglobin concentration and the hemoglc oxygen-saturation level for (a) a 33-year-old woman and (b) a year-old woman.
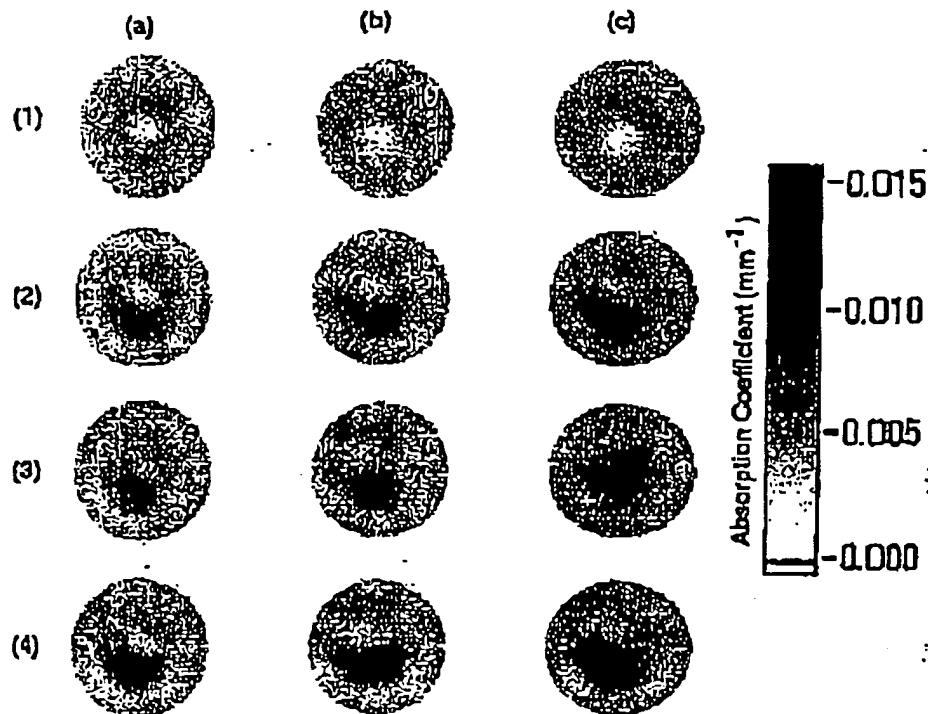
Fig. 8. Collection of absorption-coefficient images for a 25-mm circular object in a 72-mm circular phantom. The background is blood in 0.5% Intralipid and water. The object in the first row has no blood. The object in the second row contains 1% blood, that in third row 1.5% blood, and that in the fourth row 2% blood. Column (a) is measured at 750 nm, column (b) at 800 nm, and column (c) 830 nm.

tralipid and water. The phantom contained two 25-mm circular objects embedded within the background region. The object positioned off center to the right contained the exact same contents as the background, except that the object was bubbled with nitrogen gas to deoxygenate the blood. The second 25-mm object, which contained a fully oxygenated $40\mu M$ hemoglobin concentration in 0.5% Intralipid and water, was positioned left of center. Using a

least-squares fit, one obtains an image of both hemoglobin concentration and the hemoglobin (gen saturation is formed from images at two wr lengths (750 and 802 nm), as illustrated in Fig.

4. Discussion

The molar absorption-coefficient values calcul: from the curves shown in Fig. 4 are similar to results reported by Wray et al.[20] for Hb-R and Hb as shown in Table 1. Similarly, the results for absorption-coefficient spectra for Hb-R and Hb (Fig. 5) are accurate when plotted against establia values; however, an offset appears in both ca Further investigation led to the determination t this offset was due to the presence of the plastic ker used to hold the phantom solutions. Phan(experiments showed that the offset was not evid
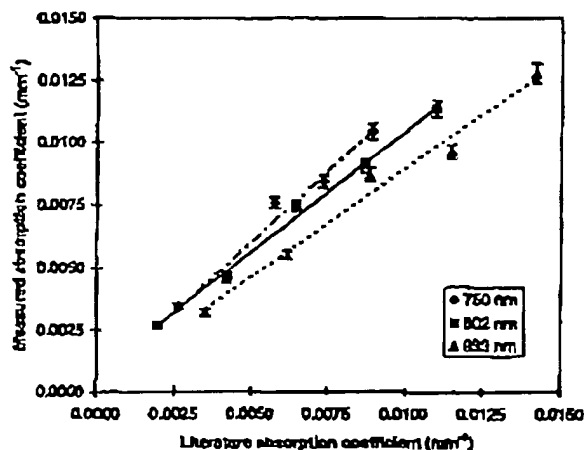
Fig. 9. Comparison of the absorption coefficient taken from the center of the object shown in Fig. 8 with the absorption-coefficient values calculated from the expected values[20,24] for blood and water.

Table 4. Linear-Regression Results from the Data Plotted in Fig.

Result	Wavelength		
	750 nm	802 nm	838 nm
Slope	1.140	0.959	0.870
Offset	0.000	0.001	0.000
R^2 value	0.972	0.994	0.981

[a]A slope of 1 indicates a 1:1 correspondence between absorption-coefficient values from the center of the object in images in Fig. 9 and the absorption-coefficient results calcul: from the expected values for hemoglobin and water.[20,24]
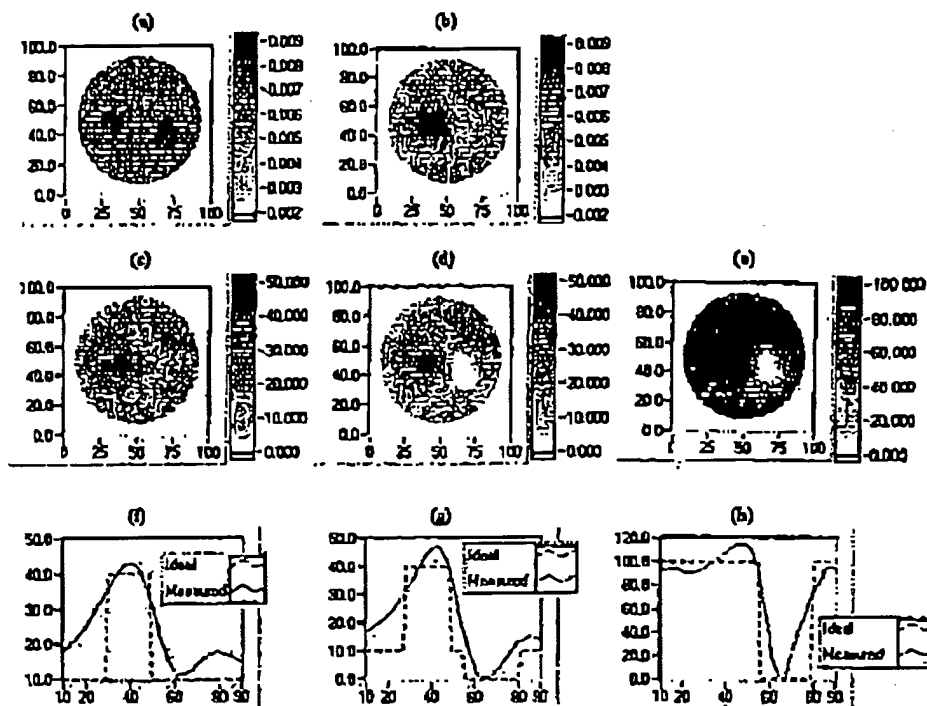
Fig. 10. Absorption-coefficient, hemoglobin-concentration, and hemoglobin oxygen-saturation images of an object with an incre hemoglobin concentration (off center to the left) and an object with deoxygenated blood (off center to the right) in an oxygenated-t background: (a) Absorption coefficient in inverse millimeters at 750 nm, (b) absorption coefficient in inverse millimeters at 802 nm total hemoglobin concentration in micromolar, (d) Hb-O₂ in micromolar, (e) hemoglobin oxygen saturation in percent. The plots one-dimensional transects through (f) the image in (c), (g) the image in (d), (h) the image in (e). Ideal profiles are plotted for compar.

in a thin-walled balloon phantom (Fig. 6). This finding suggests that the offset is due to the effect of the beaker walls and that no such offset should be observed for in vivo measurements. After we account for the offset resulting from the presence of the beaker walls, the results match to within 20% of the known content (the oxygen saturation of the deoxygenated blood was known to be less than 25%) of the tissuelike phantom, as shown in Table 2. Ideally, future calibrations would be performed with thin-walled balloon phantoms; however, in practice, this makes it difficult to include heterogeneities and to bubble solutions with nitrogen gas.

Breast-tissue absorption coefficient has been shown to decrease with age. The results, displayed in Fig. 7, show a dramatic and expected change in the overall breast-tissue absorption coefficient between the younger and the older female volunteers. Similarly, the calculated hemoglobin concentration is significantly higher in the younger woman. This result corresponds well with the known, on-average, decrease in breast-tissue density with age. Quantitative results for the 62-year-old subject are similar to data reported by Tromberg et al. and Fantini et al. The average hemoglobin oxygen-saturation values measured for the two healthy women of 68% and 70% are nearly the same as the results for healthy breast tissue that were measured by Tromberg et al. (66% and 68%).

The images shown in Fig. 8 highlight the abilit recover quantitatively the absorption coefficient objects within a scattering medium at multiple wr lengths. The absorption coefficient at the cente the object when compared with known values (plot in Fig. 9) shows a nearly one-to-one correlation. slope of a linear regression to the data illustrates t errors between 4% and 15% occur for the differ wavelengths examined. The quantitative assi ment of the absorption coefficient at multiple wr lengths should lead to the ability to quantify hemoglobin concentration and the hemoglobin c gen saturation.

For objects with known water content absorption-coefficient images at two waveleng should be sufficient to image the hemoglobin conc tration and the oxygen saturation. The hemoglol concentration and the hemoglobin oxygen-satural images displayed in Fig. 10 correctly recover increased-hemoglobin-concentration object in hemoglobin-concentration image and the deoxyg ated object in the hem globin oxygen-saturation age. The absorption-coefficient images at 750 800 nm are also displayed in Fig. 10; both the creased hemoglobin concentration and the deoxyg ated objects are evident as strong absorbers in 750-nm image, whereas only the increas hemoglobin-concentration object is recovered in 800-nm image. (This result is expected—see

Hb-O$_2$ and the Hb-R spectral signatures in Fig. 2.) These results demonstrate an ability to quantify and to map the hemoglobin concentration and the hemoglobin oxygen saturation accurately, which may provide useful diagnostic information.

The results presented here have relied on the assumption that other absorbers play an insignificant role in the absorption at NIR wavelengths. According to White et al.,[18] breast tissue can be assumed to be approximately 66% adipose tissue and 33% mammary gland for the average healthy adult human female. Using values from Woodard and White[17] demonstrates that the mammary gland has, on average, 51% water, 31% lipids, and 18% protein, whereas adipose tissue has an average composition of 21% water, 71% lipid, and 4% protein (by mass). These values are approximate and vary significantly among individuals; however, on the basis of these data average breast tissue can be approximated roughly as 31% water, 57% lipids, and 8% proteins.[18,17] Hence it appears that it will be necessary for in vivo studies to include calculations of the lipid and the water contents and their contributions to NIR absorption.[18] Further study is required to determine the number of wavelengths necessary to extract accurately the absorption resulting from Hb-R and Hb-O$_2$ from the overall absorption measured as a result of hemoglobin, water, lipids, and other possible absorbers.

In vivo estimates of the hemoglobin concentration and the oxygen saturation are currently being obtained with two to four wavelengths by several research groups that are using NIR optical diffuse data, typically in the form of bulk sample measurements.[1-6] Our research suggests that using Newton's iterative method of reconstruction based on a finite-element implementation of the diffusion-equation approximation allows accurate hemoglobin-concentration and hemoglobin oxygen-saturation images to be obtained with NIR optical diffuse tomography, which can spatially discriminate localized changes in these quantities. It is evident that in vivo mapping of the hemoglobin concentration and the hemoglobin oxygen saturation by use of two wavelengths is quantitatively accurate only if the absorption caused by water and lipids is either insignificant or known and their content is constant throughout the tissue being examined. Heterogeneous mapping of the hemoglobin oxygen saturation by use of three wavelengths is likewise accurate only if the absorption caused by water or lipids is either insignificant or a known constant. Neither of these assumptions appears to be accurate for breast tissue, which obliges the need for multispectral imaging to calculate concentrations of all these relevant chromophores simultaneously. Furthermore, using multiple wavelengths reduces the effects of noise and other errors when deriving these functional parameter maps from absorption-coefficient images, as was recently suggested by McBride et al.[28]

5. Conclusions

This research has confirmed the ability to c quantitative hemoglobin-concentration and oxy saturation images (accurate to 15%) of embedde jects within a highly scattering media in w spatially resolved localized perturbations of t quantities are recovered with model-based in reconstruction methods that preserve the nonli relations between the property map itself and measured multispectral response. In vivo tests demonstrated the potential to determine accur the bulk hemoglobin concentration and hemogl oxygen saturation as well, with single-sou illumination data sets. The effects of other abs ers, such as local variations in water and l content, warrant further investigation. Analys the composition of breast tissue, as taken from published values, has suggested that these other abs ers will be important, which indicates the minimum of four wavelengths will be needed to duce quantitative images of tissue functional par eters in the breast. This conclusion contrasts current practice in which typically data from only wavelengths are pursued.

References

1. B. J. Tromberg, O. Coquez, J. B. Fishkin, T. Pham, J Anderson, J. Butler, M. Cahn, J. D. Gross, V. Venugop and D. Pham, "Non-invasive measurements of breast t optical properties using frequency-domain photon migra Philos. Trans. R. Soc. London 352, 661–668 (1997).

2. J. B. Fishkin, O. Coquoz, E. R. Anderson, M. Brenner, and Tromberg, "Frequency-domain photon migration mea ments of normal and malignant tissue optical propertie human subject," Appl. Opt. 36, 10–20 (1997).

3. S. Fantini, S. A. Walker, M. A. Franceschini, M. Kaschke, Schlag, and R. T. Moesta, "Assessment of the size, posi and optical properties of breast tumors in vivo by nonInv optical methods," Appl. Opt. 37, 1982–1989 (1998).

4. D. T. Delpy and M. Cope, "Quantification in tissue near i red spectroscopy," Philos. Trans. R. Soc. London 352, 649– (1997).

5. B. Chance, Q. Luo, S. Nioka, D. C. Alsop, and J. A. D "Optical investigations of physiology: a study of intrinsic extrinsic biomedical contrast," Philos. Trans. R. Soc. Lo 352, 707–716 (1997).

6. E. L. Hull, M. G. Nichols, and T. H. Foster, "Quantit broadband near-infrared spectroscopy tissue-simulating p toms containing erthrocytes," Phys. Med. Biol. 43, 3381– (1998).

7. A. P. Profio and G. A. Navarro, "Scientific basis of breas mphanography," Med. Phys. 16, 60–65 (1989).

8. B. A. Teicher, "Physiologic mechanisms of therapeutic r tance: blood flow and hypoxia," Hematol. Oncol. Clin. N Am. 9, 475–506 (1995).

9. P. Vaupel, F. Kallinowski, and P. Okunieff, "Blood flow, ox and nutrient supply, and metabolic microenvironment of man tumors: a review," Cancer Res. 49, 6449–6465 (19

10. D. M. Brizel, S. P. Scully, J. M. Harrelson, L. J. Layfield, J. M. Bean, L. R. Prosnitz, and M. W. Dewhirst, "Tumor oxygenation predicts for the likelihood of distant metastases in human soft tissue sarcoma," Cancer Res. 56, 941-943 (1996).

11. P. Okunieff, M. Hoeckel, E. P. Dunphy, K. Schlenger, C. Knoop, and P. Vaupel, "Oxygen tension distributions are sufficient to explain the local response of human breast tumors treated with radiation alone," Int. J. Radiat. Oncol. Biol. Phys. 26, 631-636 (1993).

12. M. Hoeckel, C. Knoop, K. Schlenger, B. Vorndorn, E. Baubmann, M. Mitze, P. G. Knapstein, and P. Vaupel, "Intratumoral pO₂ predicts survival in advanced cancer of the uterine cervix," Radiotharapy Oncol. 26, 45-50 (1993).

13. H. Jiang, K. D. Paulsen, U. L. Osterberg, and M. S. Patterson, "Frequency-domain optical image reconstruction in turbid media: an experimental study of single-target detectability," Appl. Opt. 86, 52-63 (1997).

14. D. A. Boas, M. A. O'Leary, B. Chance, and A. G. Yodh, "Detection and characterization of optical inhomogeneities with diffuse photon density waves: a signal-to-noise analysis," Appl. Opt. 36, 75-92 (1997).

15. J. A. Moon, R. Mahon, M. D. Duncan, and J. Reintjes, "Resolution limits for imaging through turbid media with diffuse light," Opt. Lett. 18, 1591-1593 (1993).

16. D. R. White, H. Q. Woodard, and S. M. Hammond, "Average soft-tissue and bone models for use in radiation dosimetry," Br. J. Radiol. 60, 907-913 (1987).

17. H. Q. Woodard and D. R. White, "The composition of body tissues," Br. J. Radiol. 59, 1209-1219 (1986).

18. V. Quaresima, S. J. Matcher, and M. Ferrari, "Identification and quantification of intrinsic optical contrast for near-infrared mammography," Photochem. Photobiol. 67, 4-14 (1998).

19. H. Jiang, K. D. Paulsen, and U. L. Osterberg, "Frequency-domain near-infrared photo diffusion imaging: initial evaluation in multitarget tissuelike phantoms," Med. Phys. 25, 183-193 (1998).

20. S. R. Arridge and M. Schweiger, "Image reconstruction tical tomography," Philos. Trans. R. Soc. London B 352, 726 (1997).

21. B. W. Pogue, M. Testorf, T. McBride, U. Osterberg, a Paulsen, "Instrumentation and design of a frequ domain diffuse optical tomography imager for breast c detection," Opt. Exp. 1, 391-403 (1997), http://www.osa opticsexpress.

22. H. Jiang, K. D. Paulsen, U. L. Osterborg, B. W. Pogue M. S. Patterson, "Optical image reconstruction frequency-domain data: simulations and experiment Opt. Soc. Am. A 13, 253-266 (1996).

23. S. Wray, M. Cope, D. T. Delpy, J. S. Wyatt, and E. Reynolds, "Characterization of the near infrared absor spectra of cytochrome aa₃ and haemoglobin for the non sive monitoring of cerebral oxygenation," Biochim. Bio Acta, 933, 184-192 (1988).

24. G. M. Hale and M. R. Querry, "Optical constants of wat the 200-nm to 200-μm wavelength region," Appl. Opt. 12, 563 (1973).

25. H. J. van Staveren, C. J. M. Moes, J. van Marle, S. A. P and M. J. C. van Gemert, "Lightscattering in Intralipid-1(the wavelength range of 400-1100 nm," Appl. Opt. 30, 4 4514 (1991).

26. K. Suzuki, Y. Yamashita, K. Ohta, M. Kaneko, M. Yoshida B. Chance, "Quantitative measurement of optical properti normal breast using time-resolved spectroscopy: in viv sults of 30 Japanese women," J. Biomed. Opt. 1, 330. (1996).

27. B. L. Hart, R. T. Steinbock, F. A. Mettler, D. R. Pathak, S. A. Bartlow, "Age and race changes in mammographi renchymal patterns," Cancer 63, 2537-2539 (1989).

28. T. O. McBride, B. W. Pogue, U. L. Osterberg, and K Paulsen, "Image reconstruction of continuously varying ox and simulated breast cancer lesions," in Optical Tomogr and Spectroscopy of Tissue III, B. Chance, R. Alfano, ab Tromberg, eds., Proc. SPIE 3597 (in press).

Spectrophotometric Quantitative Analysis
of the Main Hemoglobin Derivatives

S. A. Adamov, S. A. Aleksandrova, A. N. Denisov,
E. Yu. Mosur, and N. A. Semikolenova*

*Sensor Microelectronics Institute, Siberian Branch of the Russian Academy of Sciences. pr. Mira 55a.
Omsk. 644077 Russia; fax: (3812) 64-8676; E-mail: semikole@univer.omsk.su*

Received October 20, 1997

Abstract—A spectrophotometric multiwavelength method for the simultaneous determination of the main hemoglobin derivatives including oxyhemoglobin, deoxyhemoglobin, carboxyhemoglobin, and methemoglobin has been developed. The choice of analytical wavelengths was made by the methods of information factors and linear programming. The software for the quantitative analysis was developed considering the least square method, linear programming, algebraic background correction, and combined methods including linear programming and algebraic background correction.

Key words: hemoglobin, software, spectrophotometry

Respiration, the source of cellular energy, is oxidation of organic substances by oxygen. Oxygen transport from lungs to tissues and reverse transport of carbon dioxide is performed by hemoglobin, the functional protein of erythrocytes. The function of the main hemoglobin derivatives including oxy- (HbO_2), carboxy- ($Hb(CO)_2$), met- ($metHb$), and reduced hemoglobin (deoxyhemoglobin, Hb) is determined by a ligand bound to the sixth coordination bond of iron atom of the heme moiety (O_2, CO, H_2O). Methemoglobin does not participate in the transport of gases but under certain pathological conditions, it can constitute up to 20% of total hemoglobin. Investigation of the transport functions of erythrocytes requires the simultaneous monitoring of the main hemoglobin derivatives. Ligand binding induces redistribution of electron density of the heme, influences magnetic moment and spin state, and causes optical activity. Electronic conformational interaction generates absorption bands in the visible part of the spectrum from 390 to 650 nm that are characteristic for each derivative. This suggests that spectrophotometry can be used to quantify the main hemoglobin derivatives.

Due to the complex nature of the subject, simple methods of spectrophotometrical analysis lack required precision. According to Kushakovsky [1]. hemoglobin concentrations are assayed by transformation into a system containing lesser number of components using

chemical interconversion. Non-equivalence of the solutions before and after the reaction is a disadvantage of this method. Another solution of the problem is the method of Firordt. Disadvantages of this method include complicated choice of analytic wavelengths due to similarity of absorption spectra of the assayed components, lack of individual absorption regions, and increasing error in case of systems containing more than four components. The problem can be solved by redetermined systems of linear algebraic equations (SLAE).

The goal of the present work was to develop a spectrophotometric method of simultaneous assay of the main hemoglobin derivatives including oxy-, deoxy-, carboxy-, and methemoglobin.

MATERIALS AND METHODS

Samples of heparin-treated blood were withdrawn from the elbow vein of donors. Blood solution (1%) was prepared by mixing 20 ml of distilled water, 0.06 ml of 0.04% ammonium solution (to clear the solution), and 0.5 ml of the blood; 1-2 min later (after the hemolysis), 25 ml of 0.0667 M potassium-sodium phosphate buffer (pH 7.2) were added. Total volume was adjusted to 50 ml with distilled water. Spectra were recorded at 450-650 nm in a quartz cell (1 cm thick) using a SF-20M double-beam spectrophotometer with automatic aperture regulation. Assays were performed within 1 h after blood withdrawal.

* To whom correspondence should be addressed.

SPECTROPHOTOMETRIC ANALYSIS OF HEMOGLOBIN DERIVATIVES   1161

RESULTS AND DISCUSSION

Quantitative spectrophotometric analysis is reduced d wn to solution of the system of Firordt equations:

$$\sum_{j=1}^{n} \varepsilon_j^{\lambda_i} c_j = A^{\lambda_i}. \tag{1}$$

where $i = 1, 2, ..., m$; m is the number of analytical wavelengths; n corresponds to the number of quantified components; $\varepsilon_j^{\lambda_i}$ are the molar extinction coefficients of component j at wavelength λ_i; c_j is the quantified concentration of component j; A^{λ_i} corresponds to absorption at wavelength λ_i.

The methods of solution of redetermined SLAE used in the present work are considered below.

The least square method (LSM). This method is the classical solution of redetermined SLAE. The criterion of the solution is the minimum of the sum of squares of deviations of the experimental spectrum from the expected one:

$$U = \left[\sum_{i=1}^{m} \left(A^{\lambda_i} - \sum_{j=1}^{n} \varepsilon_j^{\lambda_i} c_j \right)^2 \right] = \min. \tag{2}$$

Solution of system (1) by the least square method can include negative concentrations of certain components that lack physical sense. Negative concentrations are usually associated with similarity of absorption spectra of certain components. Moreover, negative concentrations appear when the matrix contains many components some of which are present at low concentrations or are absent. Negative values in solution of the system (1) can be excluded in two ways.

1. The following sum is used as the criterion of optimal solution:

$$U_a = U + \sum_{i=1}^{m} \sum_{j=1}^{n} (\varepsilon_j^{\lambda_i} c_j')^2, \tag{3}$$

where c_j' are the negative elements of the concentration column vector.

2. The values can be obtained by iteration so that the negative concentrations obtained during the first iteration are assumed to be zero and the column corresponding to these components are excluded from the matrix.

Algebraic background correction method (ABC). In systems with unknown qualitative composition, absorption is expressed as follows:

$$A^{\lambda_i} = \sum_{j=1}^{n} \varepsilon_j^{\lambda_i} c_j + \sum_{k=0}^{l} a_k \lambda_i^k. \tag{4}$$

This redetermined SLAE is solved by the least square method so that the first n columns of the matrix of the system coefficients c ntain the $\varepsilon_j^{\lambda_i}$ values and the subsequent $l + 1$ columns contain the λ_i^k values. To lower the calculation error due to rounding, the λ values in Eq. (4) are replaced with the $\lambda - \bar{\lambda}$ values (where $\bar{\lambda}$ is the mean wavelength of the interval) and for equidistant wavelengths, with their consecutive numbers. The most important factor determining the validity of this method is the difference between the absorption spectra of contaminating and main compounds. Efficiency of the ABC method increases when the impact of the main compound increases (polynomial order $k > l + 1$.

Linear programming method (LPM). The LPM is used to exclude the effect of background absorption during quantitative analysis of a multicomponent mixture. In this case, absorption equals:

$$A^{\lambda_i} + A^{\lambda_i}_{pdco} = \sum_{j=1}^{n} \varepsilon_j^{\lambda_i} c_j. \tag{5}$$

The system requires the minimal differential spectrum

$$\min \left[\sum_{i=1}^{m} \left(A^{\lambda_i} - \sum_{j=1}^{n} \varepsilon_j^{\lambda_i} c_j \right) \right],$$

under constant $\sum_{i=1}^{m} A^{\lambda_i}$ this is equivalent to the condition $\max \sum_{i=1}^{m} \sum_{j=1}^{n} \varepsilon_j^{\lambda_i} c_j$. This means that the maximum of the function

$$Z = \sum_{i=1}^{m} \sum_{j=1}^{n} \varepsilon_j^{\lambda_i} c_j$$

should be found constraining $A^{\lambda_i} - \sum_{j=1}^{n} \varepsilon_j^{\lambda_i} c_j > 0$.

According to the LPM, the solution of the quantitative analysis problem corresponds to that of the method of analytical bands selected in the most clear region of the spectrum of contaminations but in the case of LPM, the spectrum of the contaminations d es not have to be known [2]. Differential spectrum corresponds to the spectra of non-identified components. The simplex optimization method is used to solve system (1) that includes limitation of negative concentrations.

Combined methods including LPM and ABC. If the spectrum of the mixture lacks individual absorption regions of the main compounds this can be used to analyze wavelengths corresponding to minimal absorption of contamination. Such wavelengths can be selected by the LPM. In another words, the LPM selects analytical wavelengths with minimal or zero absorp-

1162   ADAMOV et al.

tion of contamination. The LPM solution is correct
only if the studied spectral region includes wavelengths
with zero background absorption. Otherwise, the
method does not eliminate the influence of contami-
nation on the results but only minimizes such influ-
ence.

Thus, it is of interest to combine the LPM and
ABC algorithms in a single method. The first combi-
nation is the selection of analytical wavelengths with
minimal absorption of contamination by the LPM and
subsequent polynomial approximation of the back-
ground spectrum at these wavelengths by ABC.

The second possibility is to set up a problem of
linear programming possessing ABC properties. The
criterion of the solution of this problem is:

$$U = \sum_{i=1}^{m}\left(A^{\lambda_i} - \sum_{j=1}^{n} \varepsilon_j^{\lambda_i} c_j - \sum_{k=0}^{l} a_k\lambda_i^k\right) = \min, \qquad (6)$$

and constraints include the following expressions:

$$\sum_{k=0}^{l} a_k\lambda_i^k > 0; \ c_j > 0; \ A^{\lambda_i} - \sum_{j=1}^{n} \varepsilon_j^{\lambda_i} c_j - \sum_{k=0}^{l} a_k\lambda_i^k > 0.$$

LPM + ABC combination enables analysis of a
mixture by approximating the background absorption
with polynomials of higher exponent versus the spec-
trum of the main compound.

The developed programs were tested for mixtures
with known concentrations of the components. Solu-
tions of methyl orange (existing in two forms: acidic
and alkaline) were used as the reference. The data
obtained by various methods are compared in the table.
The results are in good agreement with the reference
values, thus suggesting efficiency of the programs and
their possible application in a more complicated sys-
tem, i.e., hemoglobin derivatives.

Gas composition of the whole blood solution was
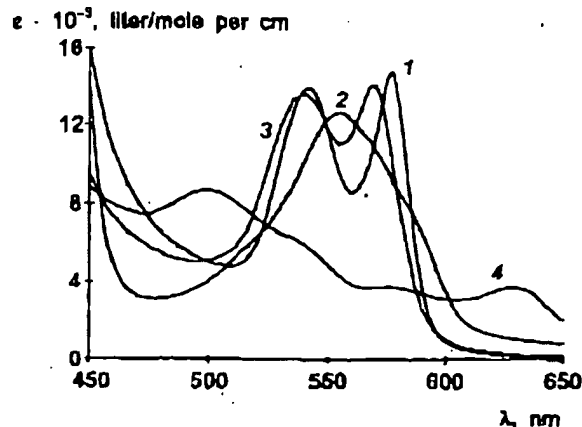studied by computer programs used for analysis of

$\varepsilon \cdot 10^{-3}$, liter/mole per cm

Fig. 1. Absorption spectra: 1) oxyhemoglobin; 2) deoxy-
hemoglobin; 3) carboxyhemoglobin; 4) methemoglobin [3].

absorption spectra of the multicomponent systems of
hemoglobin derivatives containing HbO_2, Hb, $Hb(CO)_4$,
metHb. Molar extinction coefficients used for analysis
were taken from [3] (Fig. 1). Analytical wavelengths
were selected by the information coefficient method [4].
To evaluate the optimal selection of wavelengths and
error of analysis, the information coefficient matrix is
constructed from the following elements:

$$R_{ij} = \frac{\varepsilon_j^{\lambda_i}}{\sum_{k=1}^{n} \varepsilon_k^{\lambda_i}} \qquad (7)$$

The R_{ij} element indicates the fraction of informa-
tion of the i band on the determination of the j com-
ponent of the mixture. The higher are the information
coefficients, the lower are the errors of the solution.
Also, to determined analytical wavelengths the differ-
ences $\varepsilon_i^{\lambda} - \varepsilon_j^{\lambda}$ and ratios $\varepsilon_i^{\lambda}/\varepsilon_j^{\lambda}$ were used to select
the points of maximal differences in oxyhemoglobin

Comparison of alkaline and acidic fractions (%) in methyl orange mixtures by LSM, ABC, LPM, and LPM +
ABC

Mixture number	Reference		LSM		ABC		LPM		LPM + ABC	
	alkaline	acidic	alkaline	acidic	alkaline	acidic	alkaline	acidic	alkaline	acidic
1	6	94	5.9	94.1	5.8	94.2	5.8	94.2	6.1	93.9
2	9.7	90.3	9.2	90.8	8.9	91.1	9.3	90.7	9.5	90.5
3	88.6	11.4	88.5	11.5	88.8	11.2	88.5	11.5	88.6	11.4
4	94.1	5.9	94	6	94.6	5.4	93.8	6.2	94.3	5.7
5	96.6	3.4	96.4	3.6	96.6	3.4	96.5	3.5	96.6	3.4

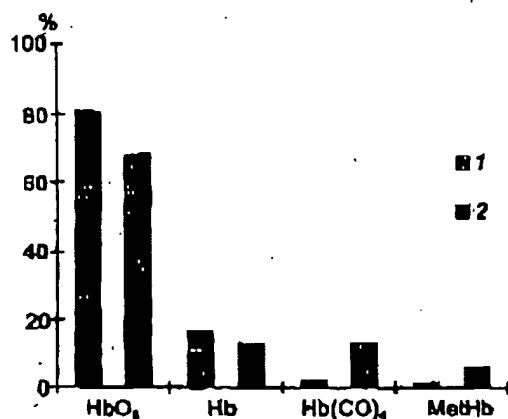## SPECTROPHOTOMETRIC ANALYSIS OF HEMOGLOBIN DERIVATIVES   1163

Fig. 2. Percentage contents of the main hemoglobin derivatives determined using the developed programs for smoking (2) and non-smoking (1) patient.
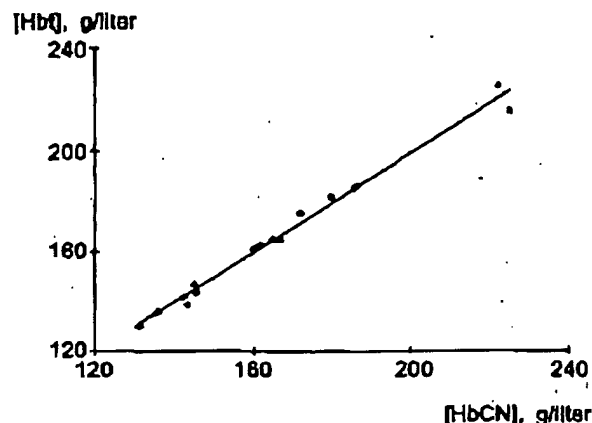

Fig. 3. Effect of total hemoglobin concentration determined by the standard cyanmethemoglobin method on the sum of concentrations of hemoglobin derivatives calculated by the developed method.

and carboxyhemoglobin spectra (their spectra are quite similar thus contributing significant error in determination of carboxyhemoglobin concentration). Then, these wavelengths were studied by LPM. Their composition varied during analysis. Those wavelengths that had no effect on the result were excluded from the experiment. Minimal difference between experimental and reduced spectra at a certain wavelength was another criterion of selection.

To illustrate the developed method, the effect of nicotine intoxication in men on concentrations of hemoglobin derivatives was studied. The data of Fig. 2 indicate that the body undergoes negative changes including lowering of oxyhemoglobin content due to increase in carboxyhemoglobin concentration and hence lowering of hemoglobin oxygenation.

The precision of the method of quantitative analysis of mixtures of hemoglobin derivatives was evaluated. The sum of concentrations of hemoglobin derivatives calculated using the method would be equal to total hemoglobin concentration in the same blood sample determined by the standard cyanmethemoglobin method; this was the criterion of correctness of calculations of concentrations of hemoglobin derivatives. Effect of total hemoglobin concentration on the calculated sum of concentrations of hemoglobin derivatives

is shown in Fig. 3. Slope of the approximating line is 0.997 and significance of approximation is 0.987, thus confirming the identity of the results.

Thus, the multiwavelength method of determination of the main hemoglobin derivatives is developed and the software is created. The method can be used in quantitative spectrophotometric analysis of any chemical systems with overlapping absorption spectra of the components. A special multiwavelength module with fixed selection of analytical wavelengths can be constructed on the basis of the method and used in clinical practice.

The work was supported by research programs "Universities of Russia" and "Siberia".

REFERENCES

1. Kushakovsky, M. S. (1968) Clinical Forms of Hemoglobin Alterations [in Russian], Meditsina, Leningrad.
2. Vasil'ev, A. F. (1976) Use of Computers in Chemical and Biological Studies [in Russian], Khimiya, Moscow.
3. Sigaard-Andersen, J., Norgaard-Pedersen, O. B., and Rem, I. (1972) Clin. Chim. Acta, 42, 101-108.
4. Bershtein, I. Ya., and Kaminsky, Yu. L. (1986) Spectrophotometrical Analysis in Organic Chemistry [in Russian], Khimiya, Leningrad.